EPFL - MSc in Computational Science and Engineering

Master Thesis

Isogeometric discretization of the Stokes problem on trimmed domains

Supervisors:
Prof. Annalisa Buffa
Dr. Pablo Antolín
Dr. Rafael Vázquez Hernández

Student:
Andrea Scaglioni
andrea.scaglioni@epfl.ch
Student n°: 272851

ÉCOLE POLYTECHNIQUE
FÉDÉRALE DE LAUSANNE

Academic year 2018-2019
Submitted on January 18th, 2019

Abstract

The main problems arising from the isogeometric discretization of the Stokes problem on trimmed domains are discussed. Taylor-Hood and Raviart-Thomas isogeometric elements are tested on several trimmed geometries and their convergence and stability properties analyzed. Dirichlet boundary conditions are imposed weakly through Nitsche's method, which makes the problem unstable for certain configurations of trimming curve and computational mesh. An existing stabilization is applied following the know-how on elliptic problems. Our numerical experiments suggest that for some trimmed domains neither Taylor-Hood not Raviart-Thomas elements are always inf-sup stable and the question of how to restore stability remains unanswered.

Contents

Chapter 1

Introduction

Isogeometric analysis (IGA) [15] is a relatively recent collection of numerical methods for the approximation of boundary value problems. IGA is characterized by the use of spline or NURBS (Non-uniform rational B-splines) functions in the description of both the computational domain and the numerical solution. This description of the computational domain is particularly interesting as it allows to avoid meshing procedures that often introduce geometric approximations or can be even difficult to terminate successfully in the case of complex geometries. The use of B-splines as shape functions allows to obtain numerical solutions with higher continuity compared to standard finite elements, a feature that can be exploited to obtain more accurate solutions at the same computational cost.

The long-term aim of isogeometric analysis is to bridge the gap between Computer-Aided Design (CAD) and numerical simulation. This is a challenging target to achieve mainly because current CAD software do not provide a description of the geometry that can be directly used in numerical simulation. Still, isogeometric methods attract an increasing number of members of the scientific community.

In CAD, trimming is both a fundamental tool for the description of complex geometries and a major obstacle to the integration with numerical simulation. By trimming, we refer to the application of boolean operations (intersection, union, set difference) on geometric object (in this context often called *primitives*). The fact that trimming operations cannot be performed exactly lead to a number of issues, not only within the CAD framework but also in numerical simulation. As a consequence, the development of numerical schemes aimed at solving boundary value problem on domain whose description is available as a trimmed geometry is desired.

In the present work we focus on the (incompressible) Stokes problem in fluid mechanics on two-dimensional trimmed domains. The first goal of the present work is to present a formulation of the discrete problem that allows the imposition of natural or essential boundary conditions on the trimmed region of the boundary. As for essential boundary conditions, they are enforced weakly through Nitsche's method. The isogeometric spaces we use to discretize velocity and pressure are based on Taylor-Hood and Raviart-Thomas isogeometric elements, which proved to have good stability and convergence properties in the untrimmed case [5]. Secondly, another goal is to carry out and analyse numerical experiments on several trimmed geometries. These numerical experiments are aimed at clarifying the properties of the numerical schemes at hand, in particular convergence and stability. Convergence of approximation errors of velocity and pressure fields are studied with respect to several norms. Stability is assessed through the approximation of continuity, coercivity and inf-sup constants of appropriate differential operators. Three different trimmed geometries are employed with the aim of highlighting how the position of the trimming curve can influence the convergence and stability properties of the schemes. Finally, having acknowledged the existence of configurations of trimming curves and com-

putational meshes that impair the stability of the schemes, a stabilization first developed for elliptic problems [6] is applied to the problem at hand.

The outline of the present work is as follows. In Chapter 2, the basic notation used throughout the work is defined. In Chapter 3, several basic notion about the Stokes problem and its isogeometric discretization are reported. In Chapter 4, the Poisson problem is considered to show how a regular isogeometric scheme can be modified to cope with trimmed geometries. In addition, some stability issues are highlighted and a stabilization aimed at curing them is introduced. In Chapter 5 and 6, numerical schemes based on Taylor-Hood and Raviart-Thomas isogeometric elements respectively are introduced. Additionally, the stabilization presented in Chapter 4 is applied to these schemes and numerical experiments are carried out. In Chapter 7, additional numerical experiments are carried out on different geometries. In Chapter 8, a simple preconditioner is presented. Finally, in Chapter 9 we summarize the results of numerical experiments, the achievements of the present work and some possible future developments.

Chapter 2

Notation

If d is a positive integer, $\boldsymbol{m}, \boldsymbol{n} \in \mathbb{N}^d$, we denote $\boldsymbol{m}..\boldsymbol{n} = (m_1..n_1) \times ... \times (m_d..n_d)$.
Given Ω, an open, connected subset of $\mathbb{R}^d$ (with d a positive integer) with Lipschitz boundary, denote for all $p \geq 1$

$$L^p(\Omega) := \left\{ u : \Omega \to \mathbb{R} : \int_\Omega |u|^p \mathrm{d}x < \infty \right\} \qquad 1 \leq p < \infty,$$
$$L^\infty(\Omega) := \{ u : \Omega \to \mathbb{R} : \mathrm{esssup}_\Omega |u| < \infty \} \qquad p = \infty.$$

$L^p(\Omega)$ is a Banach space with the standard norm:

$$\|u\|_{L^p(\Omega)} := \sqrt[p]{\int_\Omega |u|^p \mathrm{d}x} \qquad 1 \leq p < \infty,$$
$$\|u\|_{L^\infty(\Omega)} := \mathrm{esssup}_\Omega |u| \qquad p = \infty.$$

$L^2(\Omega)$ is also a Hilbert space if equipped with the scalar product $(u, v) = \int_\Omega uv \mathrm{d}x$. This scalar product induces the norm defined above for $L^2(\Omega)$ as $\|u\|_{L^2(\Omega)} = \sqrt{(u, u)}$. The subset of zero-average functions in $L^2(\Omega)$ will be denoted:

$$L^2_0(\Omega) := \left\{ v \in L^2(\Omega) : \int_\Omega v \mathrm{d}x = 0 \right\}.$$

The $L^2(\partial\Omega)$ scalar product is denoted $(u, v)_{\partial\Omega} := \int_{\partial\Omega} uv \mathrm{d}\Sigma$ and analogously $(\cdot, \cdot)_\Gamma$ the $L^2(\Gamma)$ scalar product if $\Gamma \subset \partial\Omega$ is regular enough.
Define the Sobolev space

$$W^{k,p}(\Omega) := \left\{ v \in L^p(\Omega) : D^{\boldsymbol{\alpha}} v \in L^p(\Omega) \ \forall \boldsymbol{\alpha} \in \mathbb{N}^d : |\boldsymbol{\alpha}| \leq k \right\} \ \forall k, p \geq 1,$$

where $\boldsymbol{\alpha} = (\alpha_1, ..., \alpha_d) \in \mathbb{N}^d$ is a *multi-index*, $|\boldsymbol{\alpha}| := \sum_{i=1}^d |\alpha_i|$ and $D^{\boldsymbol{\alpha}}$ represents the differential operator $\frac{\partial^{|\boldsymbol{\alpha}|}}{\partial x_1^{\alpha_1} ... \partial x_d^{\alpha_d}}$. The Sobolev space $W^{k,p}(\Omega)$ is a Banach space if equipped with the norm:

$$\|u\|_{W^{k,p}(\Omega)} := \left(\sum_{|\boldsymbol{\alpha}| \leq k} \|D^{\boldsymbol{\alpha}} u\|^p_{L^p(\Omega)} \right)^{\frac{1}{p}}.$$

For $k = 0$ we observe that $W^{k,p}(\Omega) = L^p(\Omega)$ and for $p = 2$ we will denote $H^k(\Omega) := W^{k,2}(\Omega)$.
The Sobolev space $H^k(\Omega)$ is a Hilbert space with respect to the scalar product:

$$(u, v)_{H^k(\Omega)} := \sum_{|\boldsymbol{\alpha}| \leq k} \int_\Omega D^{\boldsymbol{\alpha}} u D^{\boldsymbol{\alpha}} v \mathrm{d}x$$

for any $k > 0$. This scalar product induces the norm $\|u\|_{H^k(\Omega)} := \sqrt{(u,v)_{H^k(\Omega)}} = \|u\|_{W^{k,2}(\Omega)}$ and the semi-norm

$$|u|_{W^{k,p}(\Omega)} := \left(\sum_{|\boldsymbol{\alpha}|=k} \|D^{\boldsymbol{\alpha}} u\|^p_{L^p(\Omega)} \right)^{\frac{1}{p}}.$$

Let moreover $H^{-k}(\Omega)$ be the dual space of $H^k(\Omega)$ and $H^{k-\frac{1}{2}}(\partial\Omega)$ the trace space on $\partial\Omega$. Analogous linear spaces can be defined for vector valued functions $\boldsymbol{u} = (u_1, ..., u_q) : \Omega \to \mathbb{R}^q$ where q is a positive integer. Letting V be any of the linear spaces defined above, we define the vector-valued counterpart $\boldsymbol{V} = (V)^d := \bigotimes_{i=1}^d V$ and equip it with the Euclidean norm of the norms of the components:

$$\|\boldsymbol{u}\|_{\boldsymbol{V}} := \sqrt{\sum_{i=1}^d \|u_i\|^2_V} \qquad \forall \boldsymbol{u} \in \boldsymbol{V}.$$

Any other l^p norm could be employed and would lead to an equivalent norm.
For the Sobolev spaces $\boldsymbol{H}^k(\Omega)$ (in particular for $\boldsymbol{L}^2(\Omega)$) a scalar product can be defined analogously:

$$(\boldsymbol{u}, \boldsymbol{v})_{\boldsymbol{H}^k(\Omega)} := \sqrt{\sum_{i=1}^d (u_i, v_i)^2_{H^k(\Omega)}}.$$

Chapter 3

Isogeometric discretization of the Stokes problem

In the present chapter several preliminary concepts are recalled in order to fix the notation, present the problem of interest and recall basic concept about Isogeometric methods. In the first three sections we mainly follow [8] and [13] to present B-splines in one and several spacial dimensions as well as the geometric description of the domain. Despite the fact that we do not consider them here, Non Uniform Rational B-Splines (NURBS) are also a fundamental tool for the geometrical description of the domain. An extensive treatise on B-splines and NURBS can be found in [17].
In the fourth section the (continuous) Stokes problem is presented and its well-posedness discussed. Finally, in the fifth section the isogeometric discretization of the Stokes problem is discussed and Taylor-Hood and Raviart-Thomas elements are presented as examples of stable isogeometric spaces for the problem at hand. For the formulation and well posedness of both continuous and discrete Stokes problems we mainly follow [3] for the formulation *à la Brezzi* and [20] for the formulation *à la Babuska*.

3.1 Univariate B-splines

Given two positive integers n, p we considered the *knot vector*

$$\Xi := \{\xi_1 \leq \xi_2 \leq ... \leq \xi_{n+p} \leq \xi_{n+p+1}\}$$

where the ξ_i are real numbers. Up to an affine transformation we can assume $\xi_1 = 0$ and $\xi_{n+p+1} = 1$. Observe that elements in Ξ may not be unique. Given a knot vector Ξ, we introduce the set of *breakpoints* formed by the elements of Ξ taken without repetition,

$$Z := \{\zeta_1 < \zeta_2 < ... < \zeta_{N-1} < \zeta_N\}.$$

The set of *knot spans* $\{I_i\}_{i=1}^{N-1}$ where $I_i := (\zeta_i, \zeta_{i+1})$ forms a partition of $(0, 1)$. We can define the *measure of* I_i as $h_i := \zeta_{i+1} - \zeta_i$ for $i \in 1..N-1$.
The set formed by the number of times each knot is repeated, the *vector of knots multiplicities*, is denote $\boldsymbol{r} := \{r_i\}_{i=1}^{N} \subset \mathbb{N}^N$. As a result, $n + p + 1 = \sum_{i=1}^{N} r_i$. Moreover, we assume $r_i < p + 1$ for all $i \in 1..N$.
The knot vector Ξ is said to be *open* if $\xi_1 = \xi_2 = ... = \xi_{p+1}$ and $\xi_n = \xi_{n+1} = ... = \xi_{n+p+1}$, or equivalently if $r_1 = r_N = p+1$. Knot vectors will be assumed open throughout the rest of this report.
Given a knot vector Ξ, the *B-spline basis related to* Ξ, $\left\{\hat{B}_{i,p}\right\}_{i=1}^{n}$ is defined as follows

(*Cox-DeBoor formula*):

$$\hat{B}_{i,0}(\zeta) := \begin{cases} 1 & \text{if } \xi_i \leq \zeta < \xi_{i+1} \\ 0 & \text{otherwise} \end{cases};$$

$$\hat{B}_{i,p}(\zeta) := \frac{\zeta - \xi_i}{\xi_{i+p} - \xi_i}\hat{B}_{i,p-1}(\zeta) + \frac{\xi_{i+p+1} - \zeta}{\xi_{i+p+1} - \xi_{i+1}}\hat{B}_{i+1,p-1}(\zeta) \qquad \forall p > 0;$$

where we assume $0/0 = 0$.
The set $\left\{\hat{B}_{i,p}\right\}_{i=1}^{n}$ has the following properties:

- Non-negativity: $\hat{B}_{i,p}(\zeta) > 0 \ \forall i \in 1..n$;
- Partition of unity: $\sum_{i=1}^{n} \hat{B}_{i,p}(\zeta) \equiv 1$;
- Local support: $\hat{B}_{i,p}(\zeta) = 0$ if $\zeta \notin [\xi_i, \xi_{i+p+1}]$. Therefore, each B-spline depends only on $p+2$ knots that are collected in the *local support* $\Xi_{i,p} := \{\xi_j\}_{j=i}^{i+p+1}$;
- Piecewise polynomial: $\hat{B}_{i,p}|_{[\zeta_j,\zeta_{j+1}]} \in \mathbb{P}_p([\zeta_j, \zeta_{j+1}])$ for each $j \in 1..N-1$.

The linear space defined by a B-spline basis is called *univariate spline space* :

$$S^p_{\boldsymbol{\alpha}} = S^p_{\boldsymbol{\alpha}}(\Xi) := \text{span}\left\{\hat{B}_{i,p} : i \in 1..n\right\},$$

which can also be characterized as the space of piecewise polynomials of degree p with $\alpha_j := p - r_j$ continuous derivatives at the breakpoint ζ_j for all $j \in 1..N$. The number of continuous derivatives at the breakpoints are collected in the *regularity vector* $\boldsymbol{\alpha} := \{\alpha_i\}_{i=1}^{N}$. A knot multiplicity $r_j = p+1$ corresponds to a regularity $\alpha_j = -1$, i.e. the fact that a discontinuity is allowed at ζ_j.
The derivatives of splines are splines as well. It can actually be proved that the derivation operator is bijective between two spline spaces:

$$\left\{\frac{\mathrm{d}v}{\mathrm{d}x} : v \in S^p_{\boldsymbol{\alpha}}\right\} = S^{p-1}_{\boldsymbol{\alpha}-1}.$$

3.2 Multivariate B-splines

Let d be the space dimension. Assume $n_l \in \mathbb{N}$, $p_l \in \mathbb{N}$, and related knot vector $\Xi_l := \{\xi_{l,i}\}_{i=1}^{n_l+p_l+1}$ and breakpoints $Z_l := \{\zeta_{l,i}\}_{i=1}^{N_l}$ are given for all l in $1..d$. Define $\boldsymbol{p} := (p_1, ..., p_d)$, $\boldsymbol{n} := (n_1, ..., n_d)$, $\boldsymbol{N} = (N_1, ..., N_d)$ and $\boldsymbol{\Xi} := \Xi_1 \times ... \times \Xi_d$. The *parametric Bézier mesh* is defined as

$$\hat{\mathcal{M}} := \{Q_{\boldsymbol{j}} := I_{1,j_1} \times ... \times I_{d,j_d} : I_{l,j_l} := (\zeta_{l,j_l}, \zeta_{l,j_l+1}) \ \forall \boldsymbol{j} = (j_1, ..., j_d) \in \mathbf{1}..(\boldsymbol{N} - \mathbf{1})\}$$

and the $Q_{\boldsymbol{j}}$ are called *Bézier elements*. The Bézier mesh defines a cartesian grid on the *parametric domain* $\hat{\Omega} := (0,1)^d$. An *element size* is associated to any $Q \in \hat{\mathcal{M}}$ as $h_Q := \text{diam}(Q)$ and a *global mesh size* as $\hat{h} := \max\left\{h_Q : Q \in \hat{\mathcal{M}}\right\}$. We may explicitly specify the mesh-size by making it appear in the symbol, e.g. $\hat{\mathcal{M}}_h$.
The set of *multivariate B-splines related to* $\boldsymbol{\Xi}$ is defined as:

$$\left\{\hat{B}_{\boldsymbol{i},\boldsymbol{p}} = \hat{B}_{i_1,p_1}...\hat{B}_{i_d,p_d} : \boldsymbol{i} \in \mathbf{1..n}\right\}.$$

Several properties of univariate B-spline (in particular non-negativity, partition of unity, local support, piecewise polynomials) generalize to multivariate B-spline. A set of multivariate B-splines defines a *multivariate spline space*:

$$S^{p_1,...,p_d}_{\boldsymbol{\alpha}_1,...,\boldsymbol{\alpha}_d}(\hat{\mathcal{M}}) = S^{\boldsymbol{p}}_{\boldsymbol{\alpha}}(\hat{\mathcal{M}}) := \text{span}\left\{\hat{B}_{\boldsymbol{i},\boldsymbol{p}}(\zeta) : \boldsymbol{i} \in \mathbf{1..n}\right\}$$

where $\boldsymbol{\alpha}_i$ is the regularity vectors of Ξ_i for all $i \in 1..d$ and $\boldsymbol{\alpha} = (\boldsymbol{\alpha}_1, ..., \boldsymbol{\alpha}_d)$. The multivariate spline space can be characterized as the linear space of piecewise polynomials of degree $\boldsymbol{p}$ and with regularity across the Bézier elements given by $\boldsymbol{\alpha}$. More precisely, if $\phi \in S^{\boldsymbol{p}}_{\boldsymbol{\alpha}}(\hat{\mathcal{M}})$ then $\phi|_Q \in \mathbb{P}_{\boldsymbol{p}}(Q)$ for all $Q \in \hat{\mathcal{M}}$ ($\mathbb{P}_{\boldsymbol{p}}(Q)$ is the space of tensor product polynomials on Q of degree p_i in the i-th direction for all $i \in 1..d$) and ϕ has α_{l,i_l} continuous derivatives in the l-th direction along the internal mesh faces:

$$\left\{(x_1, ..., x_d) : x_l = \zeta_{l,i_l}, x_{l'} \in (\zeta_{l',j_{l'}}, \zeta_{l',j_{l'}+1}), l' \neq l\right\}$$

for all $i_l \in 2..(m_l - 1)$, $j_{l'} \in 1..(m_{l'} - 1)$.
Moreover, the multivariate spline space can be related to the univariate spline spaces defined by the knot vectors $\{\Xi_i\}_{i=1}^d$ and degrees $\{p_i\}_{i=1}^d$ as $S^{\boldsymbol{p}}_{\boldsymbol{\alpha}}(\boldsymbol{\Xi}) = \bigotimes_{l=1}^d S^{p_l}_{\alpha_l}(\Xi_l)$.

3.3 B-spline geometries and B-splines in physical domain

Given a parametric mesh $\hat{\mathcal{M}}_h$ on the parametric domain $\hat{\Omega}$, consider the set $C^\infty_{\boldsymbol{\alpha}_1,...,\boldsymbol{\alpha}_d} = C^\infty_{\boldsymbol{\alpha}_1,...,\boldsymbol{\alpha}_d}(\hat{\mathcal{M}}_h)$ of functions that are infinitely-many times differentiable on the interior of any $Q \in \hat{\mathcal{M}}_h$ and whose inter-element regularity is described by $\boldsymbol{\alpha}_1, ..., \boldsymbol{\alpha}_d$ as specified in the previous section. Observe that $S^{\boldsymbol{p}}_{\boldsymbol{\alpha}_1,...,\boldsymbol{\alpha}_d}(\hat{\mathcal{M}}_h) \subset C^\infty_{\boldsymbol{\alpha}_1,...,\boldsymbol{\alpha}_d}(\hat{\mathcal{M}}_h)$.
Given a *physical domain* $\Omega \subset \mathbb{R}^d$, we assume the existence of a map $\boldsymbol{F} \in (C^\infty_{\boldsymbol{\alpha}_1,...,\boldsymbol{\alpha}_d}(\hat{\mathcal{M}}_h))^d$ such that $\boldsymbol{F}(\hat{\Omega}) = \Omega$, where we recall that $\hat{\Omega}$ is the parametric domain $(0,1)^d$. The mapping through $\boldsymbol{F}$ of the parametric Bézier mesh is called *(physical) Bézier mesh*:

$$\mathcal{M} := \left\{K \subset \Omega : K = \boldsymbol{F}(Q), Q \in \hat{\mathcal{M}}\right\}$$

and the elements $K \in \mathcal{M}$ are called *Bézier elements*. Analogously to the case of the parametric Bézier mesh, we associate to each $K = \boldsymbol{F}(Q) \in \mathcal{M}$ an *element size* $h_K := \|\boldsymbol{F}\|_{L^\infty(Q)} h_Q$ and a *mesh size* $h := \max\{h_K : K \in \mathcal{M}\}$ that may appear explicitly in the mesh symbol as $\mathcal{M}_h$. We also introduce the *shape-regularity constant* as the maximum positive constant λ that satisfies:

$$\lambda \leq \frac{\min_{K \in \mathcal{M}} h_K}{h}$$

In order to prevent the presence of singularities in the mapping $\boldsymbol{F}$ the following properties are assumed:

- $\boldsymbol{F} : \hat{\Omega} \to \Omega$ is a bi-Lipschitz homeomorphism;
- $\boldsymbol{F}|_{\bar{Q}} \in C^\infty(\bar{Q})$ for all $Q \in \hat{\mathcal{M}}$;
- $\boldsymbol{F}^{-1}|_{\bar{K}} \in C^\infty(\bar{K})$ for all $K \in \mathcal{M}$.

We define the set of *parametric mesh faces* $\hat{\mathcal{F}}_h := \{\hat{F}\}$ composed of the faces of the parametric Bézier elements. The set of *(physical) mesh faces* is defined as the mapping of the parametric mesh faces to the physical domain:

$$\mathcal{F}_h := \left\{F = \boldsymbol{F}(\hat{F}) : \hat{F} \in \hat{\mathcal{F}}_h\right\}.$$

The subset $\Gamma_h := \{F \in \mathcal{F}_h : F \cap \partial\Omega \neq \emptyset\}$ is the *boundary mesh* and forms a partition on $\partial\Omega$:

$$\partial\Omega = \bigcup_{F \in \Gamma_h} \bar{F}.$$

To any $F \in \Gamma_h$ a *face-size* is associated as $h_F := h_K$ where $K \in \mathcal{M}_h$ is the unique element such that $F \in \partial K$.
The mapping through $\boldsymbol{F}$ of a multivariate spline space in the parametric domain $\hat{V}_h := S^{\boldsymbol{p}}_{\boldsymbol{\alpha}}(\hat{\mathcal{M}}_h)$ defines an *isogeometric discrete space*:

$$V_h := \left\{ v := \iota(\hat{u}) : \hat{u} \in \hat{V}_h \right\}$$

where we have explicitly expressed the mesh-size h associated to the mesh $\mathcal{M}_h$. A basis for V_h is given by the mapping through $\boldsymbol{F}$ of $\left\{ \hat{B}_{\boldsymbol{i},\boldsymbol{p}} \right\}_{\boldsymbol{i} \in \boldsymbol{I}}$:

$$V_h = \operatorname{span} \left\{ B_{\boldsymbol{i},\boldsymbol{p}} := \hat{B}_{\boldsymbol{i},\boldsymbol{p}} \circ \boldsymbol{F}^{-1} \ \forall \boldsymbol{i} \in \boldsymbol{1..n} \right\}$$

3.4 The Stokes problem

Consider a domain $\Omega \subset \mathbb{R}^d$ whose boundary is partitioned as $\partial\Omega = \Gamma_D \cup \Gamma_N$, $\Gamma_D \cap \Gamma_N = \emptyset$ and the kinematic viscosity $\nu : \Omega \to \mathbb{R}$, the forcing term $\boldsymbol{f} : \Omega \to \mathbb{R}^d$, the Dirichlet datum $\boldsymbol{g}_D : \Gamma_D \to \mathbb{R}^d$ and the Neumann datum $\boldsymbol{g}_N : \Gamma_N \to \mathbb{R}^d$.
We consider the *Stokes problem*:
Find $\boldsymbol{v} : \Omega \to \mathbb{R}^d, p : \Omega \to \mathbb{R}$ such that:

$$\begin{cases} -\nu \Delta \boldsymbol{u} + \nabla p = \boldsymbol{f} & \text{in } \Omega \\ \boldsymbol{\nabla} \cdot \boldsymbol{u} = 0 & \text{in } \Omega \\ \boldsymbol{u} = \boldsymbol{g}_D & \text{on } \Gamma_D \\ \dfrac{\partial \boldsymbol{u}}{\partial \boldsymbol{n}} - p\boldsymbol{n} = \boldsymbol{g}_N & \text{on } \Gamma_N \end{cases} . \tag{3.1}$$

In order to state the weak formulation of the Stokes problem , define $V := H^1(\Omega)$ and $Q := L^2(\Omega)$. Also consider $V_{\Gamma_D} := \left\{ \boldsymbol{v} \in \left(H^1(\Omega)\right)^d : \boldsymbol{v}|_{\Gamma_D} = \boldsymbol{g}_D \right\}$ which, being a closed subset of $\left(H^1(\Omega)\right)^d$, is a Hilbert spaces if equipped with the $\left(H^1(\Omega)\right)^d$ norm. Let now $\nu \in W^{1,\infty}(\Omega)$, $\boldsymbol{f} \in \left(H^{-1}(\Omega)\right)^d$, $\boldsymbol{g}_D \in \left(H^{1/2}(\Omega)\right)^d$ and $\boldsymbol{g}_N \in \left(H^{-1/2}(\Omega)\right)^d$. Moreover, recall from Chapter 2 that $(\cdot,\cdot)$ is the $L^2(\Omega)$ scalar product and $(\cdot,\cdot)_{\Gamma_D}$ the $L^2(\Gamma_D)$ scalar product. The *weak formulation* of the Stokes problem reads:
Find $\boldsymbol{u} \in V_{\boldsymbol{g}_D}, q \in Q$ such that

$$\begin{cases} \nu\left(\nabla \boldsymbol{u}, \nabla \boldsymbol{v}\right) - \left(\boldsymbol{\nabla} \cdot \boldsymbol{v}, p\right) = \left(\boldsymbol{f}, \boldsymbol{v}\right) + \left(\boldsymbol{g}_N, \boldsymbol{v}\right)_{\Gamma_N} & \forall \boldsymbol{v} \in V_0 \\ \left(\boldsymbol{\nabla} \cdot u, q\right) = 0 & \forall q \in Q \end{cases} .$$

The same problem can be reformulated more synthetically as:
Find $\boldsymbol{u} \in V_{\boldsymbol{g}_D}, p \in Q$ such that

$$\begin{cases} a(\boldsymbol{u}, \boldsymbol{v}) + b(\boldsymbol{v}, p) = F(\boldsymbol{v}) & \forall \boldsymbol{v} \in V_0 \\ b(\boldsymbol{u}, q) = 0 & \forall q \in Q \end{cases} . \tag{3.2}$$

where in the case of the Stokes problem

$$\begin{aligned} &a(\boldsymbol{u}, \boldsymbol{v}) := \nu\left(\nabla \boldsymbol{u}, \nabla \boldsymbol{v}\right) \ \forall \boldsymbol{u}, \boldsymbol{v} \in V, \\ &b(\boldsymbol{v}, q) := -\left(\boldsymbol{\nabla} \cdot \boldsymbol{v}, q\right) \ \forall \boldsymbol{v} \in V, q \in Q, \\ &F(\boldsymbol{v}) := \left(\boldsymbol{f}, \boldsymbol{v}\right) + \left(\boldsymbol{g}_N, \boldsymbol{v}\right)_{\Gamma_N} \ \forall \boldsymbol{v} \in V. \end{aligned} \tag{3.3}$$

The following result gives sufficient conditions for a problem in the abstract form (3.2) to be well posed.

Theorem 1. *Consider a problem in the form (3.2) where* $(V, \|\cdot\|_V), (Q, \|\cdot\|_Q)$ *are Hilbert spaces and* $a : V \times V \to \mathbb{R}$, $b : V \times Q \to \mathbb{R}$ *are continuous bilinear forms,* $F : V \to \mathbb{R}$ *is linear and continuous. If:*

- $a(\cdot,\cdot)$ *is coercive on* $V_{\ker B} := \{\boldsymbol{v} \in V : b(\boldsymbol{v}, q) = 0 \ \forall q \in Q\}$*:*

$$\exists \alpha > 0 : a(\boldsymbol{v}, \boldsymbol{v}) \geq \alpha \|\boldsymbol{v}\|_V \qquad \forall \boldsymbol{v} \in V_{\ker B} \tag{3.4}$$

- *the* inf-sup condition *is satisfied:*

$$\exists \beta > 0 : \inf_{q \in Q} \sup_{\boldsymbol{v} \in V} \frac{b(\boldsymbol{v}, q)}{\|\boldsymbol{v}\|_V \|q\|_Q} \geq \beta \tag{3.5}$$

then it exists a unique solution $(\boldsymbol{u}, p) \in V \times Q$ *to problem (3.2) and it satisfies:*

$$\exists C > 0 : \|\boldsymbol{u}\|_V + \|p\|_Q \leq C \|F\|_{V'}$$

Proof. See [3, Theorem 4.2.3] □

This theorem can be applied to the Stokes problem to prove its well posedness. Observe that the bilinear form $a(\cdot,\cdot)$ is actually coercive on V.
The case in which no Neumann boundary condition is enforced ($\Gamma_N = \emptyset$) needs special attention. As the pressure p appears only through its gradient, if $p \in L^2(\Omega)$ is a solution, then also $p + \gamma$, $\gamma \in \mathbb{R}$ is. Therefore, in this case the mean of p is set to zero ($\int_\Omega p \mathrm{d}x = 0$), which corresponds to looking for a solution $p \in L^2_0(\Omega)$.
An alternative to the abstract formulation (3.2) is:
Find $u \in \mathcal{U}$ such that:

$$\mathcal{A}(u, v) = \mathcal{F}(v) \qquad \forall v \in \mathcal{V}, \tag{3.6}$$

where, in the case of the Stokes problem,

$$\begin{aligned} \mathcal{U} &:= V_{\boldsymbol{g}_D} \times Q, \\ \mathcal{V} &:= V_0 \times Q, \\ \mathcal{A}(u, v) = \mathcal{A}((\boldsymbol{u}, p), (\boldsymbol{v}, q)) &:= a(\boldsymbol{u}, \boldsymbol{v}) + b(\boldsymbol{v}, p) + b(\boldsymbol{u}, q), \qquad (3.7) \\ \forall u = (\boldsymbol{u}, p) \in \mathcal{U}, v &= (\boldsymbol{v}, q) \in \mathcal{V}, \\ \mathcal{F}(v) = \mathcal{F}((\boldsymbol{v}, q)) &:= F(\boldsymbol{v}) \qquad \forall v = (\boldsymbol{v}, q) \in \mathcal{V}. \qquad (3.8) \end{aligned}$$

The following theorem gives necessary and sufficient conditions for the well-posedness of problems in the form (3.6).

Theorem 2. *Consider a problem in the form (3.6), where* $(\mathcal{U}, \|\cdot\|_{\mathcal{U}}), (\mathcal{V}, \|\cdot\|_{\mathcal{V}})$ *are Hilbert spaces,* $\mathcal{A} : \mathcal{U} \times \mathcal{V} \to \mathbb{R}$ *is a continuous bilinear form and* $\mathcal{F} : \mathcal{V} \to \mathbb{R}$ *is continuous and linear. If the following conditions hold:*

$$\inf_{u \in \mathcal{U}} \sup_{v \in \mathcal{V}} \frac{\mathcal{A}(u, v)}{\|u\|_{\mathcal{U}} \|v\|_{\mathcal{V}}} > 0, \quad \inf_{v \in \mathcal{V}} \sup_{u \in \mathcal{U}} \frac{\mathcal{A}(u, v)}{\|u\|_{\mathcal{U}} \|v\|_{\mathcal{V}}} > 0$$

then

$$\inf_{u \in \mathcal{U}} \sup_{v \in \mathcal{V}} \frac{\mathcal{A}(u, v)}{\|u\|_{\mathcal{U}} \|v\|_{\mathcal{V}}} = \inf_{v \in \mathcal{V}} \sup_{u \in \mathcal{U}} \frac{\mathcal{A}(u, v)}{\|u\|_{\mathcal{U}} \|v\|_{\mathcal{V}}} \equiv \alpha > 0$$

and it exists a unique solution $u \in \mathcal{U}$ *to problem (3.6) satisfying:*

$$\|u\|_{\mathcal{U}} \leq \frac{\|\mathcal{F}\|_{\mathcal{V}'}}{\alpha}.$$

Proof. see [2]. □

3.5 Discretization of the Stokes problem

We first present the Galerkin approximation of the abstract problem (3.2) and sufficient conditions for its well-posedness.
Consider finite dimensional linear subspaces $V_h \subset V$ and $Q_h \subset Q$ parametrized by $h \in \mathbb{R}_{>0}$ with the approximation property:

$$\lim_{h\to 0} \inf_{v_h \in V_h} \|v - v_h\|_V = 0 \qquad \forall v \in V$$
$$\lim_{h\to 0} \inf_{q_h \in Q_h} \|q - q_h\|_Q = 0 \qquad \forall q \in Q.$$

Let moreover $V_{\boldsymbol{g}_D,h}$ and $V_{0,h}$ be analogous approximations of $V_{\boldsymbol{g}_D}$ and V_0 respectively. We can consider the *discrete problem*:
Find $\boldsymbol{u}_h \in V_{\boldsymbol{g}_D,h}, p_h \in Q_h$ such that

$$\begin{cases} a(\boldsymbol{u}_h, \boldsymbol{v}_h) + b(\boldsymbol{v}_h, p_h) = F(\boldsymbol{v}_h) & \forall \boldsymbol{v}_h \in V_{0,h} \\ b(\boldsymbol{u}_h, q_h) = 0 & \forall q_h \in Q_h \end{cases}. \tag{3.9}$$

A well-posedness theorem analogous to Theorem 1 can be stated:

Theorem 3. *Assume that the hypotheses of Theorem 1 are satisfied and that are given finite-dimensional subspaces $V_h \subset V$ and $Q_h \subset Q$. Consider a problem in the form (3.9). If:*

- *$a(\cdot,\cdot)$ is uniformly (with respect to h) coercive on $V_{\ker B,h}$:*

$$\exists \alpha > 0 : \forall h > 0 \; a(\boldsymbol{v}_h, \boldsymbol{v}_h) \geq \alpha \|\boldsymbol{v}_h\|_V \qquad \forall \boldsymbol{v}_h \in V_{\ker B,h} \tag{3.10}$$

  where

$$V_{\ker B,h} := \{\boldsymbol{v}_h \in V_h : b(\boldsymbol{v}_h, q_h) = 0 \; \forall q_h \in Q_h\}$$

- *the* inf-sup condition *is satisfied uniformly with respect to h:*

$$\exists \beta > 0 : \forall h > 0 \inf_{q_h \in Q_h} \sup_{\boldsymbol{v}_h \in V_h} \frac{b(\boldsymbol{v}_h, q_h)}{\|\boldsymbol{v}_h\|_V \|q_h\|_Q} \geq \beta \tag{3.11}$$

then it exists a unique solution $(\boldsymbol{u}_h, p_h) \in V_{\boldsymbol{g}_D,h} \times Q_h$ which satisfies:

$$\exists C > 0 : \|\boldsymbol{u}_h\|_V + \|p_h\|_Q \leq C \|F\|_{V'}$$

as well as the following error estimate:

$$\exists C > 0 : \; \|u - u_h\|_V + \|p - p_h\|_Q \leq C \left(\inf_{v_h \in V_h} \|u - v_h\|_V + \inf_{q_h \in Q_h} \|p - q_h\|_Q \right)$$

Proof. [3, Theorem 5.2.5] □

In general, the well posedness of the continuous abstract problem (3.2) does not imply the well-posedness of the discrete problem (3.9). In facts, $V_{\ker B,h}$ may not be a subset of $V_{\ker B}$, therefore the continuous coercivity (3.4) may not imply the discrete one (3.10). Analogously, the continuous inf-sup condition (3.5) may not imply the discrete one (3.11). In the case of the Stokes problem, as the bilinear form $a(\cdot,\cdot)$ is coercive on V, the coercivity condition is satisfied. However, the validity of the inf-sup condition depends on the choice of the finite dimensional spaces V_h, Q_h.

Analogously to the continuous case, problem (3.9) can be formulated as:
Find $u_h \in \mathcal{U}_h$ such that:

$$\mathcal{A}(u_h, v_h) = \mathcal{F}(v_h) \qquad \forall v_h \in \mathcal{V}_h \tag{3.12}$$

where, in the case of the discrete Stokes problem,

$$\begin{aligned} \mathcal{U}_h &:= V_{\boldsymbol{g}_D,h} \times Q_h, \\ \mathcal{V}_h &:= V_{0,h} \times Q_h, \end{aligned}$$

$\mathcal{A}$ and $\mathcal{F}$ are defined in (3.7) and (3.8) respectively.
Sufficient conditions for the well-posedness of the projection problem (3.12) are given in the following theorem.

Theorem 4. *Assume the hypotheses of Theorem 2 are satisfied and are given finite dimensional subspaces $\mathcal{U}_h \subset \mathcal{U}$, $\mathcal{V}_h \subset \mathcal{V}$. If moreover the following condition holds:*

$$\exists \beta > 0 : \forall h > 0 \inf_{u \in \mathcal{U}_h} \sup_{v \in \mathcal{V}_h} \frac{\mathcal{A}(u, v)}{\|u\|_{\mathcal{U}} \|v\|_{\mathcal{V}}} \geq \beta \tag{3.13}$$

then it exists a unique solution $u_h \in \mathcal{U}_h$ that satisfies:

$$\|u\|_{\mathcal{U}} \leq \frac{\|\mathcal{F}\|_{\mathcal{V}'}}{\beta}$$

as well as the following approximation estimate:

$$\|u - u_h\|_{\mathcal{U}} \leq \left(1 + \frac{\|\mathcal{A}\|}{\beta}\right) \inf_{w_h \in \mathcal{V}} \|u - w_h\|_{\mathcal{U}}.$$

Proof. see [2]. □

Observe that if $\mathcal{U}_h = \mathcal{V}_h$ the condition (3.13) can be substituted by the stronger coercivity condition:

$$\exists \tilde{\beta} > 0 : \forall h > 0, u \in \mathcal{U}_h \quad \mathcal{A}(u, u) \geq \tilde{\beta} \|u\|_{\mathcal{U}}^2. \tag{3.14}$$

Indeed:

$$\inf_{u \in \mathcal{U}_h} \sup_{v \in \mathcal{U}_h} \frac{\mathcal{A}(u, v)}{\|u\|_{\mathcal{U}} \|v\|_{\mathcal{V}}} \geq \inf_{u \in \mathcal{U}_h} \frac{\mathcal{A}(u, u)}{\|u\|_{\mathcal{U}}^2} \geq \tilde{\beta}.$$

In order to distinguish the discrete inf-sup condition (3.13) on $\mathcal{A}(\cdot, \cdot)$ from the one (3.11) on $b(\cdot, \cdot)$, we will refer to the former as *global inf-sup condition* and to the quantity β appearing in Theorem 4 as *global inf-sup constant*. Analogously, if we refer to the continuity of $\mathcal{A}(\cdot, \cdot)$ we will write *global continuity* and refer to its continuity constant as *global continuity constant*. Analogously, condition (3.14) will be called *global coercivity* and the quantity $\tilde{\beta}$ *global coercivity constant*.

3.5.1 Taylor-Hood isogeometric elements

The family of Taylor-Hood isogeometric elements is defined as follows:

$$\begin{aligned} \hat{V}_h^{\mathrm{TH}} &= \hat{V}_h^{\mathrm{TH}}(p, \alpha) := S_{\alpha,\alpha}^{p+1,p+1}(\hat{\mathcal{M}}_h) \times S_{\alpha,\alpha}^{p+1,p+1}(\hat{\mathcal{M}}_h), \\ \hat{Q}_h^{\mathrm{TH}} &= \hat{Q}_h^{\mathrm{TH}}(p, \alpha) := S_{\alpha,\alpha}^{p,p}(\hat{\mathcal{M}}_h) \end{aligned} \tag{3.15}$$

for given degree p and regularity $\alpha \in 0..p-1$. The choice $\alpha = 0$ leads to the classical Taylor-Hood finite elements family. The definition of Taylor-Hood spaces in the physical domain is

$$V_h^{TH} := \left\{ \boldsymbol{v} = \hat{\boldsymbol{v}} \circ \boldsymbol{F}^{-1} \ \forall \hat{\boldsymbol{v}} \in \hat{V}_h^{\mathrm{TH}} \right\},$$
$$Q_h^{TH} := \left\{ q = \hat{q} \circ \boldsymbol{F}^{-1} \ \forall \hat{q} \in \hat{Q}_h^{\mathrm{TH}} \right\}.$$

A proof of the inf-sup stability of the isogeometric Taylor-Hood discretization of the Stokes problem can be found in [4]. As for convergence, the following convergence estimates are a consequence of the results in [4] and can be observed numerically:

$$\|\boldsymbol{u} - \boldsymbol{u}_h\|_{H^1(\Omega)} = \mathcal{O}(h^{p+1})$$
$$\|p - p_h\|_{L^2(\Omega)} = \mathcal{O}(h^{p+1})$$

3.5.2 Raviart-Thomas isogeometric elements

The family of Raviart-Thomas isogeometric elements is defined as follows:

$$\begin{aligned} \hat{V}_h^{\mathrm{RT}} &= \hat{V}_h^{\mathrm{RT}}(p,\alpha) := S^{p+1,p}_{\alpha+1,\alpha}(\hat{\mathcal{M}}_h) \times S^{p,p+1}_{\alpha,\alpha+1}(\hat{\mathcal{M}}_h), \\ \hat{Q}_h^{\mathrm{RT}} &= \hat{Q}_h^{\mathrm{RT}}(p,\alpha) := S^{p,p}_{\alpha,\alpha}(\hat{\mathcal{M}}_h) \end{aligned} \tag{3.16}$$

for given degree p and regularity $\alpha \in 0..p-1$. The choice $\alpha = -1$ (corresponding to discontinuous splines across elements) is avoided, as it would lead to a nonconforming discretization. Spaces with boundary conditions can also be defined as:

$$\hat{V}_{0,h}^{\mathrm{RT}} := \left\{ \hat{\boldsymbol{v}}_h \in \hat{V}_h^{\mathrm{RT}} : \hat{\boldsymbol{v}}_h \cdot \boldsymbol{n} = 0 \text{ on } \partial\hat{\Omega} \right\}$$
$$\hat{Q}_{0,h}^{\mathrm{RT}} := \left\{ \hat{q}_h \in \hat{Q}_h^{\mathrm{RT}} : \int_{\hat{\Omega}} \hat{q}_h \mathrm{d}x = 0 \right\}.$$

In the case of the spaces (3.16) (analogously for the spaces with boundary conditions), the functional space in the physical domain are defined as:

$$V_h^{\mathrm{RT}} := \left\{ \boldsymbol{v} = \iota_V(\hat{\boldsymbol{v}}) : \hat{\boldsymbol{v}} \in \hat{V}_h^{\mathrm{RT}} \right\}$$
$$Q_h^{\mathrm{RT}} := \left\{ q = \iota_Q(\hat{q}) : \hat{q} \in \hat{Q}_h^{\mathrm{RT}} \right\}.$$

where the parametric-to-physical domain maps ι_V, ι_Q are defined as:

$$\iota_V(\hat{v}) := \frac{D\boldsymbol{F}}{\det(D\boldsymbol{F})}(\hat{\boldsymbol{v}} \circ \boldsymbol{F}^{-1}) \quad \forall \hat{v} \in \hat{V}_h^{\mathrm{RT}} \tag{3.17}$$
$$\iota_Q(\hat{q}) := \det(D\boldsymbol{F})^{-1}(\hat{q} \circ \boldsymbol{F}^{-1}) \quad \forall \hat{q} \in \hat{Q}_{0,h}^{\mathrm{RT}} \tag{3.18}$$

where (3.17) is the *Piola transform*.
The definition of isogeometric Raviart-Thomas elements is motivated by the theory of isogeometric discrete differential forms [7]. We report here some of the main definition and results concerning their application to the Stokes problem. More detailed treatises can be found in [5] and [13].
The Raviart-Thomas isogeometric elements have the property of producing a numerical solution that is exactly divergence-free thanks to the following fact:

Proposition 1. *If* $\boldsymbol{v}_h \in V_h^{RT}$ *and*

$$(\boldsymbol{\nabla} \cdot \boldsymbol{v}_h, q_h) = 0 \quad \forall q_h \in Q_h$$

then $\boldsymbol{\nabla} \cdot \boldsymbol{v}_h \equiv 0$. *Moreover, if* $\boldsymbol{v}_h \in V_{0,h}^{RT}$ *and*

$$(\boldsymbol{\nabla} \cdot \boldsymbol{v}_h, q_h) = 0 \quad \forall q_h \in Q_{0,h}^{RT}$$

then $\boldsymbol{\nabla} \cdot \boldsymbol{v}_h \equiv 0$.

Proof. see [13, Proposition 5.4.2] □

Considered this fact, the maps (3.17) and (3.18) are chosen because of their divergence and integral-preserving properties, i.e

$$\boldsymbol{\nabla} \cdot (\iota_V(\hat{v})) = \widehat{\boldsymbol{\nabla}\cdot}\hat{v} \quad \forall \hat{v} \in \hat{V}_h^{\mathrm{RT}},$$
$$\int_\Omega \iota_Q(\hat{q})\mathrm{d}x = 0 \Leftrightarrow \int_{\hat{\Omega}} \hat{q}\mathrm{d}x = 0 \quad \forall \hat{q} \in \hat{Q}_h^{\mathrm{RT}}.$$

As the construction of Raviart-Thomas spaces with both normal and tangential Dirichlet boundary conditions is not as simple, it is preferred to impose the normal one strongly and the tangential one weakly through Nitsche's method (see [14],[18]):
Find $\boldsymbol{u} \in V_{0,h}^{\mathrm{RT}}, p \in Q_{0,h}^{\mathrm{RT}}$ such that:

$$\begin{cases} a_h(\boldsymbol{u}, \boldsymbol{v}) + b(\boldsymbol{v}, p) = F_h(\boldsymbol{v}) & \forall \boldsymbol{v} \in V_{0,h}^{\mathrm{RT}} \\ b(\boldsymbol{u}, q) = 0 & \forall q \in Q_{0,h}^{\mathrm{RT}} \end{cases}. \tag{3.19}$$

where

$$a_h(\boldsymbol{u}, \boldsymbol{v}) := (\mu \nabla \boldsymbol{u}, \nabla \boldsymbol{v}) - \left(\mu \frac{\partial \boldsymbol{u}}{\partial \boldsymbol{n}}, \boldsymbol{v}\right)_{\Gamma_D} - \left(\mu \frac{\partial \boldsymbol{v}}{\partial \boldsymbol{n}}, \boldsymbol{u}\right)_{\Gamma_D} + C_{pen}\left(\frac{\mu}{H}\boldsymbol{u}, \boldsymbol{v}\right)_{\Gamma_D} \quad \forall \boldsymbol{u}, \boldsymbol{v} \in V_{0,h}^{\mathrm{RT}},$$
$$F_h(\boldsymbol{v}) := (\boldsymbol{f}, \boldsymbol{v}) + (\boldsymbol{g_N}, \boldsymbol{v})_{\Gamma_N} - \left(\mu \frac{\partial \boldsymbol{v}}{\partial \boldsymbol{n}}, \boldsymbol{g_D}\right)_{\Gamma_D} + C_{pen}\left(\frac{\mu}{H}\boldsymbol{g_D}, \boldsymbol{v}\right)_{K \cap \Gamma_D} \quad \forall \boldsymbol{v} \in V_{0,h}^{\mathrm{RT}}$$

and $b(\cdot,\cdot)$ is defined in (3.3). Here $H : \partial\Omega \to \mathbb{R}_{>0}$ is a piecewise-constant function such that $h|_F := h_F \ \forall F \in \Gamma_h$ and C_{pen} is a constant. A proof of the stability of problem (3.19) can be found in [13, chapter 6] and implies that the method is of order h^p, i.e.

$$\|\boldsymbol{u} - \boldsymbol{u}_h\|_{H^1(\Omega)} + \|p - p_h\|_{L^2(\Omega)} = \mathcal{O}(h^p)$$

On the other hand, the following convergence estimates are observed in numerical experiments:

$$\|\boldsymbol{u} - \boldsymbol{u}_h\|_{H^1(\Omega)} = \mathcal{O}(h^p),$$
$$\|p - p_h\|_{L^2(\Omega)} = \mathcal{O}(h^{p+1}).$$

Chapter 4

Trimmed isogeometric discretization of the Poisson problem

In the present chapter we introduce trimming. In the first section we follow [16] to give some general notion on trimming in CAGD and present some of the main difficulties that arise from the attempt to develop isogeometric methods to approximate boundary value problems on trimmed domains. In the second section we introduce a notation for the description of domains obtained by trimming. In the third section the Poisson problem is considered to show more in detail how the discretization is adapted in the case of trimmed problems. In addition, the main numerical issues that arise from the adoption of this framework are highlighted with an emphasis on stability. Finally, in the fourth and last section a minimal stabilization technique aimed at correcting the stability problems is introduced. The content of the last two sections is based on the work that will appear in [6].

4.1 Trimming

Trimming is a fundamental operation in CAGD (Computer-Aided Geometric Design) that allows the representation of complex objects. However, it is also a major obstacle to the integration of CAGD and numerical simulation.
In modern CAGD tools, a 3D object is stored through its *boundary presentation* (*B-rep*), a collection of geometrical and topological pieces of information about its boundary. The geometrical information consists of a collection of boundary-patches described by tensor-product NURBS surfaces. The topological information describes the relation between the boundary-patches through their connectivity giving information about vertices, edges and faces. Moreover, a given continuity may be required to connect two adjacent patches.
Trimming operations allow to cut away unwanted parts of the geometrical model. This is achieved through a change in the visualization of the object. As a consequence, the parametrization and mathematical description of the object remain essentially the same.
A trimmed B-rep object is usually obtained as a combination of primitives, rigid motions and boolean operations (union, intersection, difference) collected in a binary tree that allows to define the order in which these operations are performed to obtain the desired trimmed object starting from the primitives.
Some of the most relevant issues with trimming come from the fact that trimming operations cannot be performed exactly. On one hand, the use of floating-point arithmetic causes round-off errors that may propagate and cause inaccuracies in the description of the model. On the other hand, several operations are the result of numerical algorithms

(for instance, the problem of surface intersection is solved as a non-linear system of equations) that are solved up to a tolerance and therefore introduce additional errors. As a consequence, the representation of the object could present small gaps and overlaps of the boundary-patches that can be acceptable for visualization purposes but makes the model unsuitable as an input for numerical algorithms.
Attempts to employ trimmed geometries in isogometric analysis can be classified in global and local approaches. Global approaches consist in performing a remodelling stage before the numerical simulation. The remodelling is aimed at substituting the trimmed regions of the boundaries with regular patches that allow to apply the same numerical scheme used on untrimmed geometries. Conversely, local approaches employ directly the trimmed objects and therefore require a substantial adaptation of the numerical algorithm. In the present report we will present a local approach to trimming.
In local approaches, the fact that trimmed entities preserve the parametrization of the original untrimmed object is exploited (for instance, in the definition of shape functions). Knot spans can be classified in interior (located within the active part of the domain), exterior (located outside the active domain) and cut-elements (intersected by the trimming curve). Cut-elements require special attention in several stages of the numerical algorithm. A fundamental step is the classification of cut-elements depending on how they are cut by the trimming curve. Despite the fact that the trimming curve can cut elements in possibly complex patterns, this complexity decreases as the mesh is refined. Cut-elements classification is needed for the integration of shape functions, an operation that also requires dedicated quadrature rules. Another problem is the imposition of essential boundary conditions on the trimming curve, that arises from the fact that the definition of shape functions is based on the untrimmed description of the domain. Finally, depending on the relative position of elements and trimming curve the problem may result unstable and ill-conditioned. These problems require the development of stabilization and preconditioning techniques that reduce the sensitivity of the numerical scheme on the relative position of mesh and trimming curve. Finally, we remark that local approaches share several features of *fictitious boundary methods*, such as CUT-FEM [9] and finite-cell method [12]. Therefore, the literature on these numerical methods may suggest solutions to problem in trimmed isogeometric analysis.

4.2 Notation for trimmed problems

In order to describe the modifications in the method needed because of the presence of trimming, we first alter and enrich the notation established in the previous chapter.
Consider a domain $\Omega_0 \subset \mathbb{R}^2$ and a parametric-to-physical mapping $\boldsymbol{F} : \hat{\Omega}_0 \to \Omega_0$ as in section 3.3 where by $\hat{\Omega}_0 = (0,1) \times (0,1)$ we denote the parametric domain. Let $\hat{\mathcal{M}}_0$ and $\mathcal{M}_0$ be the corresponding parametric and physical Bézier mesh respectively.
In general, the *trimmed physical domain* is defined as $\Omega := \Omega_0 \setminus \bigcup_{i=1}^{N} \overline{\Omega}_i$ where $\{\Omega_i\}_{i=1}^{N}$ is a set of open connected subsets of Ω. We restrict ourself to the case $N = 1$, therefore $\Omega = \Omega_0 \setminus \overline{\Omega}_1$. The *trimming curve* is defined as $T := \Omega_0 \cap \partial\Omega_1$.
Consider the new *parametric domain* $\hat{\Omega} := \boldsymbol{F}^{-1}(\Omega)$, where $\boldsymbol{F}$ remains the parametric-to-physical mapping as above. The new *parametric Bézier mesh* is

$$\hat{\mathcal{M}}_h := \left\{ Q \in \hat{\mathcal{M}}_0 : Q \cap \Omega \neq \emptyset \right\}.$$

The new *physical Bézier mesh* is defined as $\mathcal{M}_h := \left\{ \boldsymbol{F}(Q) : Q \in \hat{\mathcal{M}}_h \right\}$. We also define the *Bézier cut-elements*, $\mathcal{G}_h := \{K \in \mathcal{M} : K \cap T \neq \emptyset\}$.
Finally, given a spline-space $V_h = \text{span}\{B_{\boldsymbol{i},\boldsymbol{p}}, \boldsymbol{i} \in \boldsymbol{1..n}\}$ on the untrimmed mesh $\mathcal{M}$, we

define the *trimmed splines-space*:

$$\tilde{V}_h = \text{span}\{B_{\boldsymbol{i},\boldsymbol{p}}|_\Omega, \boldsymbol{i} \in \boldsymbol{1..n}\} \tag{4.1}$$

obtained by the restriction to the domain Ω of the basis of V_h.

4.3 Effect of trimming on stability

Let us first consider the Poisson problem defined on a trimmed domain Ω obtained as defined in the previous section.
Consider $f : \Omega \to \mathbb{R}$, a partition $\{\Gamma_D, \Gamma_N\}$ of $\partial\Omega$ where the Dirichlet and Neumann boundary conditions, $g_D : \Gamma_D \to \mathbb{R}$ and $g_N : \Gamma_N \to \mathbb{R}$ respectively, are imposed. The problem reads:
Find $u : \Omega \to \mathbb{R}$ such that:

$$\begin{cases} -\Delta u = f & \text{in } \Omega \\ u = g_D & \text{on } \Gamma_D \\ \dfrac{\partial u}{\partial \boldsymbol{n}} = g_N & \text{on } \Gamma_N \end{cases}.$$

Consider now $f \in H^{-1}(\Omega)$, $g_D \in h^{\frac{1}{2}}(\Gamma_D)$ and $g_N \in h^{-\frac{1}{2}}(\Gamma_N)$ and define $V := H^1(\Omega)$, $V_{g_D} := \left\{v \in V : v_{|\Gamma_D} = g_D\right\}$ and , $V_0 := \left\{v \in V : v_{|\Gamma_D} = 0\right\}$. The weak formulation of the Poisson problem reads:
Find $u \in V_{g_D}$ such that:

$$(\nabla u, \nabla v) = (f, v) + (g_N, v)_{\Gamma_N} \qquad \forall v \in V_0 \tag{4.2}$$

If $T \cap \Gamma_D \neq \emptyset$, enforcing Dirichlet boundary conditions "strongly" becomes cumbersome because of the choice of the basis functions (4.1). Therefore, instead of (4.2), we opt for the *symmetric Nitsche formulation* (see [14],[18]):
Find $u \in V$ such that:

$$a(u, v) = F(v) \qquad \forall v \in V, \tag{4.3}$$

where:

$$a(u, v) := (\nabla u, \nabla v) - \left(\frac{\partial u}{\partial n}, v\right)_{\Gamma_D} - \left(u, \frac{\partial v}{\partial n}\right)_{\Gamma_D} + C_{pen}\,(u, v)_{\Gamma_D} \quad \forall u, v \in V,$$
$$F(v) := (f, v) + (g_N, v)_{\Gamma_N} - \left(g_D, \frac{\partial v}{\partial n}\right)_{\Gamma_D} + C_{pen}\,(g_D, v)_{\Gamma_D} \quad \forall v \; inV$$

and $C_{pen} > 0$ is a given parameter.
The present formulation allows the *weak* enforcement of Dirichlet boundary conditions (through the formulation of the problem rather than the functional space where the solution is sought). In addition, it is symmetric, consistent and, provided $C_{pen} > 0$ is big enough, coercive.
Given a trimmed spline-space $\tilde{V}_h$ defined as in (4.1), the discretization of problem (4.3) reads:
Find $u_h \in \tilde{V}_h$ such that:

$$a_h(u_h, v_h) = F_h(v_h) \qquad \forall v_h \in \tilde{V}_h \tag{4.4}$$

where:

$$a_h(u, v) := (\nabla u, \nabla v) - \left(\frac{\partial u}{\partial n}, v\right)_{\Gamma_D} - \left(u, \frac{\partial v}{\partial n}\right)_{\Gamma_D} + C_{pen}\left(H^{-1}u, v\right)_{\Gamma_D} \quad \forall u, v \in \tilde{V}_h \tag{4.5}$$

$$F(v) := (f, v) + (g_N, v)_{\Gamma_N} - \left(g_D, \frac{\partial v}{\partial n}\right)_{\Gamma_D} + C_{pen}\left(H^{-1}g_D, v\right)_{\Gamma_D} \quad \forall v \in \tilde{V}_h \tag{4.6}$$

and $H : \partial\Omega \to \mathbb{R}_{>0}$ is a piecewise-constant function such that $H|_F := h_F \ \forall F \in \Gamma_h$.
We also introduce the following mesh-dependent norm:

$$\|v\|^2_{\tilde{V}_h} := \|\nabla v\|^2_{L^2(\Omega)} + \left\|H^{-\frac{1}{2}} v\right\|^2_{L^2(\Gamma_D)} \qquad \forall v \in \tilde{V}_h,$$

that is the natural norm for the analysis of problem.
A number of problems remain. In particular:

- problem (4.4) may be unstable (see [9], where the analogous CUT-FEM method is presented and [10] where it is applied to the Stokes problem);
- integration algorithms over $K \cap \Omega$ and over the boundaries $F = T \cap K$ for all $K \in \mathcal{G}_h$ need to be defined;
- problem (4.4) may be ill-conditioned, depending on the shape of the cut-elements (see [12], where the same problem is described for the analogous finite-cell method).

As for the stability issue, it can be proved that the operation that prevents stability is the evaluation of normal derivatives on the trimmed boundary T (appearing in the second and third term of 4.5 and in the third term of 4.6).
When for example looking at the continuity of the bilinear form, the second term of 4.5 can be bounded as:

$$\left(\frac{\partial u_h}{\partial n}, v_h\right)_{\Gamma_K} \leq \left\|H^{\frac{1}{2}} \frac{\partial u_h}{\partial n}\right\|_{L^2(\Gamma_K)} \left\|H^{-\frac{1}{2}} v_h\right\|_{L^2(\Gamma_K)} \quad \forall v_h \in \tilde{V}_h \ \forall K \in \mathcal{M}_h$$

where we define $\Gamma_K := \Gamma_D \cap K$ for all $K \in \mathcal{M}$. Therefore, the following trace-inequality would be desired:

$$\exists C > 0 : \left\|H^{\frac{1}{2}} \frac{\partial u_h}{\partial n}\right\|_{L^2(\Gamma_K)} \leq C \|\nabla v_h\|_{L^2(K\cap\Omega)} \ \forall v_h \in \tilde{V}_h$$

where the constant C does not depend on the relative position of K and Ω. However, a simple counter-example can be given for $p = 1$, so that $\nabla v_h|_K = c_K$ is a constant:

$$\begin{aligned}
\left\|\frac{\partial u_h}{\partial n}\right\|^2_{L^2(\Gamma_K)} &= \mathrm{mea}_{d-1}(\Gamma_K)|c_K|^2 \\
&= \frac{\mathrm{mea}_{d-1}(\Gamma_K)}{\mathrm{mea}_d(\Omega \cap K)} |c_K|^2 \int_{\Omega\cap K} 1 \mathrm{d}x \\
&= \frac{\mathrm{mea}_{d-1}(\Gamma_K)}{\mathrm{mea}_d(\Omega \cap K)} \int_{\Omega\cap K} |\nabla v_h|^2 \mathrm{d}x \\
&= \frac{\mathrm{mea}_{d-1}(\Gamma_K)}{\mathrm{mea}_d(\Omega \cap K)} \|\nabla v_h\|^2_{L^2(\Omega\cap K)}.
\end{aligned}$$

Therefore $C \geq h_K^{\frac{1}{2}} \frac{\mathrm{mea}_{d-1}(\Gamma_K)}{\mathrm{mea}_d(\Omega\cap K)}$ and the quantity on the right may be unbounded in the case of *sliver-cuts* as described in [11] (see figure 2(b)).

4.4 A minimal stabilization

Definition 1. *Let $\vartheta \in (0, 1]$. $K \in \mathcal{M}$ is a good element if*

$$\frac{mea_d(\Omega \cap K)}{mea_d(K)} \geq \vartheta.$$

Otherwise we call K a bad element.

Observe that if $K \in \mathcal{M}_h \setminus \mathcal{G}_h$ then K is a good element. We also define $\mathcal{G}_h^g$ the set of good cut-element, $\mathcal{G}_h^b$ the set of bad cut-element.
We assume that for any $K \in \mathcal{G}_h^b$ it exists a good element $K' \in \mathcal{M}_h$ such that K' is a neighbour of K (i.e. K and K' share at least a vertex). This hypothesis is always satisfied provided the mesh is sufficiently refined. The notion of neighbour can be relaxed as follows: K and K' are neighbours if and only if $\text{dist}(K, K') \leq Ch$, where $C > 0$ is a constant independent of h.
Consider an operator:

$$R_h : \tilde{V}_h \to L^2(\Gamma_D) \tag{4.7}$$

which, in a sense to be specified, approximates the normal derivative on of functions in $\tilde{V}_h$ on Γ_D. R_h can be used to define the problem:
Find $u_h \in \tilde{V}_h$ such that:

$$a_h^S(u_h, v_h) = F_h^S(v_h) \qquad \forall v_h \in \tilde{V}_h \tag{4.8}$$

where:

$$\begin{aligned} a_h^S(u,v) &:= (\nabla u, \nabla v) - (R_h(u), v)_{\Gamma_D} - (u, R_h(v))_{\Gamma_D} + C_{pen} \left(H^{-1}u, v\right)_{\Gamma_D} \quad \forall u, v \in \tilde{V}_h \\ F^S(v) &:= (f, v) + (g_N, v)_{\Gamma_N} - (g_D, R(v))_{\Gamma_D} + C_{pen} \left(H^{-1}g_D, v\right)_{\Gamma_D} \quad \forall v \in \tilde{V}_h. \end{aligned}$$

The following theorem gives sufficient condition for problem (4.8) to be well-posed.

Theorem 5. *Suppose $R_h : \tilde{V}_h \to L^2(\Gamma_D)$ satisfies the following property:*

$$\left\| h_K^{\frac{1}{2}} R_h(v) \right\|_{L^2(\Gamma_K)} \leq C \|v\|_{H^1(\Omega \cap K')} \quad \forall v \in \tilde{V}_h, \forall K \in \mathcal{G}_h$$

where $K' = K$ if $K \in \mathcal{G}_h^g$ and K' is a good neighbour of K if $K \in \mathcal{G}_h^b$. Then, problem (4.8) is well posed in the sense that the bilinear form $a_h^S(\cdot, \cdot)$ is coercive and continuous on $\tilde{V}_h$.

The following definition of the operator (4.7) is proposed:

$$R_h(v)|_K := R_K(v) \qquad \forall v \in \tilde{V}_h, K \in \mathcal{G}_h,$$

where:

- if $K \in \mathcal{G}_h^g$

$$R_K(v) := \frac{\partial (v|_K)}{\partial n} \qquad \forall v \in \tilde{V}_h;$$

- if $K = \boldsymbol{F}(Q) \in \mathcal{G}_h^b$, denoting $K' = \boldsymbol{F}(Q')$ a good neighbour of K

$$R_K(v) := \frac{\partial}{\partial n} \left(\mathcal{E}(\hat{v}|_{Q'}) \circ \boldsymbol{F}^{-1} \right) \qquad \forall v \in \tilde{V}_h,$$

  where $\hat{v} = v \circ \boldsymbol{F}$ and $\mathcal{E} : \mathbb{P}_p(Q') \to \mathbb{P}_p(Q \cup Q')$ is the polynomial extension operator.

It can be proved [6] that the proposed stabilization satisfies the hypotheses of Theorem 5, therefore leads to a well-posed discrete problem (4.8).

Chapter 5

Trimmed Taylor-Hood elements

In this chapter a numerical scheme based on the Taylor-Hood isogeometric elements is presented. Analogously to the case of the Poisson problem presented in the previous chapter, in the first section we define the trimmed Taylor-Hood space, then state the formulation of the problem with weak imposition of essential boundary conditions. In addition, the stabilization proposed at the end of the previous chapter is generalized in order to apply it to the problem at hand. In the second section, we give some details about the numerical estimation of the stability constant from theorems 3 and 4. In the third section, we apply the non-stabilized scheme to problems with Neumann and weak Dirichlet boundary conditions in order to assess its convergence and stability properties. Finally, in the fourth section the same stability and convergence tests are repeated for the stabilized scheme.

5.1 Problem formulation

Let us consider again the Stokes problem (3.1). As in section 4.2, we suppose an untrimmed domain $\Omega_0 = \boldsymbol{F}(\hat{\Omega}_0)$ is given with $\hat{\mathcal{M}}_{0,h}$, $\mathcal{M}_{0,h}$ parametric and physical Bèzier meshes respectively. The domain Ω is obtained by trimming Ω_0, the trimming curve is T. $\hat{\Omega} = \boldsymbol{F}^{-1}(\Omega)$ denotes the parametric domain, $\hat{\mathcal{M}}_h$ and $\mathcal{M}_h$ the parametric and physical Bézier mesh respectively, $\mathcal{G}_h$ the cut-elements.
We consider the Taylor-Hood isogeometric elements on Ω_0 with the Bèzier mesh $\mathcal{M}_{0,h}$ and recall their definition first given in section 3.5.1:

$$\begin{aligned}\hat{V}_h &= \hat{V}_h^{\mathrm{TH}}(p,\alpha) := S_{\alpha,\alpha}^{p+1,p+1}(\hat{\mathcal{M}}_{0,h}) \times S_{\alpha,\alpha}^{p+1,p+1}(\hat{\mathcal{M}}_{0,h}),\\ \hat{Q}_h &= \hat{Q}_h^{\mathrm{TH}}(p,\alpha) := S_{\alpha,\alpha}^{p,p}(\hat{\mathcal{M}}_{0,h})\end{aligned}$$

given $p > 1$ and $\alpha \in 0..p-1$. We then define the functional spaces $V_h = V_h^{\mathrm{TH}}$, $Q_h = Q_h^{\mathrm{TH}}$ in the physical domain Ω_0 as described in section 3.5.1. Finally, the trimmed spaces for velocity and pressure, $\tilde{V}_h$ and $\tilde{Q}_h$ respectively, are obtained as in (4.1) by restriction of the basis functions to Ω.
As it was the case for the Poisson problem in section 4.3, it is convenient to impose Dirichlet boundary conditions weakly. The discrete Nitsche formulation of the problem reads:
Find $\boldsymbol{u}_h \in \tilde{V}_h$, $p_h \in \tilde{Q}_h$ such that:

$$\begin{cases} a_h(\boldsymbol{u}_h, \boldsymbol{v}_h) + \tilde{b}(\boldsymbol{v}_h, p_h) = F_h(\boldsymbol{v}_h) & \forall \boldsymbol{v}_h \in \tilde{V}_h \\ \tilde{b}(\boldsymbol{u}_h, q_h) = G(q_h) & \forall q \in \tilde{Q}_h \end{cases} \tag{5.1}$$

where

$$a_h(\boldsymbol{u},\boldsymbol{v}) := (\mu\nabla\boldsymbol{u},\nabla\boldsymbol{v}) - \left(\mu\frac{\partial\boldsymbol{u}}{\partial\boldsymbol{n}},\boldsymbol{v}\right)_{\Gamma_D} - \left(\mu\frac{\partial\boldsymbol{v}}{\partial\boldsymbol{n}},\boldsymbol{u}\right)_{\Gamma_D} + C_{pen}\left(\frac{\mu}{H}\boldsymbol{u},\boldsymbol{v}\right)_{\Gamma_D} \quad \forall\boldsymbol{u},\boldsymbol{v}\in\tilde{V}_h; \tag{5.2}$$

$$\tilde{b}(\boldsymbol{v},q) := -(\boldsymbol{\nabla}\cdot\boldsymbol{v},q) + (q\boldsymbol{n},\boldsymbol{v})_{\Gamma_D} \qquad \forall\boldsymbol{v}\in\tilde{V}_h, q\in\tilde{Q}_h; \tag{5.3}$$

$$F_h(\boldsymbol{v}) := (\boldsymbol{f},\boldsymbol{v}) + (\boldsymbol{g_N},\boldsymbol{v})_{\Gamma_N} - \left(\mu\frac{\partial\boldsymbol{v}}{\partial\boldsymbol{n}},\boldsymbol{g_D}\right)_{\Gamma_D} + C_{pen}\left(\frac{\mu}{H}\boldsymbol{g_D},\boldsymbol{v}\right)_{\Gamma_D} \qquad \forall\boldsymbol{v}\in\tilde{V}_h; \tag{5.4}$$

$$G(q) := (q\boldsymbol{n},\boldsymbol{g_D})_{\Gamma_D} \qquad \forall q\in\tilde{Q}_h. \tag{5.5}$$

Observe that the bilinear form (5.2) and the linear functional (5.4) are formally the same as the ones used for the *untrimmed* Raviart-Thomas discretization presented in section 3.5.2 (in both cases the *tangential* component of Dirichlet boundary conditions is imposed weakly) while the bilinear form (5.3) includes a boundary term that was not present in the untrimmed Raviart-Thomas case (indeed, in the discretization at hand also the *normal* component of Dirichlet boundry conditions is imposed weakly). Moreover the new right-hand side (5.5) is introduced. As in the case of the Poisson problem in Chapter 4, the constant C_{pen} is a positive parameter that allows to have coercivity if chosen big enough. We observe that the present formulation is symmetric and consistent.
We also introduce the following mesh-dependent norms that will be used in the stability analysis:

$$\|\boldsymbol{u}\|^2_{\tilde{V}_h} := |\boldsymbol{u}|^2_{H^1(\Omega)} + \left\|H^{-\frac{1}{2}}\boldsymbol{u}\right\|^2_{L^2(\Gamma_D)} \qquad \forall\boldsymbol{u}\in\tilde{V}_h, \tag{5.6}$$

$$\|q\|^2_{\tilde{Q}_h} := \|q\|^2_{L^2(\Omega)} + \left\|H^{\frac{1}{2}}q\right\|^2_{L^2(\Gamma_D)} \qquad \forall q\in\tilde{Q}_h. \tag{5.7}$$

We write problem (5.1) in algebraic form as well. Let us for notational simplicity denote the B-spline basis of $\tilde{V}_h$ as $\{\varphi_i\}_{i=1}^{N_h^V}$ and the one of $\tilde{Q}_h$ as $\{\psi_i\}_{i=1}^{N_h^Q}$. Also define $N_h := N_h^V + N_h^Q$, the dimension of the solution space $\tilde{V}_h\times\tilde{Q}_h$. Then, the algebraic form of problem (5.1) reads:

$$\begin{pmatrix} A & \tilde{B}^T \\ \tilde{B} & \mathbf{0}\end{pmatrix}\begin{pmatrix}\boldsymbol{u}\\ \boldsymbol{p}\end{pmatrix} = \begin{pmatrix}\boldsymbol{F}\\ \boldsymbol{G}\end{pmatrix} \tag{5.8}$$

where:

$$\begin{aligned}
&A\in\mathbb{R}^{N_h^V,N_h^V} \quad A_{i,j} = a_h(\varphi_j,\varphi_i) \quad \forall i,j\in 1..N_h^V, && (5.9)\\
&\tilde{B}\in\mathbb{R}^{N_h^Q,N_h^V} \quad \tilde{B}_{i,j} = \tilde{b}(\varphi_j,\psi_i) \quad \forall i\in 1..N_h^Q, j\in 1..N_h^V, && (5.10)\\
&F\in\mathbb{R}^{N_h^V} \quad \boldsymbol{F}_i = F_h(\varphi_i) \quad \forall i\in 1..N_h^V,\\
&G\in\mathbb{R}^{N_h^Q} \quad \boldsymbol{G}_i = G(\psi_i) \quad \forall i\in 1..N_h^Q
\end{aligned}$$

and $\boldsymbol{u}\in\mathbb{R}^{N_h^V}$, $\boldsymbol{p}\in\mathbb{R}^{N_h^Q}$ are the unknown degrees of freedom of the solution. We can also express the algebraic form of the scalar products associated to the norms (5.6) and (5.7) as:

$$\begin{aligned}
&M_u\in\mathbb{R}^{N_h^V,N_h^V} \quad (M_u)_{i,j} = (\nabla\varphi_j,\nabla\varphi_i) + \left(\frac{1}{H}\varphi_j,\varphi_i\right)_{\Gamma_D} \qquad \forall i,j\in 1..N_h^V\\
&M_p\in\mathbb{R}^{N_h^Q,N_h^Q} \quad (M_p)_{i,j} = (\psi_j,\psi_i) + (H\psi_j,\psi_i)_{\Gamma_D} \qquad \forall i,j\in 1..N_h^Q. && (5.11)
\end{aligned}$$

Theorem 3 or equivalently Theorem 4 can be employed to study the well-posedness of problem (5.1).

Observe that the bilinear form (5.2) is analogous to the bilinear form (4.5) appearing in the weak formulation of the Poisson problem with weak imposition of Dirichlet boundary conditions. We stress that, while the continuity condition is also analogous, the coercivity condition on $a_h(\cdot,\cdot)$ now reads

$$a_h(\boldsymbol{u},\boldsymbol{u}) \geq \alpha \|\boldsymbol{u}\|^2_{\tilde{V}_h} \forall \boldsymbol{u} \in V_h^{\ker \tilde{B}}, \forall h > 0$$

where $V_h^{\ker \tilde{B}} := \left\{ \boldsymbol{u} \in \tilde{V}_h : \tilde{b}(\boldsymbol{u}, q) = 0 \ \forall q \in \tilde{Q}_h \right\}$. The discrete inf-sup condition in this case reads:

$$\exists \beta > 0 : \forall h > 0 \ \inf_{q \in \tilde{Q}_h} \sup_{\boldsymbol{v} \in \tilde{V}_h} \frac{\tilde{b}(\boldsymbol{v}, q)}{\|\boldsymbol{v}\|_{\tilde{V}_h(\Omega)} \|\boldsymbol{q}\|_{\tilde{Q}_h(\Omega)}} \geq \beta.$$

The stability issues observed in section 4.3 appear also in the present problem (5.1), thus the stable approximation of normal derivatives presented in section 4.4 is applied. In this case the stabilization operator reads:

$$\begin{aligned} &\boldsymbol{R}_h : \tilde{V}_h \to \left(L^2(\Gamma_D)\right)^d \\ &\boldsymbol{R}_h(\boldsymbol{v}_h)|_K := \boldsymbol{R}_K(\boldsymbol{v}_h) \qquad \forall \boldsymbol{v}_h \in \tilde{V}_h, K \in \mathcal{G}_h, \end{aligned}$$

where:

- if $K \in \mathcal{G}_h^g$

$$\boldsymbol{R}_K(\boldsymbol{v}_h) := \frac{\partial(\boldsymbol{v}_h|_K)}{\partial \boldsymbol{n}} \qquad \boldsymbol{v}_h \in \tilde{V}_h;$$

- if $K = \boldsymbol{F}(Q) \in \mathcal{G}_h^b$, denoting $K' = \boldsymbol{F}(Q')$ a good neighbour of K

$$\boldsymbol{R}_K(\boldsymbol{v}_h) := \frac{\partial}{\partial \boldsymbol{n}} \left(\mathcal{E}(\hat{\boldsymbol{v}_h}|_{Q'}) \circ \boldsymbol{F}^{-1} \right) \qquad \boldsymbol{v}_h \in \tilde{V}_h, \tag{5.12}$$

  where $\mathcal{E} : (\mathbb{P}_p(Q'))^d \to (\mathbb{P}_p(Q \cup Q'))^d$ is the vectorial polynomial extension operator.

The stabilized version of the problem reads:

$$\begin{cases} a_h^S(\boldsymbol{u}_h, \boldsymbol{v}_h) + \tilde{b}(\boldsymbol{v}_h, p_h) = F_h^S(\boldsymbol{v}_h) & \forall \boldsymbol{v}_h \in \tilde{V}_h \\ \tilde{b}(\boldsymbol{u}_h, q_h) = G(q_h) & \forall q \in \tilde{Q}_h \end{cases} \tag{5.13}$$

where now

$$a_h^S(\boldsymbol{u},\boldsymbol{v}) := (\mu \nabla \boldsymbol{u}, \nabla \boldsymbol{v}) - (\mu \boldsymbol{R}(\boldsymbol{u}), \boldsymbol{v})_{\Gamma_D} - (\mu \boldsymbol{R}(\boldsymbol{v}), \boldsymbol{u})_{\Gamma_D} + C_{pen} \left(\frac{\mu}{H} \boldsymbol{u}, \boldsymbol{v} \right)_{K \cap \Gamma_D} \quad \forall \boldsymbol{u}, \boldsymbol{v} \in \tilde{V}_h; \tag{5.14}$$

$$F_h^S(\boldsymbol{v}) := (\boldsymbol{f}, \boldsymbol{v}) + (\boldsymbol{g_N}, \boldsymbol{v})_{\Gamma_N} - (\mu \boldsymbol{R}(\boldsymbol{v}), \boldsymbol{g_D})_{\Gamma_D} + C_{pen} \left(\frac{\mu}{H} \boldsymbol{g_D}, \boldsymbol{v} \right)_{K \cap \Gamma_D} \qquad \forall \boldsymbol{v} \in \tilde{V}_h. \tag{5.15}$$

5.2 Numerical estimation of stability constants

The global stability of problem (5.1) or of the stabilized problem (5.13) can be assessed by estimating the global coercivity and continuity constants, here denoted α and C respectively, as suggested in Theorem 4 and the following remark. This can be achieved solving a generalized eigenvalue problem. For example, for problem (5.1):

$$\min \{\lambda_i\}_{i=1}^{N_h} \geq \alpha, \qquad \max \{\lambda_i\}_{i=1}^{N_h} \leq C$$

where $\{\lambda_i\}_{i=1}^{N_h}$ are the eigenvalues of the generalized eigenvalue problem:
Find $\boldsymbol{x} \in \mathbb{R}^{N_h} \setminus \{\mathbf{0}\}$, $\lambda \in \mathbb{R}$:

$$D\boldsymbol{x} = \lambda M\boldsymbol{x} \tag{5.16}$$

where

$$D := \begin{pmatrix} A & \tilde{B}^T \\ \tilde{B} & \mathbf{0} \end{pmatrix} \in \mathbb{R}^{N_h, N_h}, \qquad M := \begin{pmatrix} M_u & \mathbf{0} \\ \mathbf{0} & M_p \end{pmatrix} \in \mathbb{R}^{N_h, N_h}.$$

The Taylor-Hood elements will be considered stable with respect to h if the estimates of the global coercivicty and continuity constants, α and C, and the inf-sup constant β (in the sense of Theorem 3) converge to finite values as h tends to zero. Moreover, they will be considered stable with respect to the trimming if α, C and β do not depend on the position of the trimming curve T. We remark that the value of the minimum eigenvalue depends on the parameter C_{pen} (if C_{pen} is increased, also the minimum eigenvalue increases). Therefore, obtaining a *negative* estimate of the global coercivity constant with e.g. $C_{pen} = 1$ does not imply that the scheme is unstable but only that a bigger C_{pen} is needed. The inf-sup stability in the sense of Theorem 3 is also studied because it is equivalent to coercivity and continuity of the global bilinear form if the "coercivity on the kernel" condition (3.10) holds. We report the method used in [1] to estimate the inf-sup constant β:

$$\alpha_h = \min \{\sqrt{\gamma_i}\}_{i=1}^{N_h} \geq \beta,$$

where $\{\gamma_i\}_{i=1}^{N_h^Q}$ are the eigenvalues of the generalized eigenvalue problem:
Find $\boldsymbol{x} \in \mathbb{R}^{N_h^Q} \setminus \{\mathbf{0}\}$, $\gamma \in \mathbb{R}$:

$$\tilde{B}A^{-1}\tilde{B}^T\boldsymbol{x} = \gamma M_p\boldsymbol{x}.$$

5.3 Numerical experiments without stabilization

In the following tests the effect of the position of the trimming curve with respect to the knotlines is studied. In particular, we look at the convergence with respect to mesh refinement of the error for different *trimming-to-element ratios*, i.e. fixing a constant ratio ρ between the distance of a straight trimming line from a knot-line and the mesh-size. Moreover, the stability tests presented in the previous sections are performed.
We start by introducing the domain that will be used for the numerical experiments using the notation detailed in section 4.2. On the parametric domain $\hat{\Omega}$ a number of elements per side n is fixed and a uniform tensor product mesh $\hat{\mathcal{M}}_h$ is defined, where $h = \frac{1}{n}$ is the length of the side of each element. Fixed a trimming-to-element ratio ρ, a trimming size $\delta = \rho h$ is defined. The parametric (trimmed) domain is then defined as $\hat{\Omega} = (0,1) \times (0, 1-h+\delta)$ and the trimming curve is $T = \{(x, 1-h+\delta) : x \in (0,1)\}$. The parametric-to-physical mapping $\boldsymbol{F}(x,y) = \left(x, \frac{y}{1-h+\delta}\right)$ is chosen in order to obtain $\Omega = (0,1) \times (0,1)$. This example is chosen because of the presence of a sliver cut (in the sense already mentioned in section 4.3). Therefore, when weak Dirichlet boundary conditions are imposed on the trimmed side, the stability issues presented above should appear.
Errors are computed with respect to the following manufactured solution:

$$\boldsymbol{u} : \Omega \subset \mathbb{R}^2 \to \mathbb{R}^2 \qquad \boldsymbol{u}(x,y) := \begin{pmatrix} -\frac{\sin(\pi x)}{\pi^2} \cdot \cos(y) \\ \frac{\cos(\pi x)}{\pi} \cdot \sin(y) \end{pmatrix}$$

$$p : \Omega \subset \mathbb{R}^2 \to \mathbb{R} \qquad p(x,y) := -\frac{\cos(\pi x)\cos(y)}{\pi}.$$

Observe that $\boldsymbol{u}$ is divergence-free.
Numerical experiments are presented in the subsequent sections using either Neumann

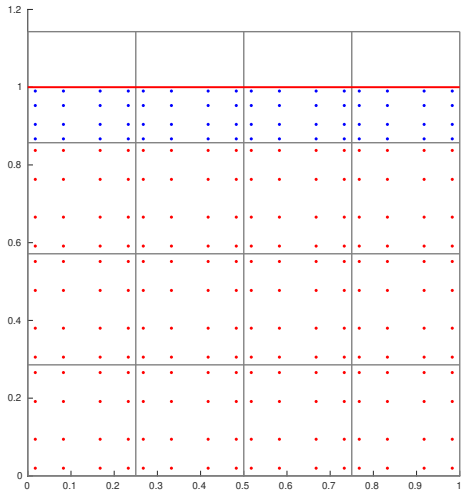

Figure 5.1: Example of trimmed domain with $h = 0.25$ (4 elements per side) and $\rho = \frac{1}{2}$. The grey lines delimit the untrimmed mesh $\mathcal{M}_{0,h}$ (that, in this case, also corresponds to the mesh $\mathcal{M}_h$), the red line is the trimming curve, red dots indicate quadrature points on untrimmed elements, the blue ones the quadrature points on the cut-elements.

or Dirichlet boundary conditions on the side $\{(x, 1) : x \in (0, 1)\}$ of the physical domain Ω (the side that corresponds to the trimming curve T). For all the following numerical experiments Dirichlet boundary conditions are imposed in the classical way on the side $\{(x, 0) : x \in (0, 1)\}$ and homogeneous Neumann boundary conditions are imposed on the sides $\{(0, y) : y \in (0, 1)\}$ and $\{(1, y) : y \in (0, 1)\}$.
We choose degree $p = 3$ splines with regularity $\alpha = 2$. Integration of basis functions on each element is performed using a Gaussian quadrature rule with $p + 1$ Gaussian quadrature points per parametric direction. To approximate integrals on the boundary, $p + 1$ quadrature nodes are used. In figure 5.1 an example of trimmed domain and quadrature points on each element is shown. When Dirichlet boundary conditions are enforced weakly, the stabilization constant $C_{pen} = 10p$ is chosen. Stability tests are also performed as explained in the previous section. The penalization constant for the weak imposition of Dirichlet boundary conditions is put to $C_{pen} = 1$.
For both numerical verifications of the convergence rate and stability of the problems we test trimming-to-element ratios $\rho \in \{10^{-1}, 10^{-4}, 10^{-7}, 10^{-10}\}$ and mesh-sizes $h \in \{2^{-1}, 2^{-2}, 2^{-3}, 2^{-4}, 2^{-5}, 2^{-6}\}$.
All numerical tests were carried out using the Matlab library `GeoPDEs` [19]. When solving linear systems, the simple diagonal preconditioner described in chapter 8 is applied.

5.3.1 Experiments with Neumann boundary condition

We impose inhomogeneous Neumann boundary conditions on the side $\{(x, 1) : x \in (0, 1)\}$ with datum:

$$\boldsymbol{g} : \{(x, 1) : x \in (0, 1)\} \to \mathbb{R}^2 \qquad \boldsymbol{g}(x) := \begin{pmatrix} \frac{\sin(1)\sin(\pi x)}{\pi^2} \\ 2\frac{\cos(1)\cos(\pi x)}{\pi} \end{pmatrix} \tag{5.17}$$

A visual comparison of the exact and numerical solution computed with $h = 2^{-3}$ and $\rho = 0.5$ is shown in figure 5.2 for velocity and pressure. Error distributions and the divergence of the numerical solution are shown in figure 5.3.

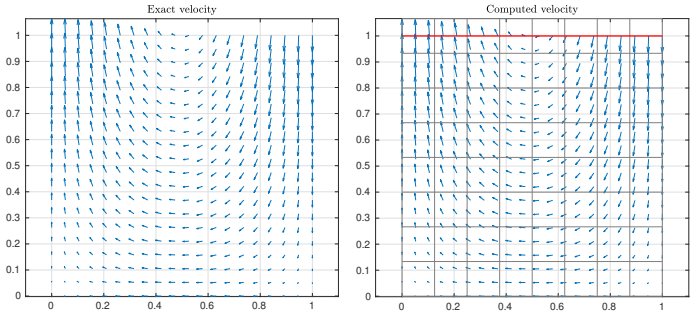

(a) Comparison of exact and numerical velocity

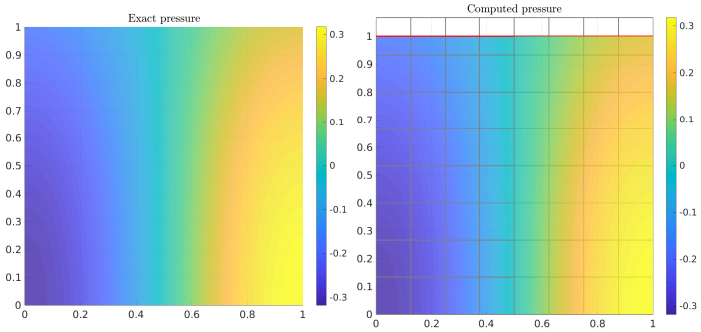

(b) Comparison of exact and numerical pressure

Figure 5.2: Comparison of exact solution and numerical velocity (a) and pressure (b) obtained with Taylor-Hood elements on trimmed domain.

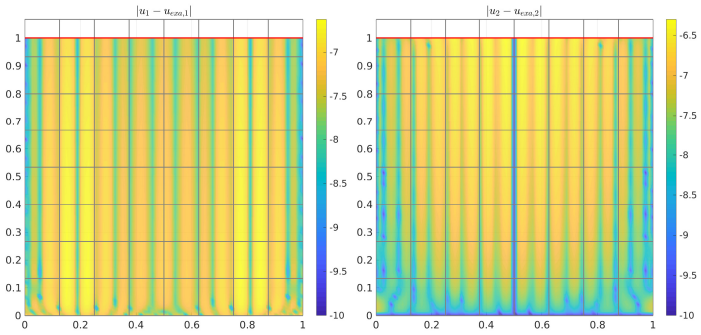

(a) Error distribution on the velocity, componentwise.

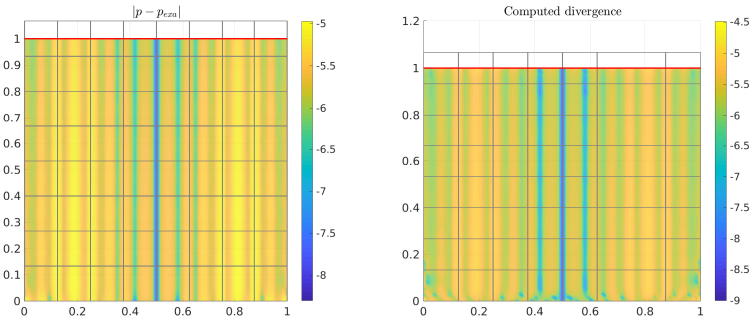

(b) Error distribution on the pressure.

(c) Divergence of numerical solution

Figure 5.3: Error distribution of the numerical velocity (a) and pressure (b) obtained with Taylor-Hood elements on a trimmed domain. Divergence of the numerical solution (c). all quantities as plotted in log-scale.

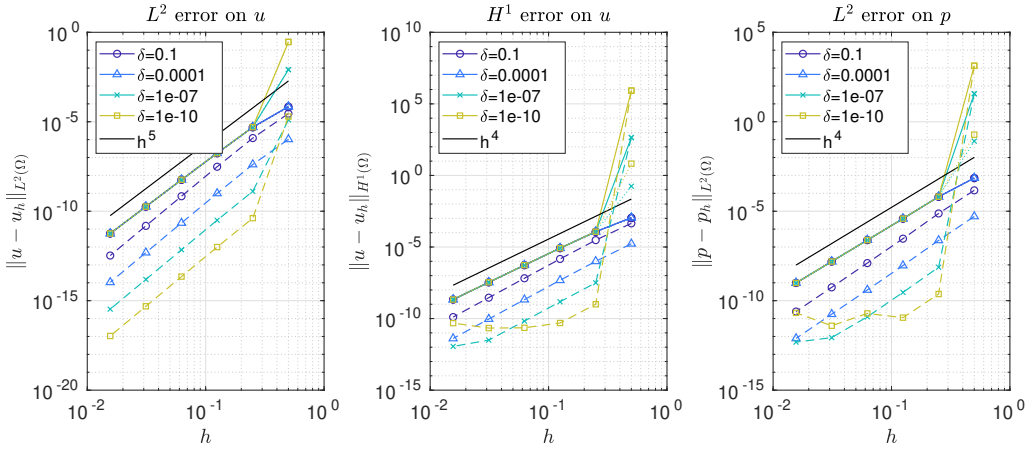

Figure 5.4: Taylor-Hood with Neumann B.C.: errors (L^2 and H^1 norms for the velocity, L^2 norm for the pressure) for decreasing mesh sizes h and values of the trimming-to-element ratio ρ. For each value of ρ, the total error (continuous line) is split in the error on untrimmed (dashed fine line) and cut-elements (dashed line).

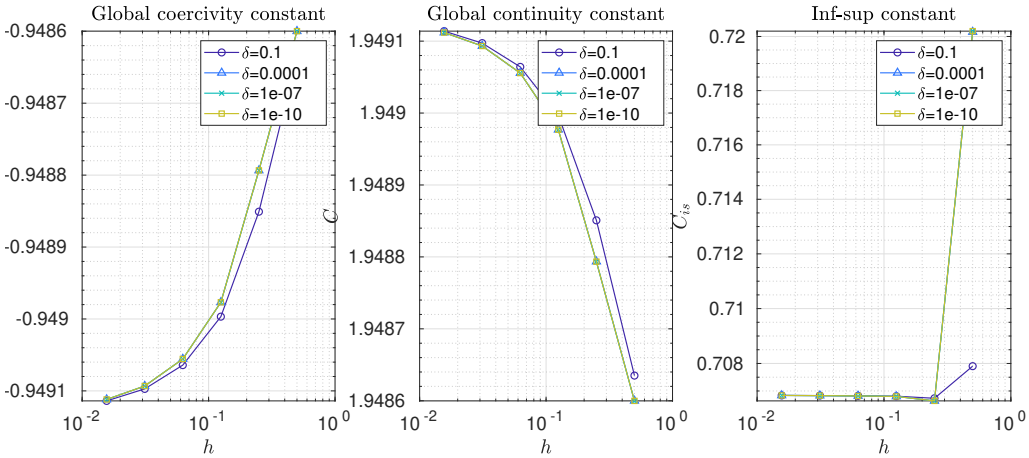

Figure 5.5: Taylor-Hood with Neumann B.C.: numerical estimates of global coercivity, global continuity and inf-sup constants for decreasing mesh sizes h and values of the trimming-to-element ratio ρ.

In figure 5.4 the L^2, H^1 error for velocity and L^2 for pressure are plotted for the values of ρ and h listed above. Moreover, the total error (continuous line) is split in the error computed on untrimmed (dashed fine line) and cut-elements (dashed line). In all cases the total error follows the expected convergence rate for Taylor-Hood elements. The error on the untrimmed elements dominates the error on trimmed elements. Observe that the errors on cut-elements as a function of h are roughly parallel for different values of ρ and their offset is proportional to $\sqrt{\rho}$. For both H^1 error for velocity and L^2 error for pressure, the error on cut-elements corresponding to $\rho \in \{10^{-7}, 10^{-10}\}$ stops decreasing for the smallest values of h. Moreover, for $\rho = 10^{-10}$ the errors stop decreasing when they reach a higher value than in the case $\rho = 10^{-7}$. This effect is attributed to round-off errors in the assembly of the Neumann boundary condition that become evident when ρ is small. In particular, some of the operations affected by these errors are the placement of quadrature points and in the evaluations of basis functions.

The stability of the method is assessed by estimating the global coercivity and continuity constants as explained in the section 5.2. In figure 5.5 these quantities are plotted for the same values of ρ and h that were used for the convergence test. In can be observed that both estimates converge as h decreases and the limit is independent of the value of

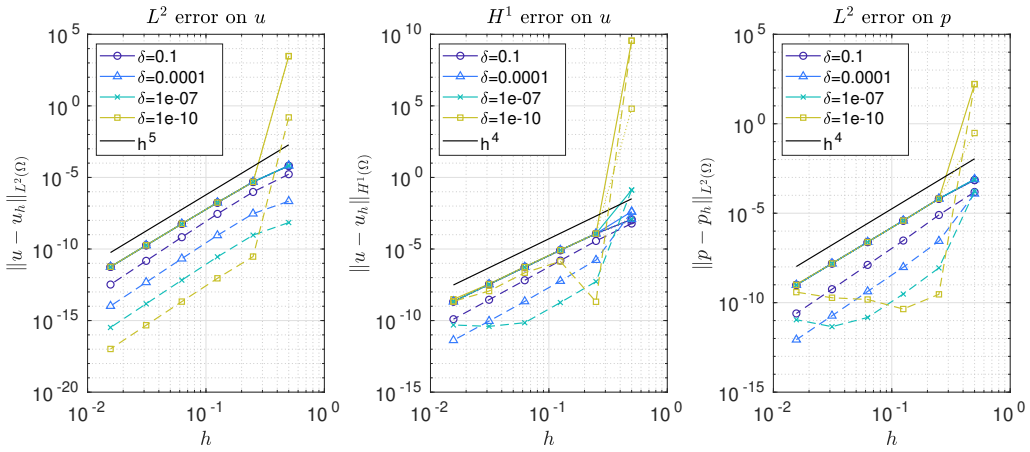

Figure 5.6: Taylor-Hood with weak Dirichlet B.C.: errors (L^2 and H^1 norms for the velocity, L^2 norm for the pressure) for decreasing mesh sizes h and values of the trimming-to-element ratio ρ. For each value of ρ, the total error (continuous line) is split in the error on untrimmed (dashed fine line) and cut-elements (dashed line).

the trimming-to-element ratio ρ. Observe that the fact that the estimate of the coercivity constant converges to a negative value does not mean that the scheme is unstable. As mentioned above, the value of the Nitsche parameter is set to $C_{pen} = 1$ for stability tests but leads to a positive coercivity constant if sufficiently big (e.g. $C_{pen} = 10(d+1)$ used in the convergence tests). The estimate of the inf-sup constant, shown in the last sub-plot of figure 5.5, shows that (for the problem at hand) the Taylor-Hood elements are inf-sup stable independently of the ratio ρ.

5.3.2 Experiments with (weak) Dirichlet boundary condition

The same setting as in the previous section is employed, except that the Neumann condition on $\{(x,1) : x \in (0,1)\}$ is substituted by a (inhomogeneous) Dirichlet condition enforced weakly as described in section 5.1.

As in the previous section, in figure 5.6 the error for velocity and pressure is show in several norms. Similar problems as those shown in the case of Neumann boundary conditions can be observed. In particular, for the smallest values of ρ the error on cut-elements does not decrease as expected when h decreases, instead it may have a sharp growth (H^1 error of the velocity for $\rho = 10^{-10}$) or increase steadily (L^2 error of the pressure for $\rho = 10^{-7}, 10^{-10}$). In figure 5.7 we also plot the convergence test in the mesh-dependent norms (5.6) for velocity and (5.7) for pressure, that are the natural norms for the analysis of the method. For the smallest values of ρ the error on the pressure is dominated by the error on the cut elements and the trimmed boundary and increases slightly as h decreases. This behaviour is again attributed to round-off errors.

The results of the stability tests are shown in figure 5.8. As predicted in section 5.2, the global coercivity and continuity constants are highly affected by the valued of the trimming-to-element ratio ρ. In facts, as ρ tends to 0, the global coercivity (resp. continuity) constant decrease (resp. increases) indefinitely, showing that the numerical scheme is not uniformly stable with respect to ρ. By contrast, the inf-sup condition seems to be satisfied uniformly in ρ with a slightly higher inf-sup constant for the largest ratio $\rho = 10^{-1}$.

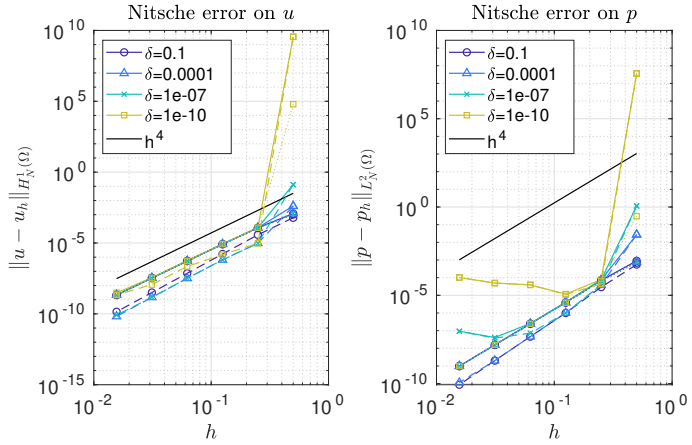

Figure 5.7: Taylor-Hood with weak Dirichlet B.C.: errors (norm (5.6) for the velocity, (5.7) for the pressure) for decreasing mesh sizes h and values of the trimming-to-element ratio ρ. For each value of ρ, the total error (continuous line) is split in the error on untrimmed (dashed fine line) and cut-elements (dashed line).

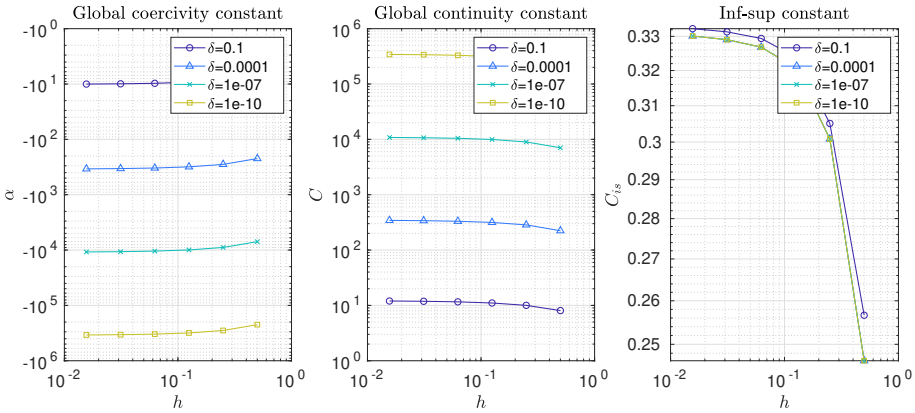

Figure 5.8: Taylor-Hood with weak Dirichlet B.C.: numerical estimates of global coercivity, global continuity and inf-sup constants for decreasing mesh sizes h and values of the trimming-to-element ratio ρ.

5.4 Numerical experiments with stabilization

In light of the results show in the previous section, in particular the lack of stability of the scheme, we now test the stabilized scheme (5.13). The stabilization is applied on every element for all values of ρ, in other words every cut element is considered a bad cut element (equivalently, the parameter ϑ in definition 1 is chosen as $\vartheta = 1$). The convergence test plotted in figure 5.9 shows the beneficial effect of the stabilization. Unlike the results shown in figure 5.9, the L^2 error for the pressure has the expected behaviour and the H^1 error on the velocity, although still suffering from round-off errors, is lower compared to the non-stabilized case.
These observations are confirmed by the convergence test in the mesh-dependent norms shows in figure 5.10
The stability tests for the stabilized scheme are show in figure 5.11. Global coercivity and continuity constants converge to real numbers as h decreases and unlike the non-stabilized case these values are only mildly dependent on the value of ρ and becomes independent as $\rho \to 0$. The inf-sup constant has the same behaviour as the previous case, showing that the stabilization does not affect negatively the inf-sup stability of the Taylor-Hood elements.

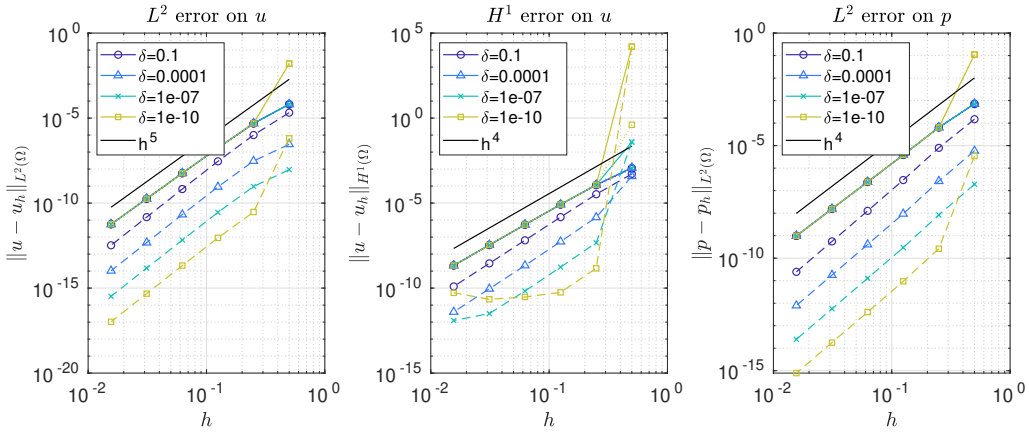

Figure 5.9: Stabilized Taylor-Hood with weak Dirichlet B.C.: errors (L^2 and H^1 norms for the velocity, L^2 norm for the pressure) for decreasing mesh sizes h and values of the trimming-to-element ratio ρ. For each value of ρ, the total error (continuous line) is split in the error on untrimmed (dashed fine line) and cut-elements (dashed line).

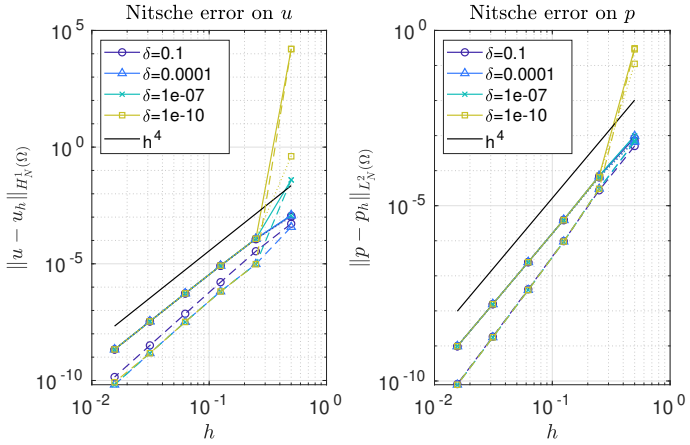

Figure 5.10: Stabilized Taylor-Hood with weak Dirichlet B.C.: errors (norm (5.6) for the velocity, (5.7) for the pressure) for decreasing mesh sizes h and values of the trimming-to-element ratio ρ. For each value of ρ, the total error (continuous line) is split in the error on untrimmed (dashed fine line) and cut-elements (dashed line).

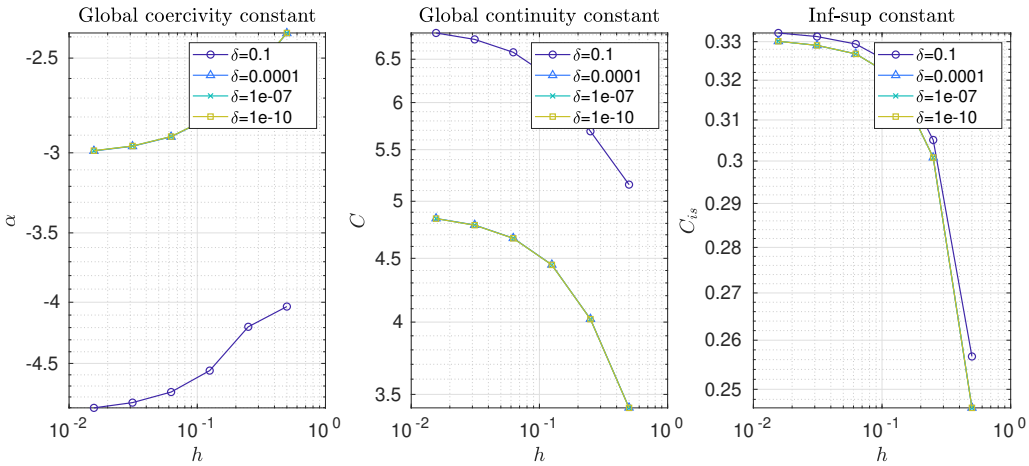

Figure 5.11: Stabilized Taylor-Hood with weak Dirichlet B.C.:numerical estimates of global coercivity, global continuity and inf-sup constants for decreasing mesh sizes h and values of the trimming-to-element ratio ρ.

Chapter 6

Trimmed Raviart-Thomas elements

In this chapter a numerical scheme based on the Raviart-Thomas isogeometric elements is presented following the same structure of the previous chapter. In the first section we define the trimmed Raviart-Thomas space, then state the formulation of the problem with weak imposition of essential boundary conditions with and without stabilization. In the second section we give some details about the numerical estimation of the stability constant from theorems 3 and 4. In the third section, we apply the non-stabilized scheme to problems with Neumann and weak Dirichlet boundary conditions in order to assess its convergence and stability properties. Finally, in the fourth section the same stability and convergence tests are repeated for the stabilized scheme.

6.1 Problem formulation

Let us consider again the Stokes problem (3.1). As in section 4.2, we suppose an untrimmed domain $\Omega_0 = \boldsymbol{F}(\hat{\Omega}_0)$ is given with $\hat{\mathcal{M}}_{0,h}$, $\mathcal{M}_{0,h}$ parametric and physical Bèzier meshes respectively. The domain Ω is obtained by trimming Ω_0, the trimming curve is T. $\hat{\Omega} = \boldsymbol{F}^{-1}(\Omega)$ denotes the parametric domain, $\hat{\mathcal{M}}_h$ and $\mathcal{M}_h$ the parametric and physical Bézier mesh respectively, $\mathcal{G}_h$ the cut-elements.
We consider the Raviart-Thomas isogeometric elements on Ω_0 with Bézier mesh $\mathcal{M}_{0,h}$ and recall their definition first given in section 3.5.2:

$$\begin{aligned}\hat{V}_h = \hat{V}_h^{\mathrm{RT}}(p,\alpha) &:= S^{p+1,p}_{\alpha+1,\alpha}(\hat{\mathcal{M}}_{0,h}) \times S^{p,p+1}_{\alpha,\alpha+1}(\hat{\mathcal{M}}_{0,h}),\\ \hat{Q}_h = \hat{Q}_h^{\mathrm{RT}}(p,\alpha) &:= S^{p,p}_{\alpha,\alpha}(\hat{\mathcal{M}}_{0,h})\end{aligned}$$

for given degree p and regularity $\alpha \in 0..p-1$. The functional spaces $V_h = V_h^{\mathrm{RT}}$ and $Q_h = Q_h^{\mathrm{RT}}$ on the physical domain Ω_0 are defined as in section 3.5.2 through the divergence and integral-reserving maps (3.17), (3.18). Finally, the trimmed spaces for velocity and pressure, $\tilde{V}_h$ and $\tilde{Q}_h$ respectively, are obtained as in (4.1) by restriction of the basis functions to Ω.
As for the Taylor-Hood elements presented in the previous section, we impose Dirichlet boundary conditions weakly. The problem reads:
Find $\boldsymbol{u}_h \in \tilde{V}_h$, $p_h \in \tilde{Q}_h$ such that:

$$\begin{cases} a_h(\boldsymbol{u}_h, \boldsymbol{v}_h) + \tilde{b}(\boldsymbol{v}_h, p_h) = F_h(\boldsymbol{v}_h) \qquad \forall \boldsymbol{v}_h \in \tilde{V}_h \\ b(\boldsymbol{u}_h, q_h) = 0 \qquad \forall q \in \tilde{Q}_h \end{cases} \tag{6.1}$$

where $a_h(\cdot,\cdot)$, $\tilde{b}(\cdot,\cdot)$ and F_h are defined as in (5.2)-(5.4) and $b(\cdot,\cdot)$ as in (3.3). To write the problem in algebraic form we denote the B-spline basis of $\tilde{V}_h$ as $\{\varphi_i\}_{i=1}^{N_h^V}$ and the one

of $\tilde{Q}_h$ as $\{\psi_i\}_{i=1}^{N_h^Q}$ and define $N_h := N_h^V + N_h^Q$. Then, the algebraic form of (6.1) reads:

$$\begin{pmatrix} A & \tilde{B}^T \\ B & \mathbf{0} \end{pmatrix} \begin{pmatrix} \boldsymbol{u} \\ \boldsymbol{p} \end{pmatrix} = \begin{pmatrix} \boldsymbol{F} \\ \mathbf{0} \end{pmatrix} \tag{6.2}$$

where $A, \tilde{B}$ are defined as in (5.9), (5.10) and

$$B \in \mathbb{R}^{N_h^Q, N_h^V} \quad \tilde{B}_{i,j} = b(\varphi_j, \psi_i) \quad \forall i \in 1..N_h^Q, j \in 1..N_h^V.$$

Observe that the present problem formulation is consistent but not symmetric. This problem differs from (5.1) in the second row. This choice is made to preserve the divergence-conforming property of Raviart-Thomas isogeometric elements.
Because of the lack of symmetry of problem (6.1), Theorem 3 cannot be directly applied to study its well-posedness. However, Theorem 4 can be applied, as problem (6.1) can be recasted in the form:
Find $u_h \in \mathcal{U}_h$ such that

$$\mathcal{A}(u_h, v_h) = \mathcal{F}(v_h) \qquad \forall v_h \in \mathcal{V}_h$$

where

$$\begin{aligned} \mathcal{U}_h = \mathcal{V}_h &:= \tilde{V}_h \times \tilde{Q}_h, \\ \mathcal{A}(u_h, v_h) = \mathcal{A}((\boldsymbol{u}_h, p_h), (\boldsymbol{v}_h, q_h)) &:= a(\boldsymbol{u}_h, \boldsymbol{v}_h) + \tilde{b}(\boldsymbol{v}_h, p_h) + b(\boldsymbol{u}_h, q_h) \\ \forall u_h = (\boldsymbol{u}_h, p_h) \in \mathcal{U}_h, v_h = (\boldsymbol{v}_h, q_h) &\in \mathcal{V}_h, \\ \mathcal{F}(v_h) = \mathcal{F}((\boldsymbol{v}_h, q_h)) &:= F(\boldsymbol{v}_h) \qquad \forall v_h = (\boldsymbol{v}_h, q_h) \in \mathcal{V}_h. \end{aligned}$$

The norm used in the analysis is:

$$\|u_h\|_{\mathcal{U}_h} := \sqrt{\|\boldsymbol{u}_h\|_{\tilde{V}_h}^2 + \|p_h\|_{\tilde{Q}_h}^2} \qquad \forall u_h = (\boldsymbol{u}_h, p_h) \in \mathcal{U}_h.$$

where $\|\cdot\|_{\tilde{V}_h}, \|\cdot\|_{\tilde{Q}_h}$ are defined in (5.6), (5.7).
In this case, the stabilization operator defined in the previous section takes a slightly different form. In facts, (5.12) must be substituted by:

$$\boldsymbol{R}_K(\boldsymbol{v}_h) := \frac{\partial}{\partial \boldsymbol{n}} \iota_V \left(\mathcal{E}(\hat{\boldsymbol{v}}_h|_{Q'}) \right) \qquad \boldsymbol{v}_h \in \tilde{V}_h,$$

where ι_V is the div-preserving transformation (3.17).
The stabilized version of the problem reads:

$$\begin{cases} a_h^S(\boldsymbol{u}_h, \boldsymbol{v}_h) + \tilde{b}(\boldsymbol{v}_h, p_h) = F_h^S(\boldsymbol{v}_h) \qquad \forall \boldsymbol{v}_h \in \tilde{V}_h \\ b(\boldsymbol{u}_h, q_h) = 0 \qquad \forall q \in \tilde{Q}_h \end{cases} \tag{6.3}$$

where $a_h^S(\cdot,\cdot)$ and $F_h^S(\cdot)$ are defined as for Taylor-Hood elements in (5.14) and (5.15) respectively.

6.2 Numerical estimation of stability constants

As for the case of the trimmed Taylor-Hood elements, the continuity and coercivity constants can be estimated solving a generalized eigenvalue problem in the form (5.16), where now:

$$D := \begin{pmatrix} A & \tilde{B}^T \\ B & \mathbf{0} \end{pmatrix} \in \mathbb{R}^{N_h, N_h}, \tag{6.4}$$

the stiffness matrix of the problem at hand. We stress that, being the problem non-symmetric, eigenvalues may have a non-zero imaginary part. Therefore, the eigenvalues with maximum and minimum real part will be approximated and used as estimates.

6.3 Numerical experiments without stabilization

Analogously to what was done for Taylor-Hood elements in the previous chapter, the convergence and stability of problem (6.1) with Raviart-Thomas elements is studied. The square domain described in section 5.3 is used. In particular, the trimming-to-element ratio ρ is varied in order to asses the effect of the distance of the trimming line from the closes knots-line on convergence and stability.
The same manufactured solution (5.3) is used, with either Dirichlet or Neumann boundary conditions on the trimmed side. The spline space for pressures is again chosen to have degree $p = 3$ and regularity $\alpha = 2$. The Nitsche parameter is $C_{pen} = 10(d + 1)$ for convergence tests, $C_{pen} = 1$ for stability tests. Finally, the same trimming-to-element ratios $\rho \in \{10^{-1}, 10^{-4}, 10^{-7}, 10^{-10}\}$ and mesh-sizes $h \in \{2^{-1}, 2^{-2}, 2^{-3}, 2^{-4}, 2^{-5}, 2^{-6}\}$ are tested. When solving linear systems, the simple diagonal preconditioner described in chapter 8 is applied.

6.3.1 Experiments with Neumann boundary conditions

A Neumann boundary condition with datum (5.17) is imposed on the trimmed side $\{(x, 1), x \in (0, 1)\}$. A visual comparison of the exact and numerical solution computed with $h = 2^{-3}$ and $\rho = 0.5$ in figure 6.1 for velocity and pressure respectively. Error distributions and the divergence of the numerical solution are shown in figure 6.2. We stress that, as it can be seen in the last sub-plot of figure 6.2, the divergence of the numerical solution is zero up to machine precision.

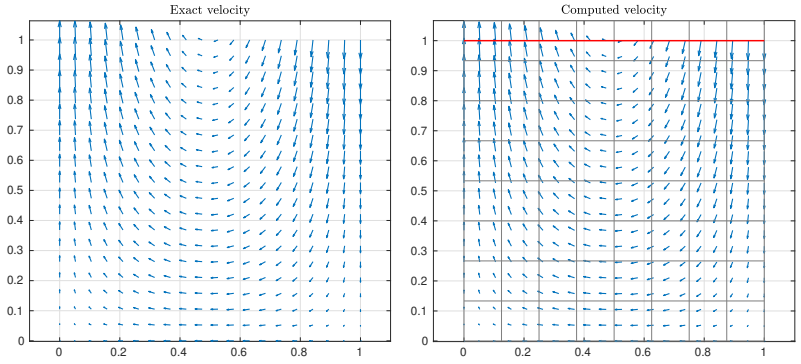

(a) Comparison of exact and numerical velocity

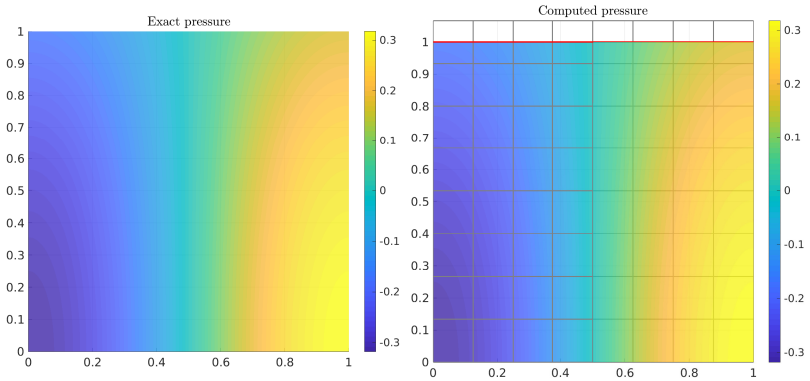

(b) Comparison of exact and numerical pressure

Figure 6.1: Comparison of exact solution and numerical velocity (a) and pressure (b) obtained with Raviart-Thomas elements on trimmed domain.

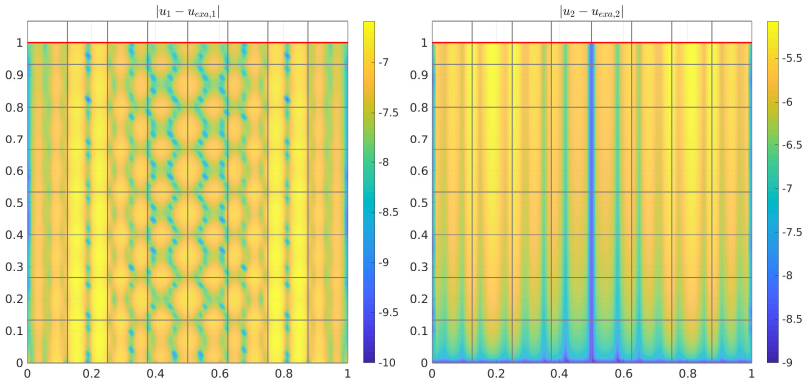

(a) Error distribution on the velocity, componentwise.

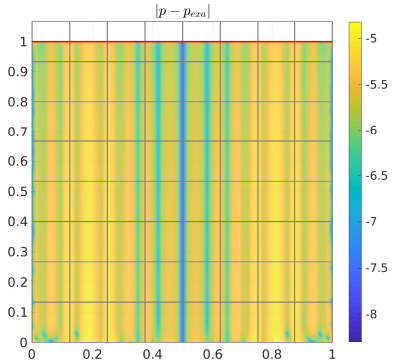

(b) Error distribution on the pressure.

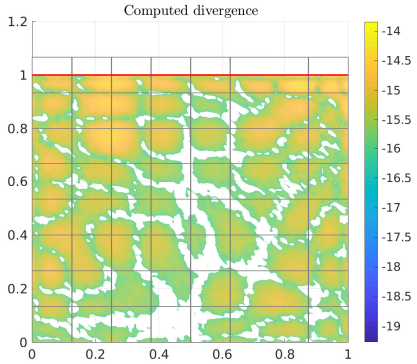

(c) Divergence of numerical solution

Figure 6.2: Error distribution of the numerical velocity (a) and pressure (b) obtained with Raviart-Thomas elements on a trimmed domain. Both quantities as plotted in log-scale. Divergence of the numerical solution (c) in log-scale.

In figure 6.3 the L^2, H^1 error for velocity and L^2 for pressure are plotted for the values of ρ and h listed above. Moreover, the total error (continuous line) is split in the error computed on untrimmed (dashed fine line) and cut-elements (dashed line). In all cases the total error follows the expected convergence rate for Raviart-Thomas elements. The error on the untrimmed elements dominates the error on trimmed elements. Observe that the errors on cut-elements as a function of h are roughly parallel for different values of ρ and their offset is proportional to $\sqrt{\rho}$. For both H^1 error for velocity and L^2 error for pressure, the error on cut-elements corresponding to $\rho \in \{10^{-7}, 10^{-10}\}$ decreases sub-optimally for the smallest values of h. Moreover, for $\rho = 10^{-10}$ the errors stop decreasing when they reach a higher value than in the case $\rho = 10^{-7}$. As in the case of Taylor-Hood elements, this effect is attributed to round-off errors in the assembly of the Neumann boundary condition that become evident when ρ is small.

The stability of the method is assessed by estimating the global coercivity and continuity constants as explained in the section 6.2. In figure 6.4 these quantities are plotted for the same values of ρ and h that were used for the convergence test. In can be observed that both estimates converge as h decreases and the limit is independent of the value of the trimming-to-element ratio ρ. The estimate of the inf-sup constant, shown in the last sub-plot of figure 6.4, seems not to converge as quickly as h is decreased. However, it can be seen that its variation between subsequent mesh-sizes h is decreasing.

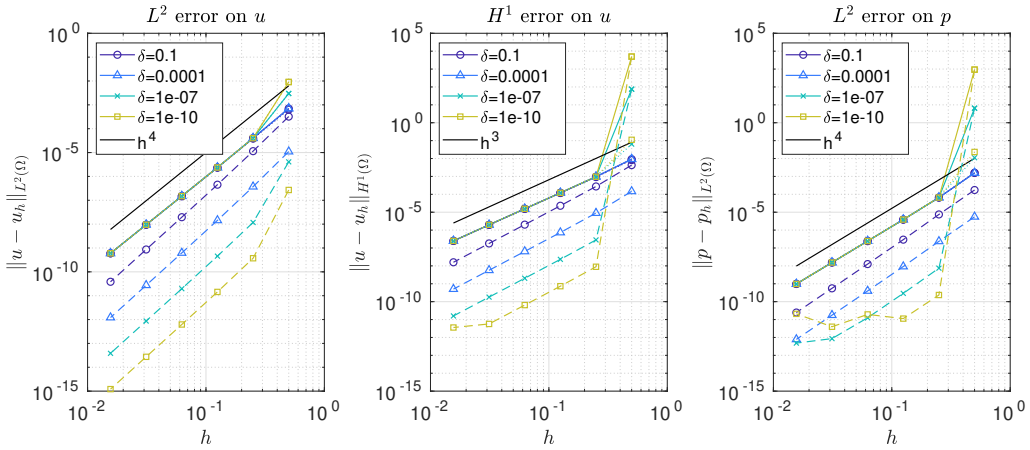

Figure 6.3: Raviart-Thomas with Neumann B.C.: errors (L^2 and H^1 norms for the velocity, L^2 norm for the pressure) for decreasing mesh sizes h and values of the trimming-to-element ratio ρ. For each value of ρ, the total error (continuous line) is split in the error on untrimmed (dashed fine line) and cut-elements (dashed line).

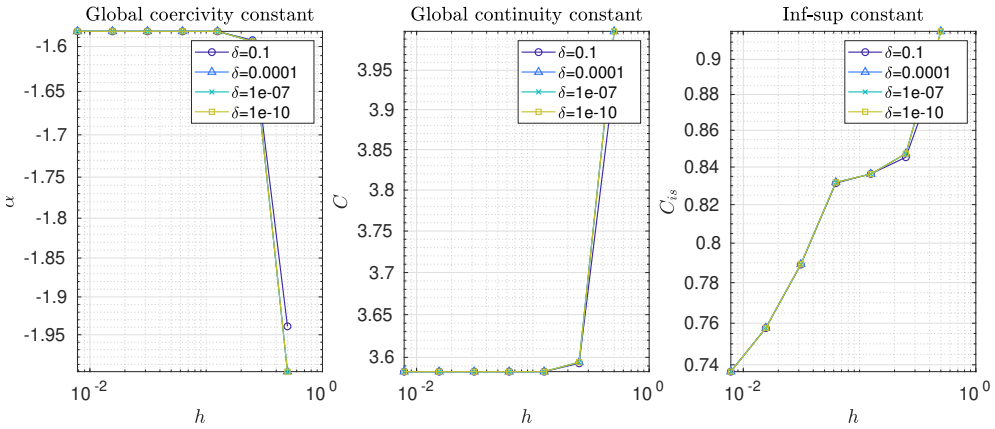

Figure 6.4: Raviart-Thomas with Neumann B.C.: numerical estimates of global coercivity, global continuity and inf-sup constants for decreasing mesh sizes h and values of the trimming-to-element ratio ρ.

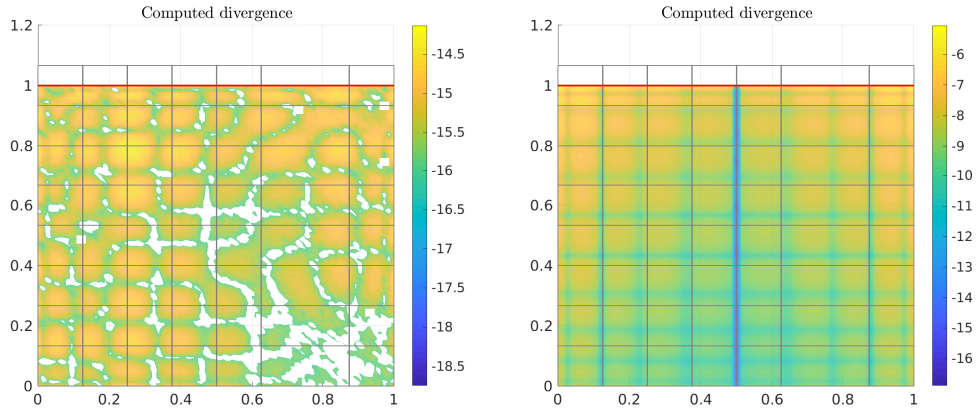

Figure 6.5: Raviart-Thomas with weak Dirichlet B.C.: comparison of divergence of numerical solution obtained with the non-symmetric formulation (6.1)(a) and the symmetric one (5.1) (b) in log-scale.

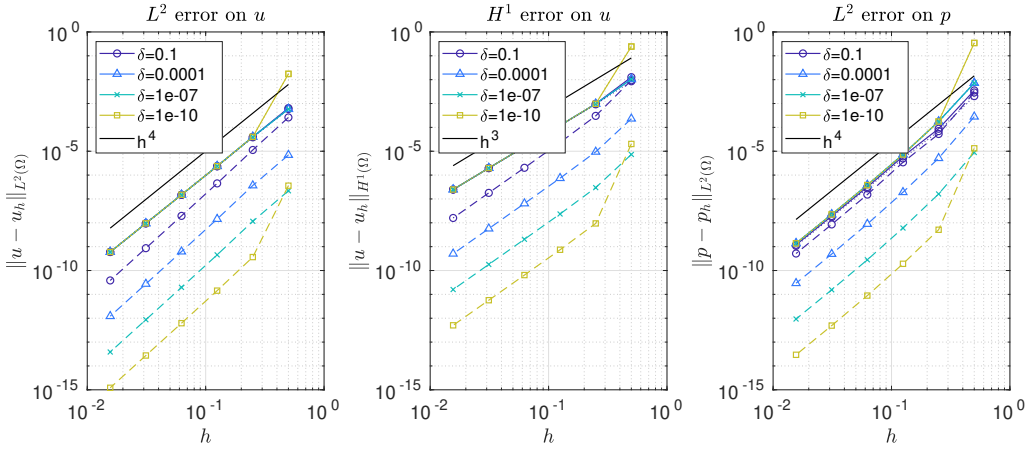

Figure 6.6: Raviart-Thomas with weak Dirichlet B.C.: errors (L^2 and H^1 norms for the velocity, L^2 norm for the pressure) for decreasing mesh sizes h and values of the trimming-to-element ratio ρ. For each value of ρ, the total error (continuous line) is split in the error on untrimmed (dashed fine line) and cut-elements (dashed line).

6.3.2 Experiments with (weak) Dirichlet boundary conditions

As done in section 5.3.2, a (inhomogeneous) Dirichlet condition enforced weakly as described in section 6.1.

We stress once more that the choice of the non-symmetric formulation (6.1) over the symmetric one (5.1) is made in order to preserve the divergence-conforming property of Raviart Thomas elements. In figure 6.5 it can be seen that while the non-symmetric formulation leads to a divergence-free numerical solution (up to machine precision), the symmetric one does not share this property. In figure 6.6 the error for velocity and pressure is show in several norms. Unlike the case of Neumann boundary conditions or Taylor-Hood elements, the error follows the expected trend and is not affected by the limitations of floating-point arithmetic as seen above. In figure 6.7 we also plot the convergence test in the mesh-dependent norms (5.6) for velocity and (5.7) for pressure, that are the natural norms for the analysis of the method. Also in this case both velocity and pressure errors follow the expected trend.

The results of the stability tests are shown in figure 6.8. Despite the good convergence just observed, the estimates of global coercivity and continuity constants are highly affected

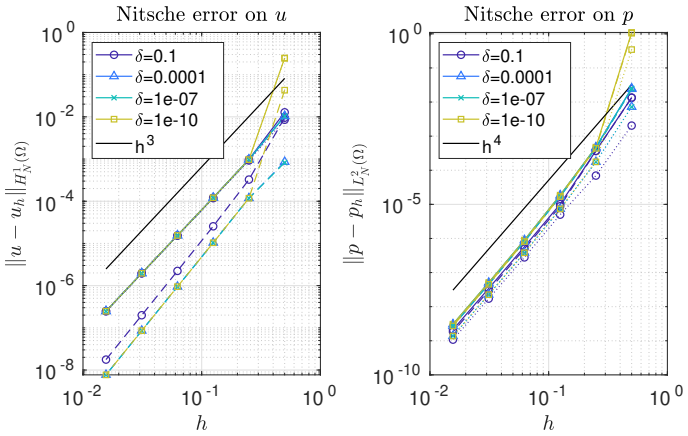

Figure 6.7: Raviart-Thomas with weak Dirichlet B.C.: errors (norm (5.6) for the velocity, (5.7) for the pressure) for decreasing mesh sizes h and values of the trimming-to-element ratio ρ. For each value of ρ, the total error (continuous line) is split in the error on untrimmed (dashed fine line) and cut-elements (dashed line).

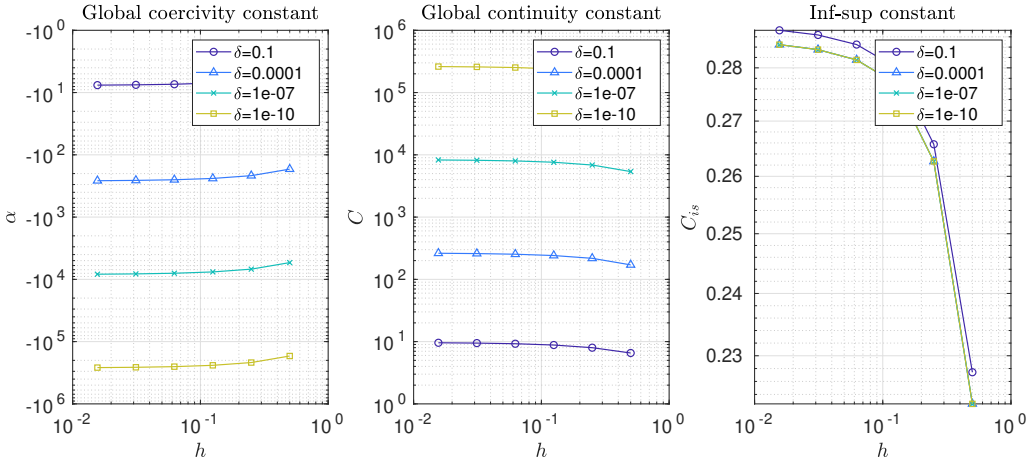

Figure 6.8: Raviart-Thomas with weak Dirichlet B.C.:numerical estimates of global coercivity, global continuity and inf-sup constants for decreasing mesh sizes h and values of the trimming-to-element ratio ρ.

by the valued of the trimming-to-element ratio ρ analogously to the case of Taylor-Hood elements. By contrast, the inf-sup constant converges as h is decreased to a positive finite value for all the values of the trimming-to-element ratio ρ.

6.4 Numerical experiments with stabilization

The stabilized scheme (6.3) is employed. The stabilization is applied on every element for all values of ρ, in other words every cut element is considered a bad cut element (equivalently, the parameter ϑ in definition 1 is chosen as $\vartheta = 1$). The results of the convergence test are plotted in figure 6.9. Surprisingly, the application of the stabilization seems to damage the convergence of the scheme for the smallest value of ρ. In particular, the total L^2 error for velocity is roughly constant for the two smallest mesh-sizes h and the total L^2 error on the pressure increases. For all three norms the error on cut-elements is sub-optimal for the smallest values of ρ and h. Analogous observations can be made observing the convergence test in the mesh-dependent norms shows in figure 6.10

The stability tests for the stabilized scheme are show in figure 6.11. Global coercivity and continuity constants converge to real numbers as h decreases and unlike the non-stabilized

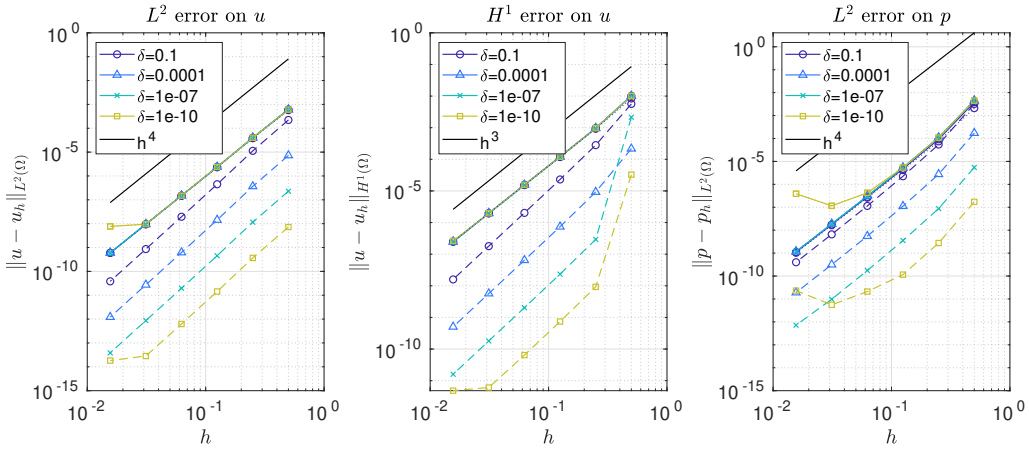

Figure 6.9: Stabilized Raviart-Thomas with weak Dirichlet B.C.: errors (L^2 and H^1 norms for the velocity, L^2 norm for the pressure) for decreasing mesh sizes h and values of the trimming-to-element ratio ρ. For each value of ρ, the total error (continuous line) is split in the error on untrimmed (dashed fine line) and cut-elements (dashed line).

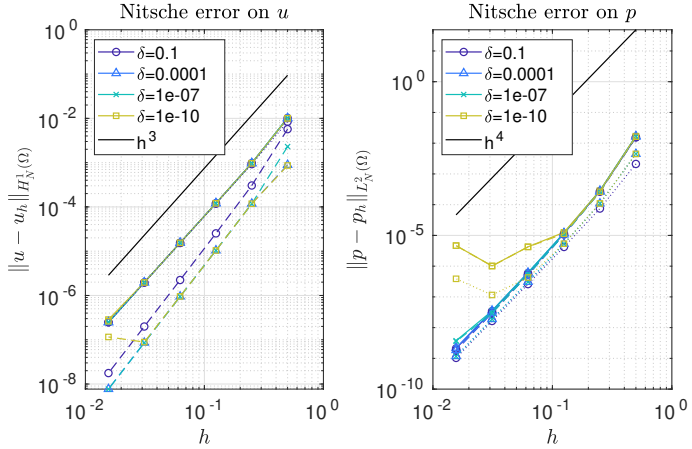

Figure 6.10: Stabilized Raviart-Thomas with weak Dirichlet B.C.: errors (norm (5.6) for the velocity, (5.7) for the pressure) for decreasing mesh sizes h and values of the trimming-to-element ratio ρ. For each value of ρ, the total error (continuous line) is split in the error on untrimmed (dashed fine line) and cut-elements (dashed line).

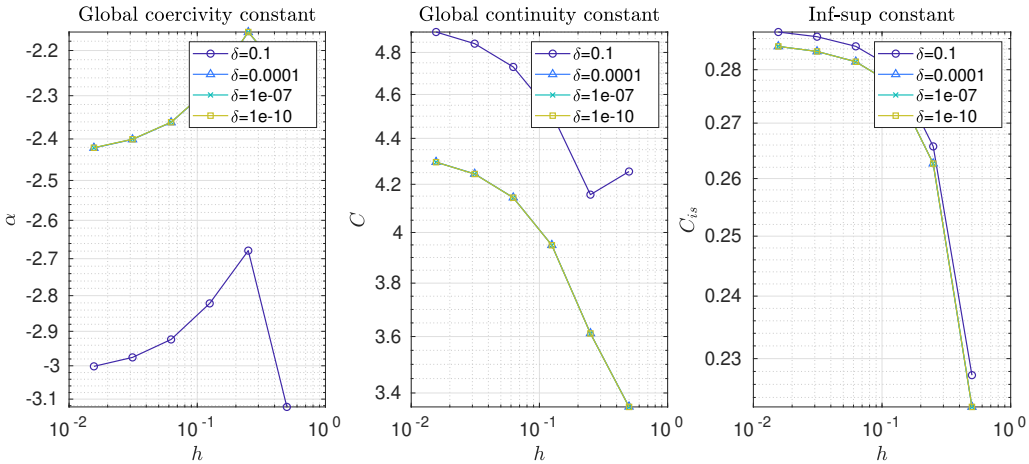

Figure 6.11: Stabilized Raviart-Thomas with weak Dirichlet B.C.:numerical estimates of global coercivity, global continuity and inf-sup constants for decreasing mesh sizes h and values of the trimming-to-element ratio ρ.

case these values are only mildly dependent on the trimming-to-element ratio ρ. The inf-sup constant has the same behaviour as the previous case, showing that the stabilization does not affect negatively the inf-sup stability of the Raviart-Thomas elements.

Chapter 7

Numerical experiments with different domains

In the present chapter, different trimmed domains are considered and the same stability and convergence analysis performed in the previous chapters is carried out. In the first section, a square domain with a diagonal trimming curve is examined. For both Taylor-Hood and Raviart-Thomas elements, the schemes with and without stabilization are assessed. In the second section, the trimming curve is a a quarter of circumference and leads to a trimmed domain that represents a quarter of a plate with a hole. We remark that some of the results presented in this section, such as the suboptimal convergence rate for the pressure obtained from Raviart-Thomas elements, may be caused by problems in the implementation. Therefore, a more detailed analysis of the code is required.

7.1 Diagonal trimming curve

We consider the untrimmed parametric domain $\hat{\Omega}_0 = (0,1) \times (0,1)$ and the identity as parametric-to-physical mapping $\boldsymbol{F}$, so that $\Omega_0 = \hat{\Omega}_0$. The parametric untrimmed mesh $\hat{\mathcal{M}}_{0,h}$ is again defined in a tensor product fashion fixing a number of elements per side n, so that $h = \frac{1}{n}$. The trimming curve in this case is:

$$T_\delta := \Big\{(x,y) \in \hat{\Omega}_0 : y = x + 0.75 + \delta\Big\}$$

where the *trimming thickness* δ is a positive real parameter (smaller than 0.25 to avoid trivial cases). The trimmed domain is $\hat{\Omega} = \Omega := \Big\{(x,y) \in \hat{\Omega}_0 : y \leq x + 0.75 + \delta\Big\}$. An example of such trimmed domain with $\delta = 0.05$ is given in figure 7.1 for two different meshes ($h = 0.25$ and $h = 0.125$). We remark that the active regions of cut-elements (highlighted in green in the figure) have two possible shapes: they are either pentagons or triangles. In figure 7.1 we also mark with a black line the boundaries of the *tiles* the active regions of cut-elements are divided into (the pentagons are divided in two quadrilaterals). This subdivision is used to place quadrature nodes.
We study convergence and stability of the method while refining the mesh ($h \in \{2^{-1}, 2^{-2}, 2^{-3}, 2^{-4}, 2^{-5}, 2^{-6}\}$) and decreasing δ ($\delta \in \{10^{-2}, 10^{-5}, 10^{-8}\}$). Observe that, unlike the mesh used in the previous section, no sliver-cut is present. As a matter of facts, as δ decreases either both area and perimeter of the active parts of cut-elements tend to 0 (the triangles) or neither of the two (pentagons). As a consequence, we do not expect to observe the stability issues that were predicted in Chapter 4. However, the active part of cut-elements either tends to zero (triangles) or approximates a triangle (pentagons) as δ tends to zero, which may cause issues.
The same manufactured solution used in the two previous sections is employed. As

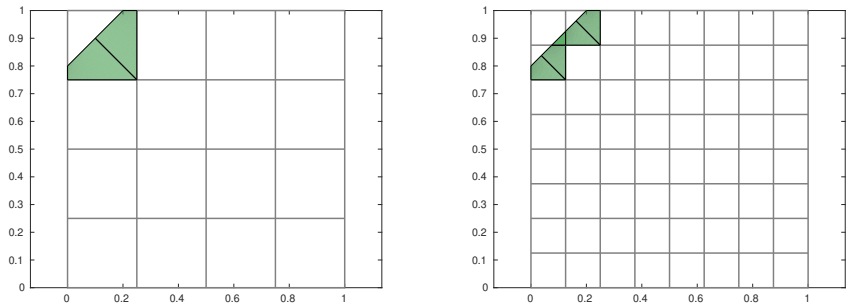

Figure 7.1: Example of trimmed domain with diagonal trimming curve with two meshes.

for boundary conditions, we employ classical Dirichlet conditions on $\{(x,0) : x \in (0,1)\}$ and $\{(1,y) : y \in (0,1)\}$, Neumann boundary conditions on $\{(x,1) : x \in (0.25-\delta, 1)\}$ and $\{(0,y) : y \in (0, 0.75+\delta)\}$ and weak Dirichlet boundary conditions on $\{(x, x+0.75+\delta), x \in (0, 0.25-\delta)\}$. For both Taylor-Hood and Raviart-Thomas elements we will choose degree $p = 3$ and regularity $\alpha = 2$ (as in the definitions (3.15) and (3.16)). In this case $(d+3)^2$ quadrature points are used to integrate the shape functions on the active part of cut-elements and $d+3$ on their boundary. If only $(d+1)^2$ and $d+1$ quadrature nodes were used as in chapters 5 and 6 the integration of shape functions would be inaccurate. As in the previous chapter, when studying convergence the Nitsche parameter is defined as $C_{pen} = 10(d+1)$ while when studying stability as $C_{pen} = 1$. The diagonal preconditioner described in chapter 8 is used.

7.1.1 Taylor-Hood elements

We start by showing an example of numerical solution obtained with Taylor-Hood elements with $n = 8$ elements per parametric direction. in figure 7.2 the computed velocity, pressure and divergence of the velocity are plotted. In figure 7.3 the error distribution for velocity and pressure are plotted. The convergence and stability tests carried out in the previous two chapters for Taylor-Hood elements are repeated. In figure 7.4 and 7.5 the convergence analysis for standard and mesh-dependent norms respectively are plotted. Th error follows the theoretical Taylor-Hood convergence rates except for the pressure error measured in the mesh-dependent norm 5.7 for the smallest values of the trimming-thickness δ. This phenomenon is probably caused by round-off errors as seen in chapter 5. In figure 7.6 the results of the stability tests are shown. The estimates of global coercivity and continuity constants seem to converge to real values as h is decreased independently of the trimming-thickness δ. Finally, a dependence between the inf-sup constant and the value of δ can clearly be observed. In particular, as δ decreases also the inf-sup constant decreases. By contrast, as h decreases the inf-sup constant increases and seems to converge (for the values of h tested here) only in the case $\delta = 0.01$. The present behaviour of the inf-sup constant (that was not seen in the previous numerical experiments) may be caused by the different shapes taken by the active parts of cut-elements. The same convergence and stability analysis is carried out applying the stabilization (5.13). The parameter to distinguish bad and good cut-elements is chosen as $\vartheta = 0.25$ in order to apply the stabilization on cut-elements with *triangular* active region only. The results of the convergence tests in figures 7.7 and 7.8 show that the application of the stabilization does not have a big impact of the convergence properties of the scheme. Finally, the stability test in figure 7.6 shows that appying the stabilization makes global coercivity and continuity constant completely independent of δ, while in the case of the scheme without stabilization values of the stability constants were different for $\delta = 10^{-2}$.

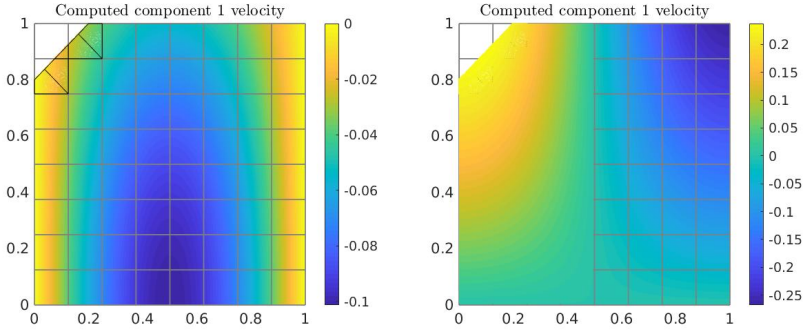

(a)

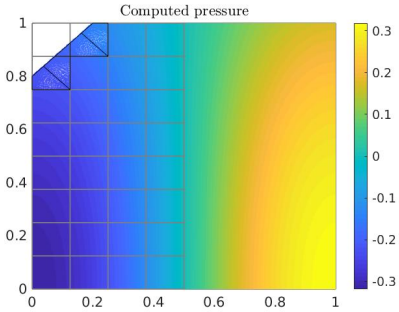

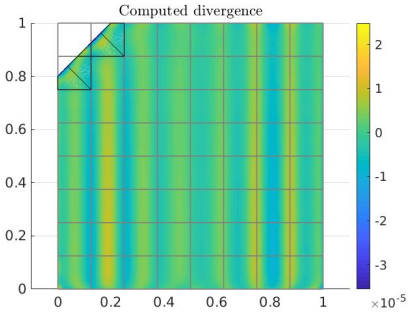

(b) **(c)**

Figure 7.2: Computed velocity (a) and pressure (b) obtained with Taylor-Hood elements on trimmed domain with diagonal trimming curve. Divergence of the numerical solution (c).

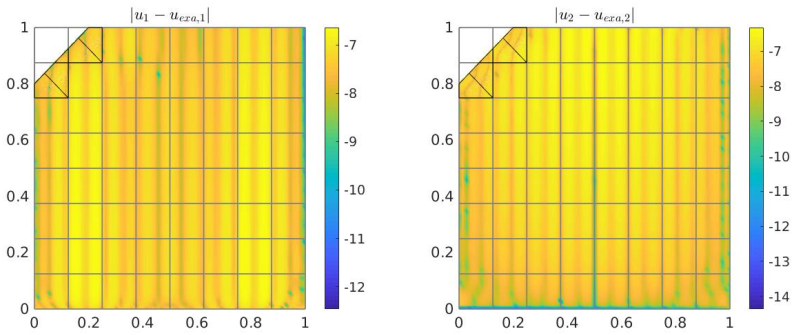

(a)

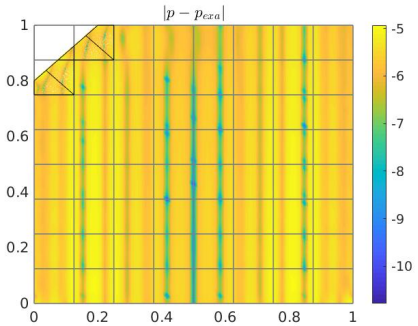

(b)

Figure 7.3: Error distribution of the numerical velocity (a) and pressure (b) obtained with Taylor-Hood elements on a trimmed domain. Both quantities as plotted in log-scale.

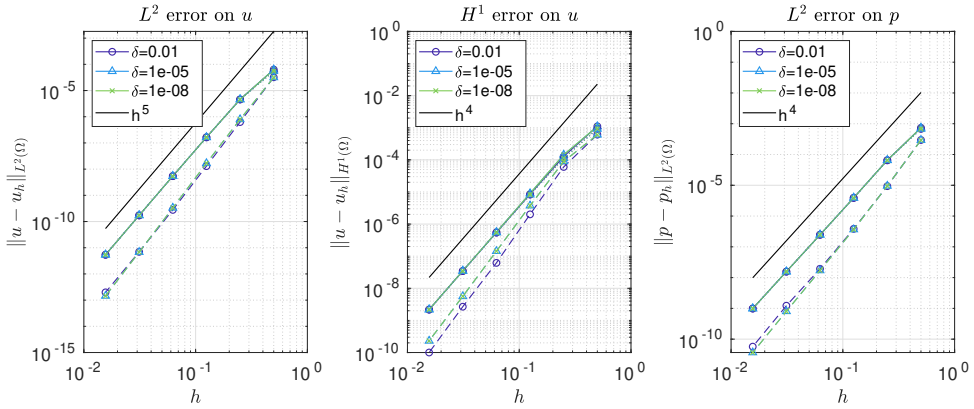

Figure 7.4: Taylor-Hood on domain with diagonal trimming curve: errors (L^2 and H^1 norms for the velocity, L^2 norm for the pressure) for decreasing mesh sizes h and values of the trimming-thickness δ. For each value of δ, the total error (continuous line) is split in the error on untrimmed (dashed fine line) and cut-elements (dashed line).

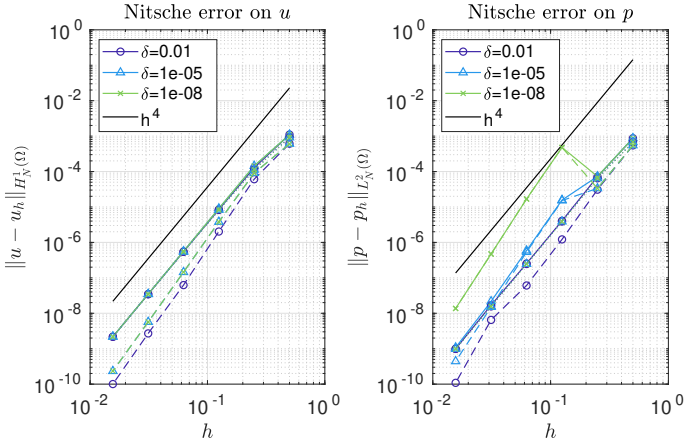

Figure 7.5: Taylor-Hood on domain with diagonal trimming curve: errors (norm (5.6) for the velocity, (5.7) for the pressure) for decreasing mesh sizes h and values of the trimming-thickness δ. For each value of δ, the total error (continuous line) is split in the error on untrimmed (dashed fine line) and cut-elements (dashed line).

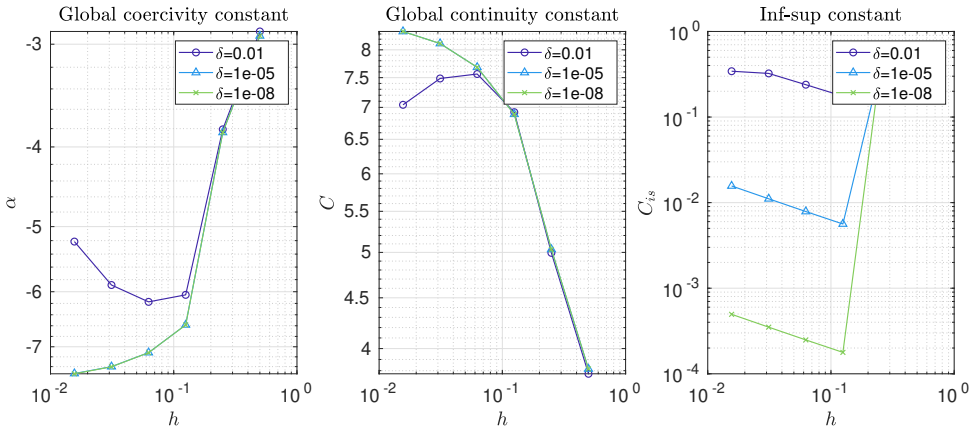

Figure 7.6: Taylor-Hood on domain with diagonal trimming curve: numerical estimates of global coercivity, global continuity and inf-sup constants for decreasing mesh sizes h and values of the trimming-thickness δ.

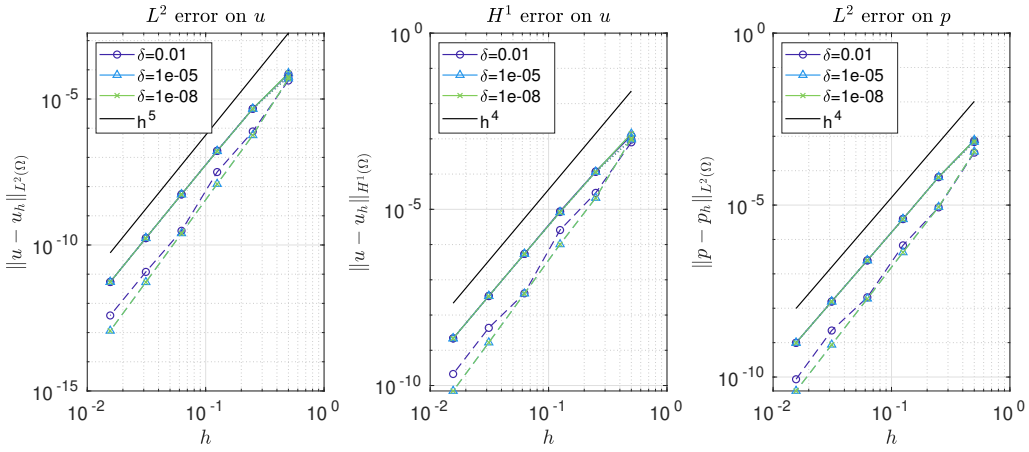

Figure 7.7: Stabilized Taylor-Hood on domain with diagonal trimming curve: errors (L^2 and H^1 norms for the velocity, L^2 norm for the pressure) for decreasing mesh sizes h and values of the trimming-thickness δ. For each value of δ, the total error (continuous line) is split in the error on untrimmed (dashed fine line) and cut-elements (dashed line).

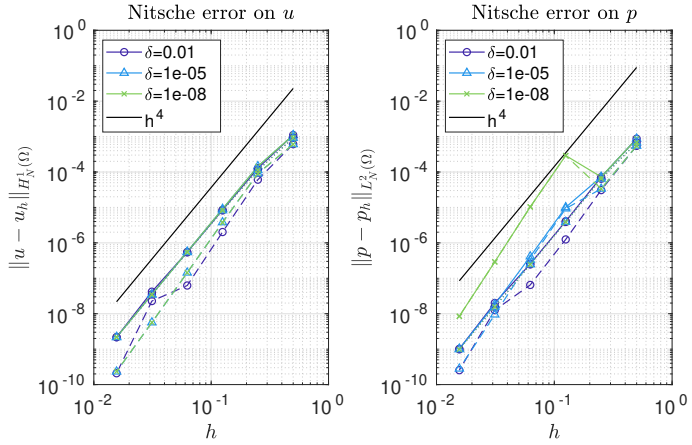

Figure 7.8: Stabilized Taylor-Hood on domain with diagonal trimming curve: errors (norm (5.6) for the velocity, (5.7) for the pressure) for decreasing mesh sizes h and values of the trimming-thickness δ. For each value of δ, the total error (continuous line) is split in the error on untrimmed (dashed fine line) and cut-elements (dashed line).

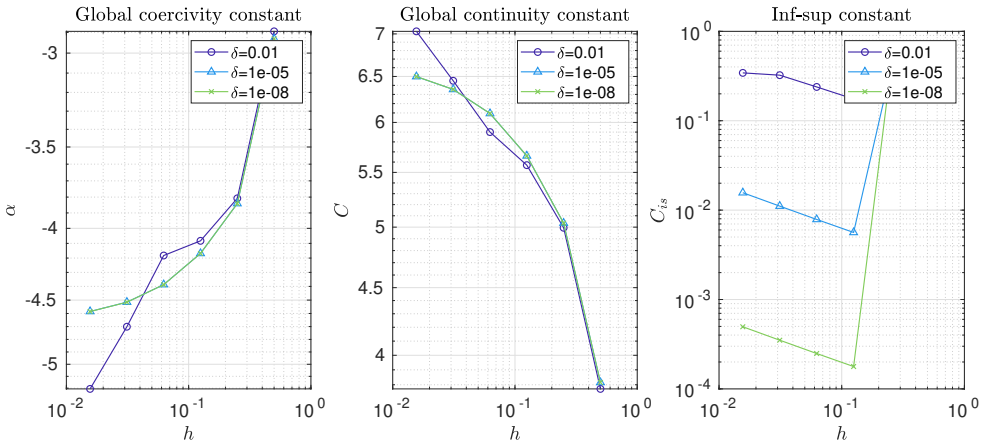

Figure 7.9: Stabilized Taylor-Hood on domain with diagonal trimming curve: numerical estimates of global coercivity, global continuity and inf-sup constants for decreasing mesh sizes h and values of the trimming-thickness δ.

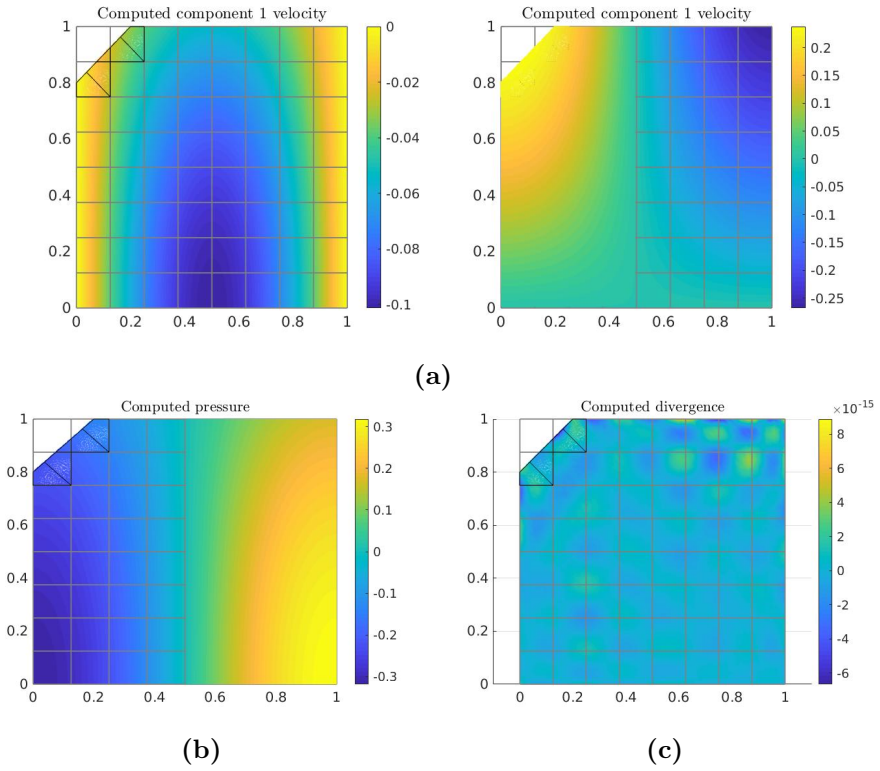

Figure 7.10: Computed velocity (a) and pressure (b) obtained with Raviart-Thomas elements on trimmed domain with diagonal trimming curve. Divergence of the numerical solution (c).

7.1.2 Raviart-Thomas elements

We start by showing an example of numerical solution obtained with Raviart-Thomas elements with $n = 8$ elements per parametric direction. in figure 7.10 the computed velocity, pressure and divergence of the velocity are plotted. In figure 7.11 the error distribution for velocity and pressure are plotted. Analogously to the previous section, convergence and stability tests are first presented for the scheme without stabilization. The convergence tests presented in figures 7.12 and 7.13 show that while the velocity error has the expected rate of convergence, both L^2 and mesh-dependent errors on the pressure are sub-optimal by one order. Moreover, in the case of the mesh-dependent norm (5.7) it can be seen that the error increases when δ is decreased. The results of the stability test in figure 7.14 shows a behaviour that is similar to the one seen above in the case of Taylor-Hood elements. Global coercivity and continuity constants seem to be bounded both as functions of h and δ, the inf-sup constant again decreases with δ, increases slightly with respect to h and seems to converge only for $\delta = 0.01$. The stabilized scheme defined in (6.3) is applied with $\vartheta = 0.25$ again to stabilize only on the cut-elements with triangular active region. Convergence results can be seen in figure 7.15 and 7.16. As in the case of the experiments without stabilization, the pressure converges sub-optimally in both the norms. However, in this case the error on cut-elements is higher when $\delta = 10^{-2}$ and for the other values of δ is about the same order of the error on untrimmed elements(unlike in the non-stabilized case). The stability test in figure 7.17 shows that the application of the stabilization makes the global continuity and coercivity constant less dependent on δ than in the previous case, while the values of the inf-sup constant are unchanged.

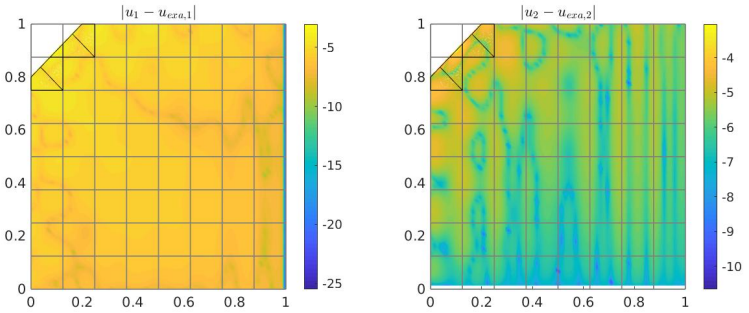

(a)

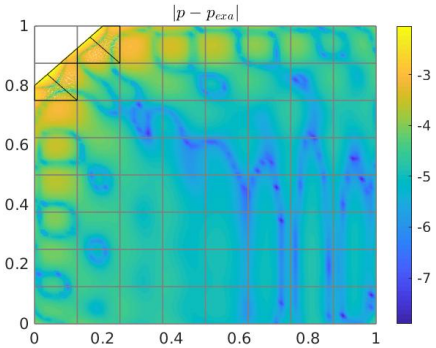

(b)

Figure 7.11: Error distribution of the numerical velocity (a) and pressure (b) obtained with Raviart-Thomas elements on a trimmed domain. Both quantities as plotted in log-scale.

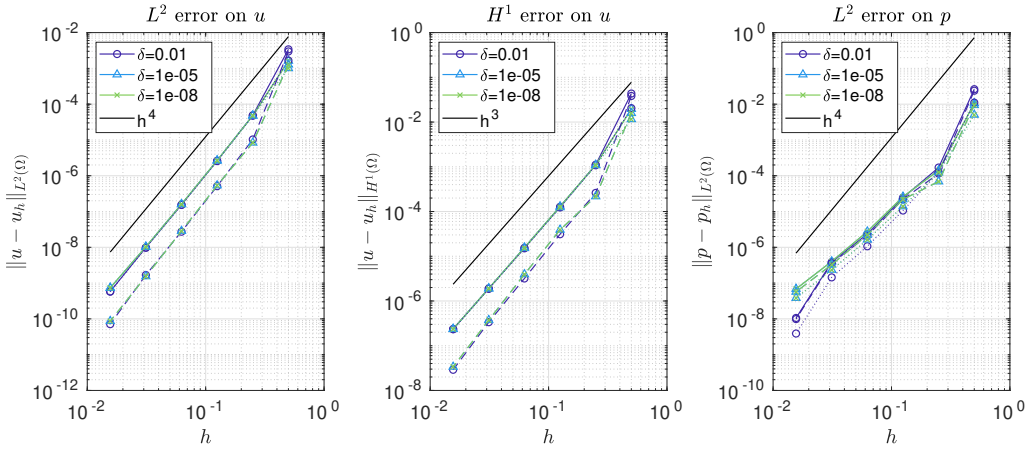

Figure 7.12: Raviart-Thomas on domain with diagonal trimming curve: errors (L^2 and H^1 norms for the velocity, L^2 norm for the pressure) for decreasing mesh sizes h and values of the trimming-thickness δ. For each value of δ, the total error (continuous line) is split in the error on untrimmed (dashed fine line) and cut-elements (dashed line).

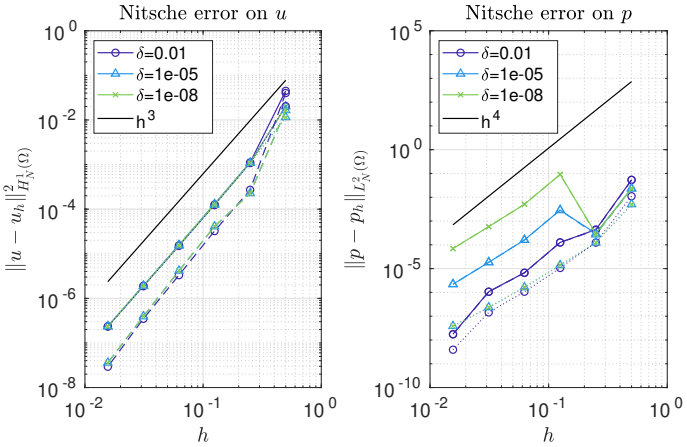

Figure 7.13: Raviart-Thomas on domain with diagonal trimming curve: errors (norm (5.6) for the velocity, (5.7) for the pressure) for decreasing mesh sizes h and values of the trimming-thickness δ. For each value of δ, the total error (continuous line) is split in the error on untrimmed (dashed fine line) and cut-elements (dashed line).

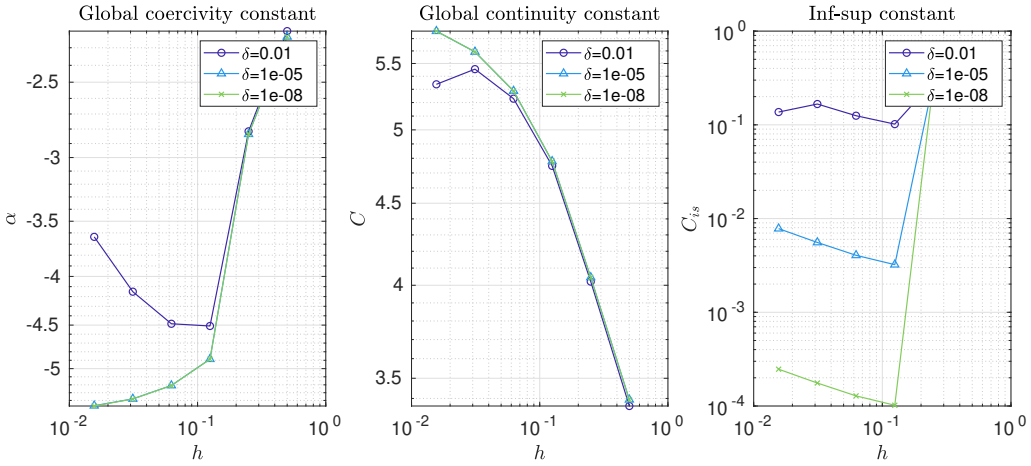

Figure 7.14: Raviart-Thomas on domain with diagonal trimming curve: numerical estimates of global coercivity, global continuity and inf-sup constants for decreasing mesh sizes h and values of the trimming-thickness δ.

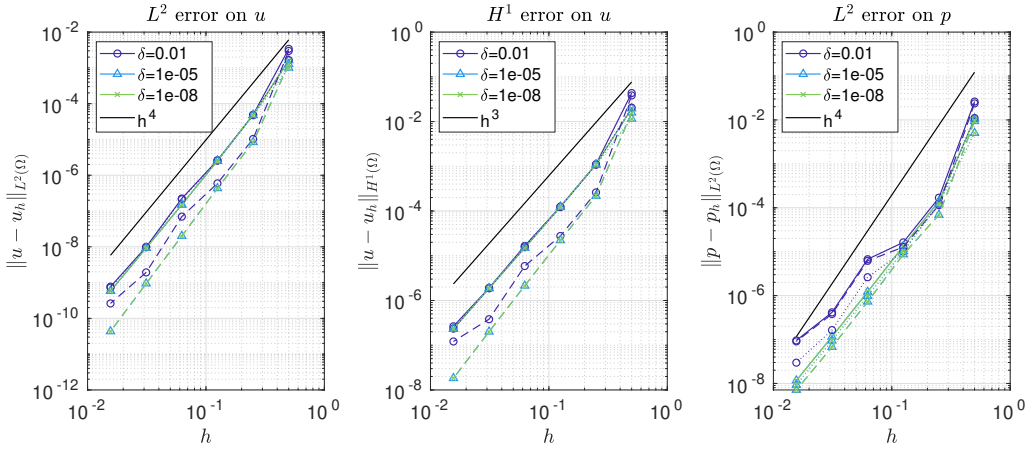

Figure 7.15: Stabilized Raviart-Thomas on domain with diagonal trimming curve: errors (L^2 and H^1 norms for the velocity, L^2 norm for the pressure) for decreasing mesh sizes h and values of the trimming-thickness δ. For each value of δ, the total error (continuous line) is split in the error on untrimmed (dashed fine line) and cut-elements (dashed line).

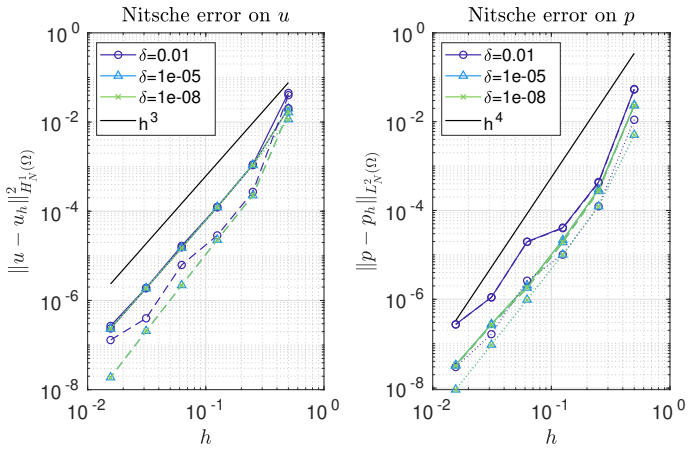

Figure 7.16: Stabilized Raviart-Thomas on domain with diagonal trimming curve: errors (norm (5.6) for the velocity, (5.7) for the pressure) for decreasing mesh sizes h and values of the trimming-thickness δ. For each value of δ, the total error (continuous line) is split in the error on untrimmed (dashed fine line) and cut-elements (dashed line).

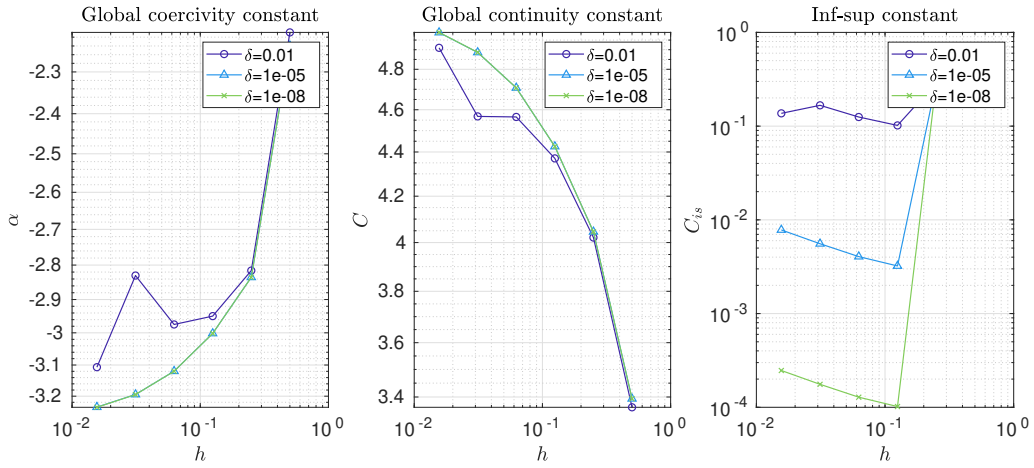

Figure 7.17: Stabilized Raviart-Thomas on domain with diagonal trimming curve: numerical estimates of global coercivity, global continuity and inf-sup constants for decreasing mesh sizes h and values of the trimming-thickness δ.

7.2 Quarter plate with hole

The same setting of the previous section is considered. However, this time the trimming curve is:

$$T_\delta := \left\{(x,y) \in \hat{\Omega}_0 : x^2 + y^2 = (0.5-\delta)^2\right\}$$

where the *trimming thickness* δ is a positive real parameter smaller than 0.5 to avoid trivial cases. The trimmed domain is $\hat{\Omega} = \Omega := \left\{(x,y) \in \hat{\Omega}_0 : x^2 + y^2 \geq (0.5-\delta)^2\right\}$. An example of such trimmed domain with $\delta = 0.01$ is given in figure 7.18 for $h = 0.25$ and $h = 0.125$. We remark that in this case the active part of trimmed elements can take a number of different shapes and can change in different ways as δ tends to zero. In particular, both sliver cuts and triangular elements may be present, possibly leading to the instabilities observed in the previous numerical experiments. We study convergence and stability of the method for the same values of h and δ used in the previous section. Also the same manufactured solution is used. In this case boundary conditions are: classical Dirichlet conditions on $\{(1,y) : y \in (0,1)\}$ and $\{(x,1) : x \in (0,1)\}$, Neumann boundary conditions on $\{(x,0) : x \in (0.5-\delta, 1)\}$ and $\{(0,y) : y \in (0.5-\delta, 1)\}$ and weak Dirichlet boundary conditions on $\left\{(x, \sqrt{(0.5-\delta)^2 - x^2}, x \in (0, 0.5-\delta)\right\}$. For both Taylor-Hood and Raviart-Thomas elements we choose degree $p = 3$ and regularity $\alpha = 2$ (as in the definitions (3.15) and (3.16)). In this case $(d+10)^2$ quadrature points are used to integrate the shape functions on the active part of cut-elements and $d + 10$ on their boundary. This increased value is again needed to accurately approximate integrals on cut-elements (but note that in may not be the lowest). In this case the Nitsche parameter is set to $C_{pen} = 10(d+1)$ while when studying stability as $C_{pen} = 1$. The diagonal preconditioner described in chapter 8 is used.

7.2.1 Taylor-Hood elements

We start by showing an example of numerical solution obtained with Taylor-Hood elements with $n = 8$ elements per parametric direction. in figure 7.19 the computed velocity, pressure and divergence of the velocity are plotted. In figure 7.20 the error distribution for velocity and pressure are plotted. Convergence and stability tests are carried out for Taylor-Hood elements in the present setting. In figure 7.21 and 7.22 the convergence analysis for standard and mesh-dependent norms respectively is plotted. Th error follows the theoretical Taylor-Hood convergence rates. In figure 7.23 the results of the stability tests are shown. The estimates of global coercivity and continuity constants seem to diverge as h decreases for all values of δ. This can be attributed to the presence of sliver-cuts (for instance, in the leftmost and rightmost elements in mesh). The estimate

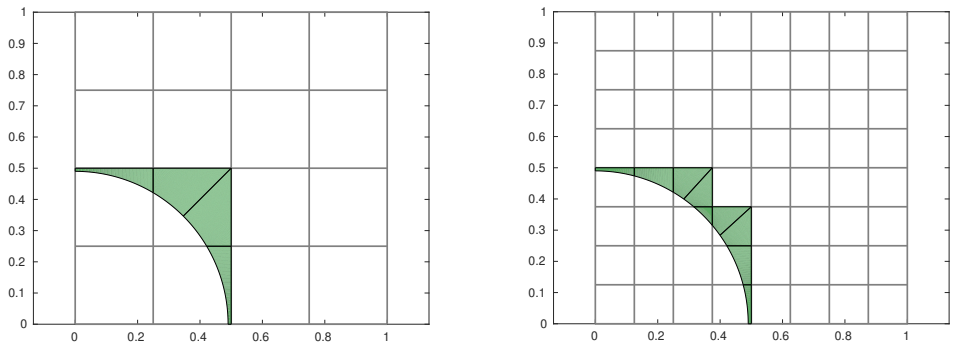

Figure 7.18: Example of trimmed domain with circular curve with two meshes.

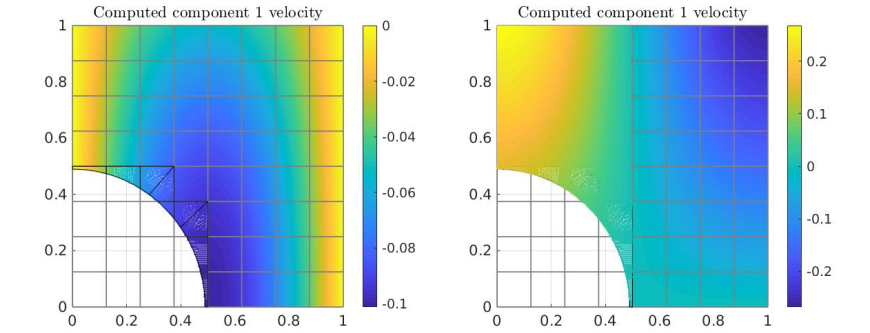

(a)

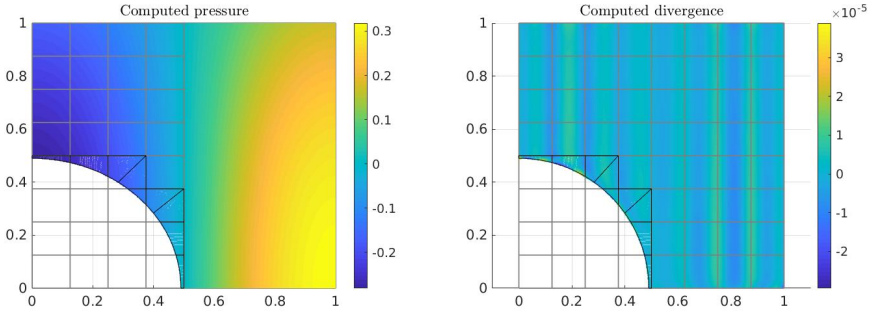

(b) **(c)**

Figure 7.19: Computed velocity (a) and pressure (b) obtained with Taylor-Hood elements on trimmed domain with circular trimming curve. Divergence of the numerical solution (c).

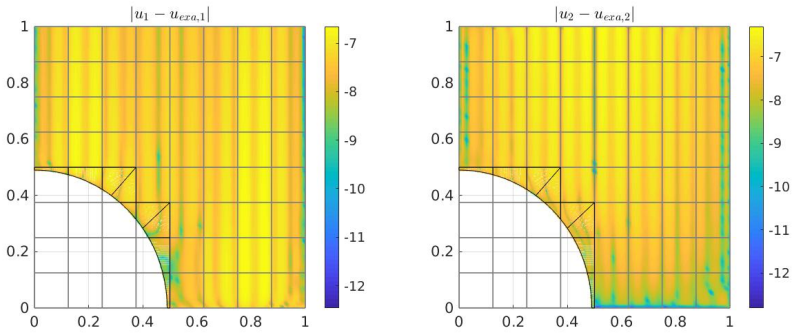

(a)

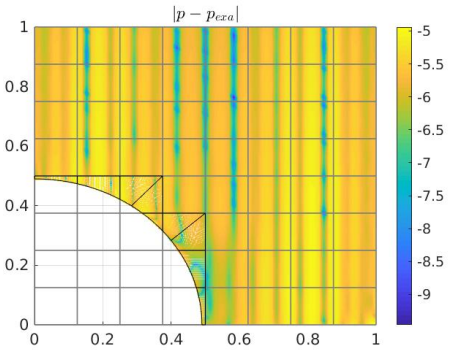

(b)

Figure 7.20: Error distribution of the numerical velocity (a) and pressure (b) obtained with Taylor-Hood elements on the trimmed domain with circular trimming curve. Both quantities as plotted in log-scale.

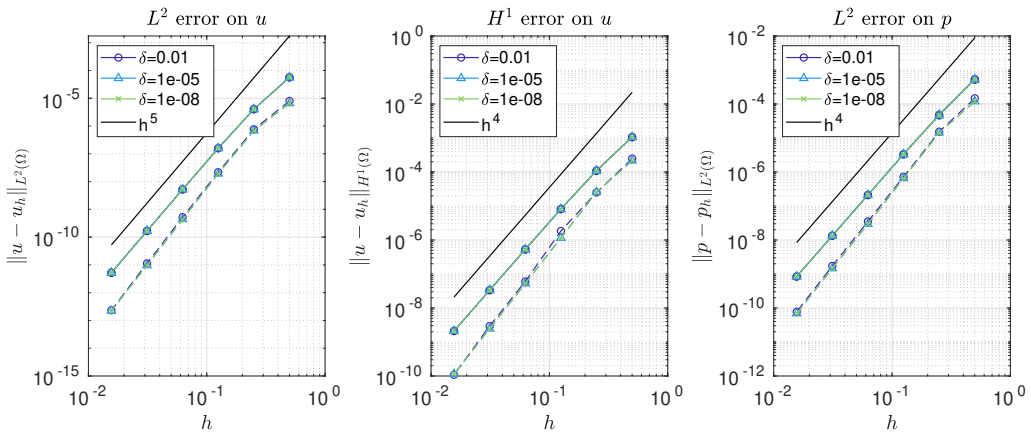

Figure 7.21: Taylor-Hood on domain with circular trimming curve: errors (L^2 and H^1 norms for the velocity, L^2 norm for the pressure) for decreasing mesh sizes h and values of the trimming-thickness δ. For each value of δ, the total error (continuous line) is split in the error on untrimmed (dashed fine line) and cut-elements (dashed line).

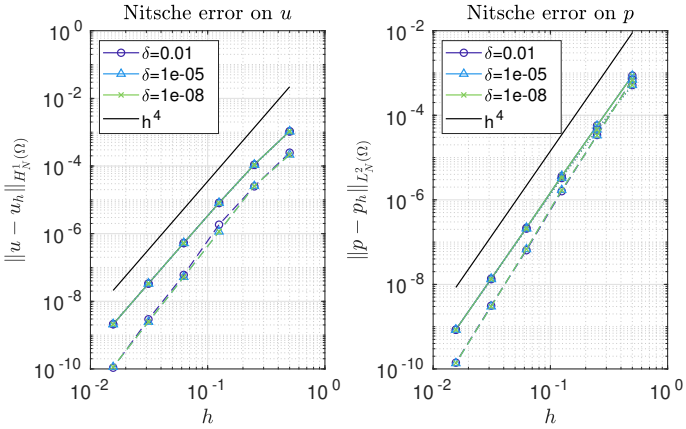

Figure 7.22: Taylor-Hood on domain with circular trimming curve: errors (norm (5.6) for the velocity, (5.7) for the pressure) for decreasing mesh sizes h and values of the trimming-thickness δ. For each value of δ, the total error (continuous line) is split in the error on untrimmed (dashed fine line) and cut-elements (dashed line).

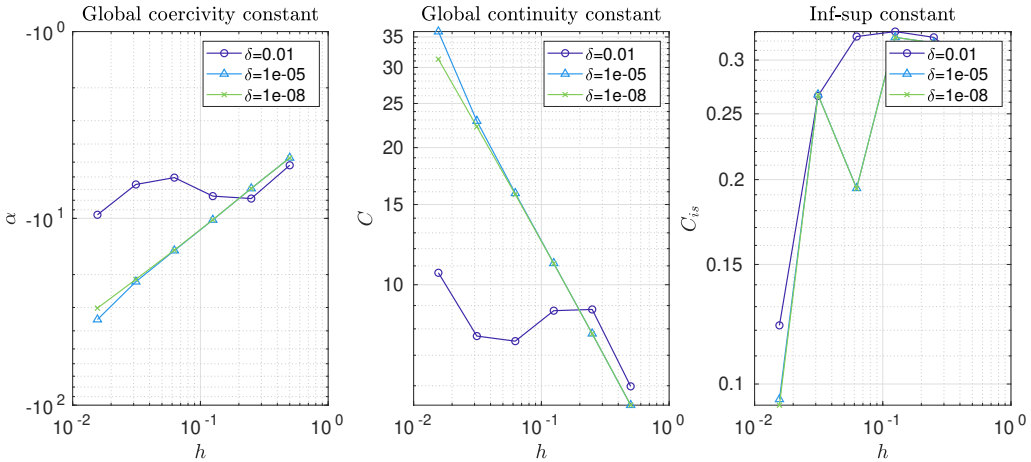

Figure 7.23: Taylor-Hood on domain with circular trimming curve: numerical estimates of global coercivity, global continuity and inf-sup constants for decreasing mesh sizes h and values of the trimming-thickness δ.

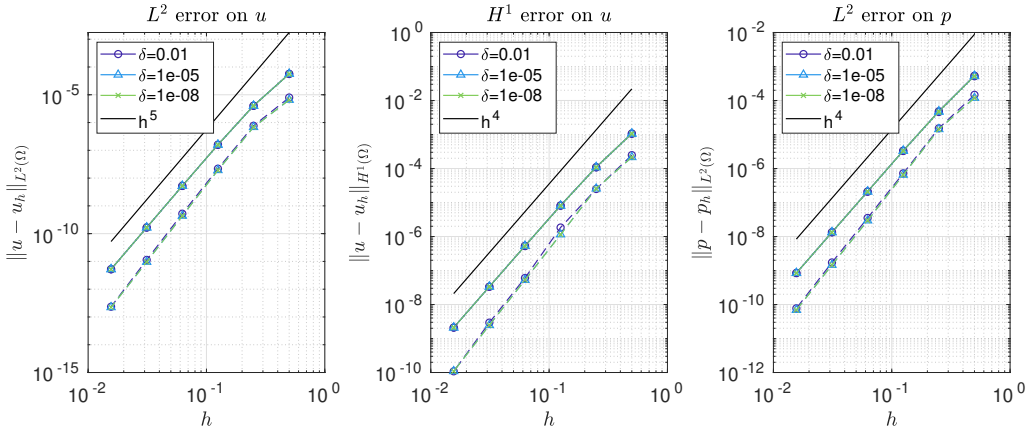

Figure 7.24: Stabilized Taylor-Hood on domain with circular trimming curve: errors (L^2 and H^1 norms for the velocity, L^2 norm for the pressure) for decreasing mesh sizes h and values of the trimming-thickness δ. For each value of δ, the total error (continuous line) is split in the error on untrimmed (dashed fine line) and cut-elements (dashed line).

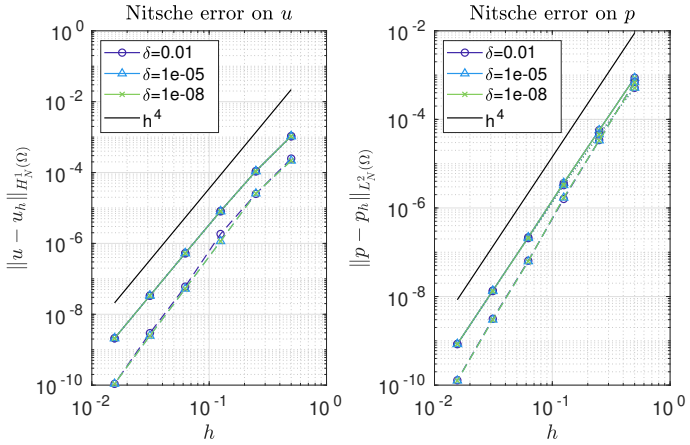

Figure 7.25: Stabilized Taylor-Hood on domain with circular trimming curve: errors (norm (5.6) for the velocity, (5.7) for the pressure) for decreasing mesh sizes h and values of the trimming-thickness δ. For each value of δ, the total error (continuous line) is split in the error on untrimmed (dashed fine line) and cut-elements (dashed line).

of the inf-sup constant tends to zero as h decreases for all δ. While in the case of the diagonal trimming curve the inf-sup constant has an abrupt decrese for $\delta \in \{10^{-5}, 10^{-8}\}$, in this case the decrease is less sudden but is present for all values of δ. The same convergence and stability analysis is carried out applying the stabilization (5.13). The parameter to distinguish bad and good cut-elements is chosen as $\vartheta = 0.01$. The results of the convergence tests in figures 7.24 and 7.25 show that as in the non-stabilized case the optimal Taylor-Hood rates of convergence are obtained. Finally, the stability test in figure 7.26 shows that the application of the stabilization prevent global coercivity and continuity constants to diverge as h decreases. In this case the estimates of the two stability constants seem to oscillate but remain bounded. Results for inf-sup stability are as in the non-stabilized case.

7.2.2 Raviart-Thomas elements

We start by showing an example of numerical solution obtained with Raviart-Thomas elements with $n = 8$ elements per parametric direction. in figure 7.27 the computed velocity, pressure and divergence of the velocity are plotted. In figure 7.28 the error

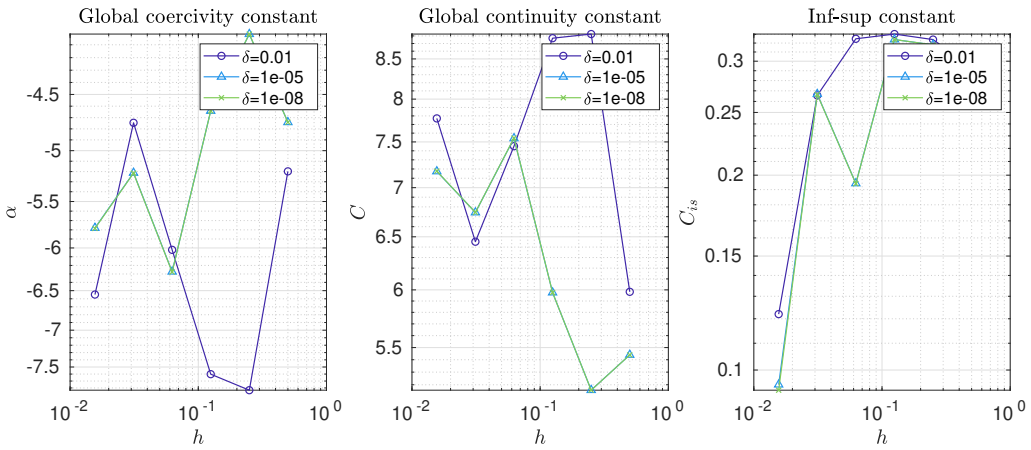

Figure 7.26: Stabilized Taylor-Hood on domain with circular trimming curve: numerical estimates of global coercivity, global continuity and inf-sup constants for decreasing mesh sizes h and values of the trimming-thickness δ.

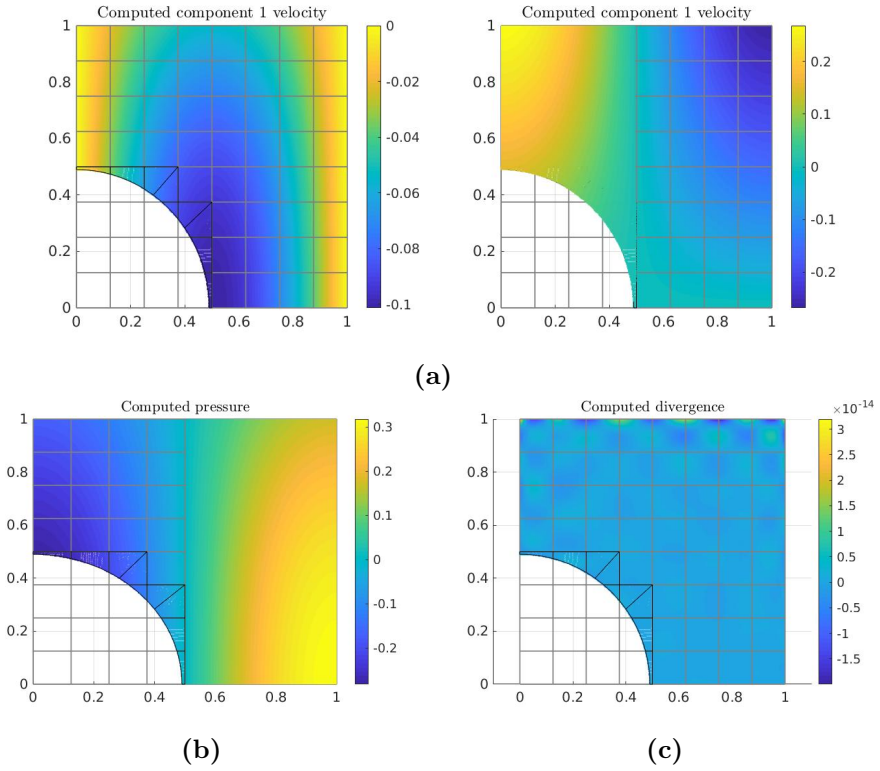

Figure 7.27: Computed velocity (a) and pressure (b) obtained with Raviart-Thomas elements on the trimmed domain with circular trimming curve. Divergence of the numerical solution (c).

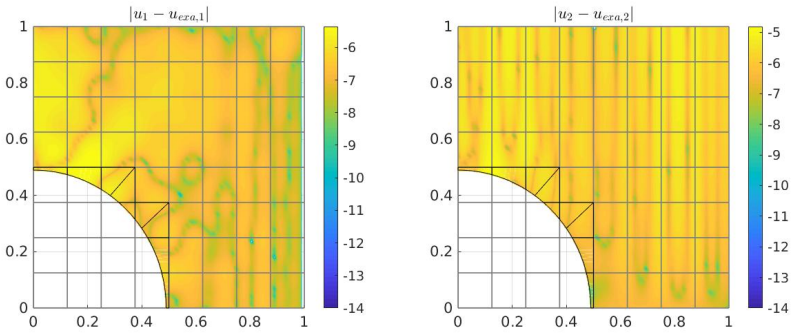

(a)

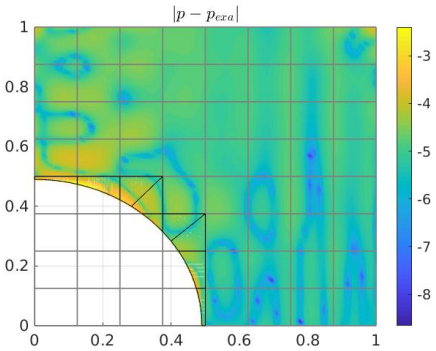

(b)

Figure 7.28: Error distribution of the numerical velocity (a) and pressure (b) obtained with Raviart-Thomas elements on the trimmed domain with circular trimming curve. Both quantities as plotted in log-scale.

distribution for velocity and pressure are plotted. Convergence and stability tests are first presented for the scheme without stabilization. The convergence tests presented in figures 7.29 and 7.30 show that while the velocity errors have the expected rate of convergence, both L^2 and mesh-dependent errors on the pressure show an irregular behaviour. The results of the stability test are analogous to the ones obtained with Taylor-Hood elements on the same domain. In particular, global coercivity and continuity constant diverge as h decreases for all values of the trimming-thickness δ. The inf-sup constant tends to zero as h tends to zero for all δ. The stabilized scheme defined in (6.3) is applied with $\vartheta = 0.01$. Convergence results can be seen in figure 7.32 and 7.33. Again, the convergence rates for velocity are the expected ones. As for the errors on the pressure, it can be seen that it decreases more regularly than in the non-stabilized case, however it does so with a slightly suboptimal rate. The effect of the stabilization on the stability constants is analogous to the one seen in the case of Taylor-Hood elements on the same domain. Global continuity and coercivity constants are now bounded with respect to h for all δ and the inf-sup constant still tends to zero as h is decreased.

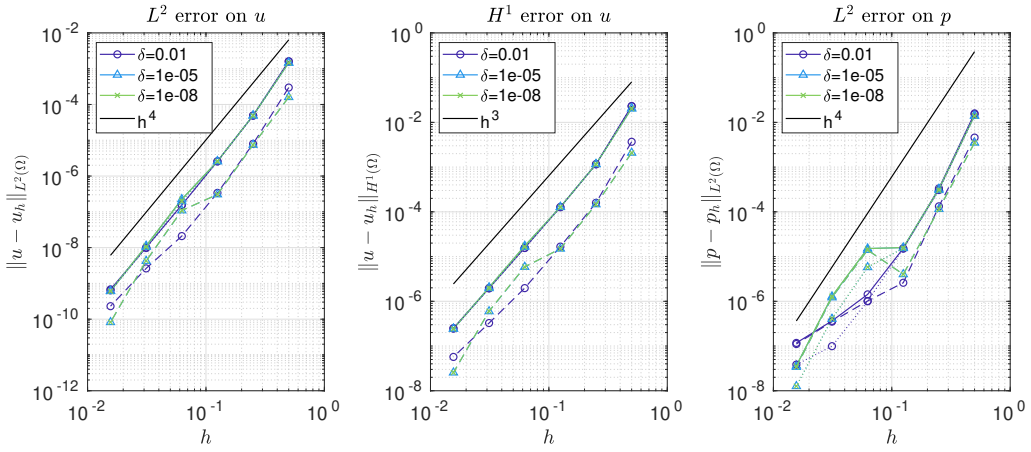

Figure 7.29: Raviart-Thomas on domain with circular trimming curve: errors (L^2 and H^1 norms for the velocity, L^2 norm for the pressure) for decreasing mesh sizes h and values of the trimming-thickness δ. For each value of δ, the total error (continuous line) is split in the error on untrimmed (dashed fine line) and cut-elements (dashed line).

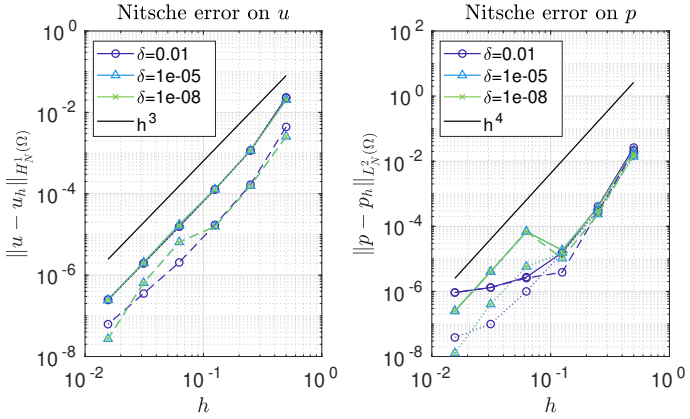

Figure 7.30: Raviart-Thomas on domain with circular trimming curve: errors (norm (5.6) for the velocity, (5.7) for the pressure) for decreasing mesh sizes h and values of the trimming-thickness δ. For each value of δ, the total error (continuous line) is split in the error on untrimmed (dashed fine line) and cut-elements (dashed line).

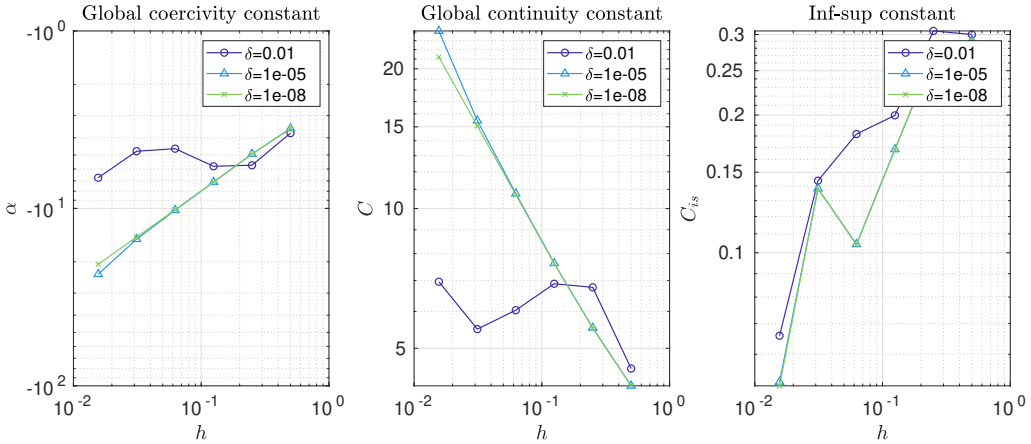

Figure 7.31: Raviart-Thomas on domain with circular trimming curve: numerical estimates of global coercivity, global continuity and inf-sup constants for decreasing mesh sizes h and values of the trimming-thickness δ.

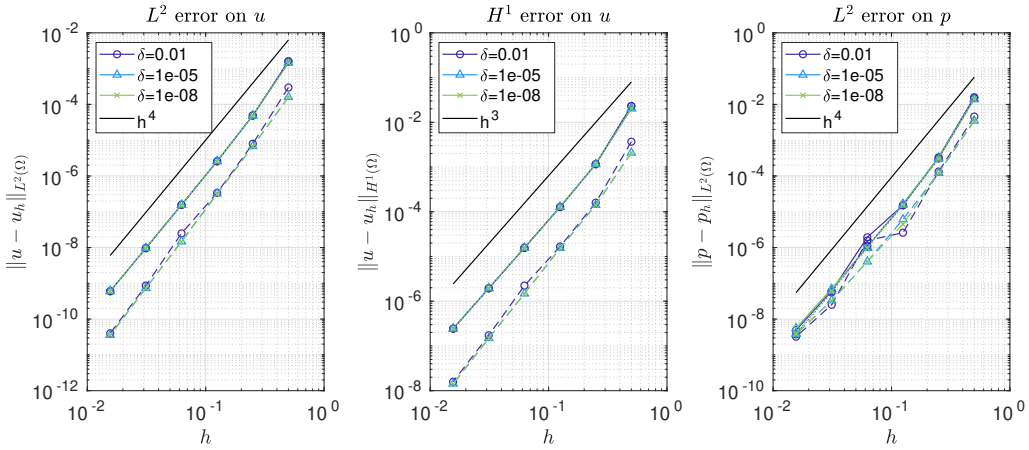

Figure 7.32: Stabilized Raviart-Thomas on domain with circular trimming curve: errors (L^2 and H^1 norms for the velocity, L^2 norm for the pressure) for decreasing mesh sizes h and values of the trimming-thickness δ. For each value of δ, the total error (continuous line) is split in the error on untrimmed (dashed fine line) and cut-elements (dashed line).

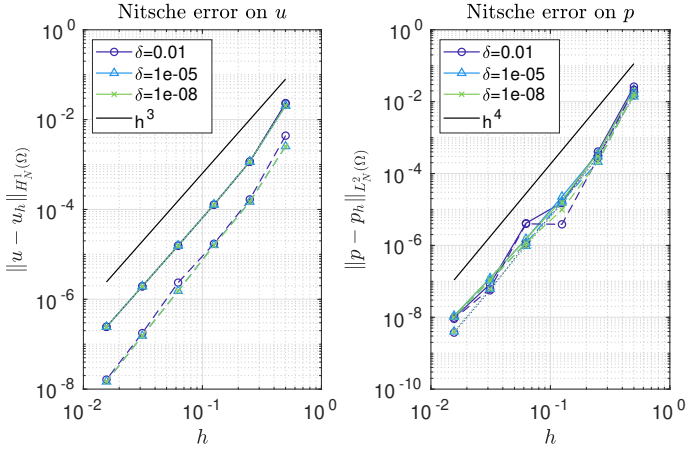

Figure 7.33: Stabilized Raviart-Thomas on domain with circular trimming curve: errors (norm (5.6) for the velocity, (5.7) for the pressure) for decreasing mesh sizes h and values of the trimming-thickness δ. For each value of δ, the total error (continuous line) is split in the error on untrimmed (dashed fine line) and cut-elements (dashed line).

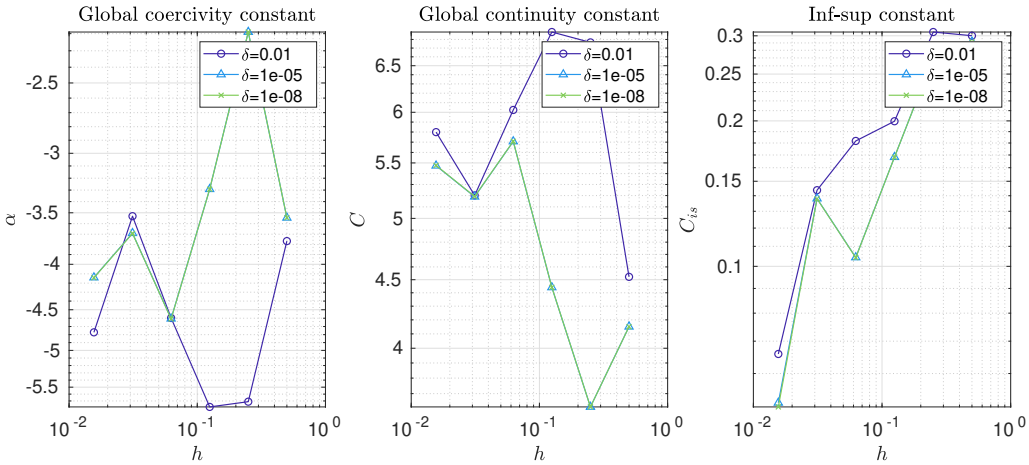

Figure 7.34: Stabilized Raviart-Thomas on domain with circular trimming curve: numerical estimates of global coercivity, global continuity and inf-sup constants for decreasing mesh sizes h and values of the trimming-thickness δ.

Chapter 8

Preconditioning

In this short chapter we define the preconditioner employed in the numerical experiments presented in the previous chapters. In the first section, an intuitive explanation of the behaviour of the conditioning number for the problem at hand and the preconditioner is defined. In the second section numerical experiments are presented to assess the effectiveness of the preconditioner for both Taylor-Hood and Raviart-Thomas elements.

8.1 A diagonal preconditioner

We consider the linear system:

$$S\boldsymbol{x} = \boldsymbol{b}$$

that can correspond either to the algebraic form of the Taylor-Hood problem (5.8) or the Raviart-Thomas problem (6.2). The problem can be ill-conditioned depending on the size of the cut-elements. As suggested in [12], ill-conditioning is caused by the presence of cut-elements $K \in \mathcal{G}_h$ that have an active part $K \cap \Omega$ that consist of a small volume fraction of K. The following diagonal preconditioner is proposed:

$$P := \begin{pmatrix} P_A & \mathbf{0} \\ \mathbf{0} & P_p \end{pmatrix} \tag{8.1}$$

where

$$\begin{aligned} P_A \in \mathbb{R}^{N,N} \qquad & (P_A)_{i,j} = \frac{\delta_{i,j}}{\sqrt{(A)_{i,j}}}, \\ P_p \in \mathbb{R}^{N,N} \qquad & (P_p)_{i,j} = \frac{\delta_{i,j}}{\sqrt{(M_p)_{i,j}}}, \end{aligned}$$

$\delta_{i,j}$ is the classical Kronecker symbol, A is the first block of both the Taylor-Hood and Raviart-Thomas stiffness matrix (5.9) and $M_p \in \mathbb{R}^{M,M}$ is the mass matrix (5.11) associated to the norm (5.7). The following centered preconditioning strategy is applied:

1. Solve $PSP\bar{\boldsymbol{x}} = P\boldsymbol{b}$
2. Compute $\boldsymbol{x} = P^{-1}\bar{\boldsymbol{x}}$.

8.2 Numerical experiments

As an example, we assemble the stiffness matrix of the problem with weak Dirichlet boundary conditions presented in section 5.3.2 (for Taylor-Hood elements) or 6.3.2 (for Raviart-THomas elements) and observe what is the effect of the preconditioner proposed in the

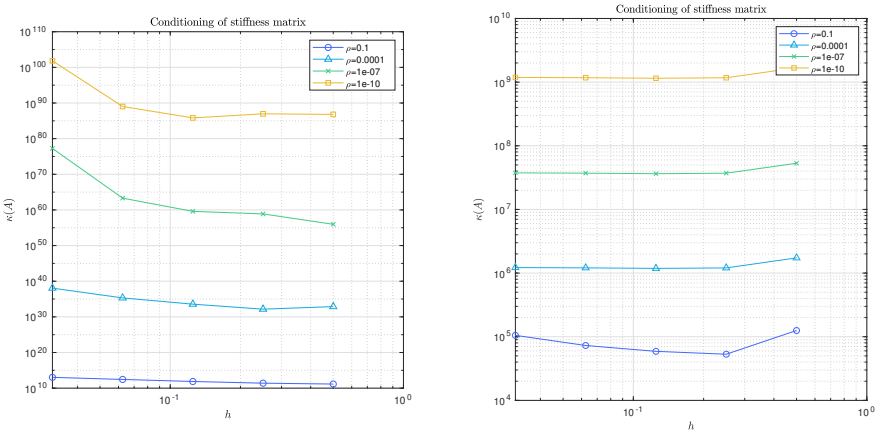

(a) 1-conditioning number without preconditioning

(b) 1-conditioning number with preconditioning

Figure 8.1: Taylor-Hood with weak Dirichlet B.C.: comparison of 1-conditioning number without (left) and with (right) application of diagonal preconditioning for decreasing mesh-sizes h and trimming-to-element ratio ρ.

previous section on the conditioning number. We consider the 1-conditioning number $\kappa(A) := \|A\|_1 \left\|A^{-1}\right\|_1$ where $\|A\|_1 := \max_{\boldsymbol{x}\in\mathbb{R}^N} \frac{\|Ax\|}{\|x\|}$. The 1-conditioning number is estimated by the Matlab function `condest`. Results for the Taylor-Hood elements can be seen in figure 8.1, while those for Raviart-Thomas elements can be seen in figure 8.2. In both cases, without preconditioning the conditioning number is strongly influenced by the trimming-to-element ratio and reaches, for the smallest values of ρ values far beyond acceptable. The application of the preconditioner leads in both cases to a reduction of the conditioning number for the same values of ρ. However, there is still a dependence of the value on ρ.

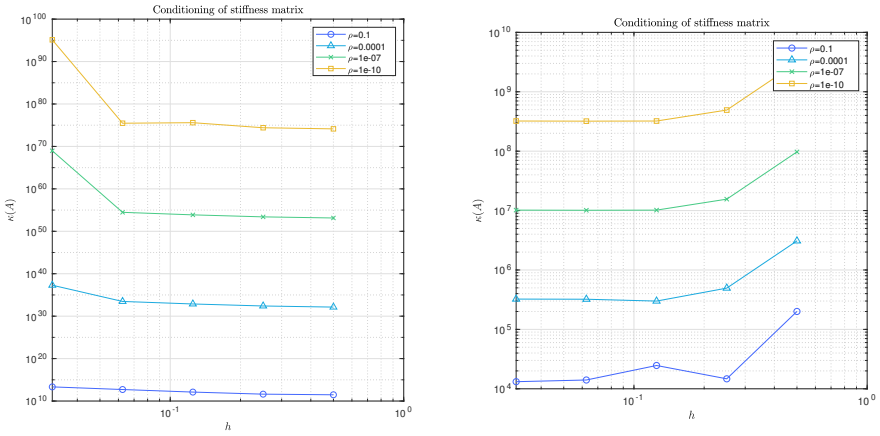

(a) 1-conditioning number without preconditioning

(b) 1-conditioning number with preconditioning

Figure 8.2: Raviart-Thomas with weak Dirichlet B.C.: comparison of 1-conditioning number without (left) and with (right) application of diagonal preconditioning for decreasing mesh-szes h and trimming-to-element ratio ρ.

Chapter 9

Conclusions and outlook

This final chapter starts with a summary of the results from the numerical experiments carried out in the previous chapters. The subsequent section describes which of the goals set in the introduction have been achieved. The final section describes possible future developments of the present work.

9.1 Summary of results from numerical experiments

In this section the results from the numerical experiments carried out in chapters 5, 6, 7 and 8 are summarized and their main features highlighted. Several trimming curves are considered in order to analyse the effect of the position of the trimming curve with respect to knot-lines of the mesh on the stability and convergence of the schemes. In chapter 5 and 6 the case of sliver-cuts, for which the trimming curve runs parallel and relatively close to a knot-line, is analysed. We observe that imposing Neumann boundary conditions on the trimmed portions of the boundary does not lead to stability issues and the convergence rates are optimal. By contrast, imposing Dirichlet boundary conditions weakly on the trimmed boundary causes the problem's stability (in particular continuity and coercivity) to depend on the position of the trimming curve with respect to the closes knot-line. As a possible solution, the stabilization reported in Chapter 4 is adapted to the problem at hand and successfully applied to make the stability properties of the problem independent of the position of the trimming curve. In the case of sliver-cuts, we observe that the inf-sup stability of the problem is not damaged. Different trimming curves are considered in Chapter 7, in particular a diagonal line that is not parallel to any knot-line and a quarter of circumference. In the case of the diagonal trimming line, the stability problems observed in the previous case do not reappear (indeed, no sliver cut-elements is present), however it appears that both Taylor-Hood and Raviart-Thomas spaces are not inf-sup stable. This effect may be related to the possible degenerate shapes that the active parts of cut-elements can take in this setting, in particular small triangles and pentagons with two short sides. Finally, in the case of the quarter of circumference, both stability issues observed above appear (cut-elements can take both the degenerate shapes observed in the two previous cases). The loss of coercivity and continuity can again be cured applying the stabilization. In all cases the diagonal preconditioner described in Chapter 8 allows to sensibly reduce the conditioning number of the problems, but not to make it independent of the position of the trimming curve. Finally, we remark that for trimming curves that lead to small active regions of cut-elements, round-off errors can limit the accuracy of the solution.

9.2 Achieved goals

In the present work the isogeometric discretization of the Stokes problem on trimmed domains is analysed. Problem formulations are derived for Taylor-Hood and Raviart-Thomas isogeometric elements. We remark that, at the cost of employing a non-symmetric formulation, the divergence-conforming property of Raviart-Thomas elements allows to produce divergence-free numerical solutions. The imposition of essential boundary conditions is carried out in a weak fashion thorough Nitsche's method. The stability and convergence of the numerical scheme is analysed through several numerical experiments characterized by different trimming curves. As the numerical experiments confirm the presence of stability problems for some configurations of trimming curves and meshes, a stabilization strategy first introduced for the Poisson problem is adapted and successfully applied to cure the stability issues. Numerical experiments also confirm or suggest the presence of other possible problems. For instance, problems related to conditioning and round-off errors and the possible loss of inf-sup stability for some configurations of trimming curve and mesh.

9.3 Outlook

Finally, we outline some possible further developments of the present work. Firstly, we remark that some of the results presented in Chapter 7, in particular the ones obtained with Raviart-Thomas elements, cannot be completely explained (e.g. suboptimal convergence of the errors on the pressure). Therefore, the implementation requires a more in-depth analysis. Secondly, the body of numerical experiments could be enlarged, for instance considering different trimming curves and boundary conditions (observe that the case of a Neumann boundary conditions on the trimmed boundary is not presented in chapter 7). Moreover, the case in which both a complex trimming curve and a non-trivial parametric-to-physical mapping are present still has to be studied. Finally, all experiments should be repeated with different spline degrees and regularities. As for conditioning, a preconditioner that makes the conditioning of the problem independent of the position of the trimming curve is desired. As for inf-sup stability, if the results from chapter 7 are confirmed, a more detailed study of the effect of trimming on inf-sup stability may be needed. The problematic trimming configurations should be identified and a stabilization strategy derived. Finally, the numerical experiments presented in this work may suggest possible directions for theoretical developments, such as proofs of the well posedness of the stabilized schemes.

Bibliography

[1] P. Antolin, A. Bressan, A. Buffa, and G. Sangalli. An isogeometric method for linear nearly-incompressible elasticity with local stress projection. *Computer Methods in Applied Mechanics and Engineering*, 316:694–719, 2017.

[2] I. Babuška and A. Aziz. Survey lectures on the mathematical foundations of the finite element method, univ. *Maryland, College Park, Washington DC, Techinical Note BN-748*, 1972.

[3] D. Boffi, F. Brezzi, M. Fortin, et al. *Mixed finite element methods and applications*, volume 44. Springer, 2013.

[4] A. Bressan. Isogeometric regular discretization for the stokes problem. *IMA journal of numerical analysis*, 31(4):1334–1356, 2010.

[5] A. Buffa, C. De Falco, and G. Sangalli. Isogeometric analysis: stable elements for the 2d stokes equation. *International Journal for Numerical Methods in Fluids*, 65(11-12):1407–1422, 2011.

[6] A. Buffa, R. Puppi, and R. Vázquez. Article in preparation.

[7] A. Buffa, J. Rivas, G. Sangalli, and R. Vázquez. Isogeometric discrete differential forms in three dimensions. *SIAM Journal on Numerical Analysis*, 49(2):818–844, 2011.

[8] A. Buffa and G. Sangalli. *IsoGeometric Analysis: A New Paradigm in the Numerical Approximation of PDEs: Cetraro, Italy 2012*, volume 2161. Springer, 2016.

[9] E. Burman, S. Claus, P. Hansbo, M. G. Larson, and A. Massing. Cutfem: discretizing geometry and partial differential equations. *International Journal for Numerical Methods in Engineering*, 104(7):472–501, 2015.

[10] E. Burman and P. Hansbo. Fictitious domain methods using cut elements: Iii. a stabilized nitsche method for stokes' problem. *ESAIM: Mathematical Modelling and Numerical Analysis*, 48(3):859–874, 2014.

[11] F. de Prenter, C. Lehrenfeld, and A. Massing. A note on the penalty parameter in nitsche's method for unfitted boundary value problems. *arXiv preprint arXiv:1709.05832*, 2017.

[12] F. de Prenter, C. V. Verhoosel, G. van Zwieten, and E. H. van Brummelen. Condition number analysis and preconditioning of the finite cell method. *Computer Methods in Applied Mechanics and Engineering*, 316:297–327, 2017.

[13] J. A. Evans. *Divergence-free B-spline discretizations for viscous incompressible flows*. PhD thesis, 2011.

[14] S. Fernández-Méndez and A. Huerta. Imposing essential boundary conditions in mesh-free methods. *Computer methods in applied mechanics and engineering*, 193(12-14):1257–1275, 2004.

[15] T. J. Hughes, J. A. Cottrell, and Y. Bazilevs. Isogeometric analysis: Cad, finite elements, nurbs, exact geometry and mesh refinement. *Computer methods in applied mechanics and engineering*, 194(39-41):4135–4195, 2005.

[16] B. Marussig and T. J. Hughes. A review of trimming in isogeometric analysis: challenges, data exchange and simulation aspects. *Archives of computational methods in engineering*, 25(4):1059–1127, 2018.

[17] L. Piegl and W. Tiller. *The NURBS book*. Springer Science & Business Media, 2012.

[18] R. Stenberg. On some techniques for approximating boundary conditions in the finite element method. *Journal of Computational and applied Mathematics*, 63(1-3):139–148, 1995.

[19] R. Vázquez. A new design for the implementation of isogeometric analysis in octave and matlab: Geopdes 3.0. *Computers & Mathematics with Applications*, 72(3):523–554, 2016.

[20] J. Xu and L. Zikatanov. Some observations on babuska and brezzi theories. *Numerische Mathematik*, 94(1):195–202, 2003.